TABLE OF CONTENTS

LIST OF FIGURES

LIST OF TABLES

TABLE PAGE

CHAPTER 1 - INTRODUCTION

1.1 Motivation and Statement of the Problem

Today, computers are part of many aspects of human activity. There is great interest in research that seek to enhance human-computer interactions, developing new ways in which users can provide input to computer systems and mechanisms by which the users can perceive the output from computers. In particular, there is a current interest in developing systems that could allow users to provide input to the computer in ways that are more natural and intuitive. Several studies have attempted to develop alternate methods to achieve input and output to and from computer systems, beyond the general input devices (e.g., keyboard, mouse, and screen). Voice command systems have been developed by numerous research groups since 1952 [1] and are becoming one of the most commonly used input methods, in both computer and mobile systems, providing a natural way to give input commands and dictation to computer systems. Similarly, 3D graphics have become widely adopted by some computer industries [2], such as gaming and designing [3] [4], pursuing the representation of computer objects in highly realistic ways. As the realism of computer representations has been enhanced, the popularity of Virtual Reality (VR) and Augmented Reality (AR) has increased in many applications [5]. In this current context, it would be highly beneficial for computer systems to have the real-time ability of capturing hand movement in terms of both position and orientation. This kind of capability would enable the development of natural human-computer interaction systems that could operate intuitively in 3D space [6].

One of the key objectives of using VR and AR is to create a simulated environment and make the user feel immersed in that 3D world, giving him/her the

ability to interact with that world in a natural and effortless fashion. VR and AR developers endeavor to provide simulated simulation to several senses, such as vision, hearing, touch, or even smell, to foster the sensation of presence in the user. In these types of environments, hand motion tracking is an interesting choice for users to interact more naturally with 3D interfaces than regular input devices like mice, game pads, joysticks and wands, which require the user to perform highly artificial sequences of actions. These unnatural actions may play an important role in reducing the sensations of immersion and presence experienced by the users. In contrast, hand motion tracking can be used to implement a more intuitive mechanism to provide input to the computer and provide the computer with a mechanism to gauge the user's body language as the user grabs and holds objects, moving objects from place to place in the surrounding environment. Thus, an improvement in the computer's capability to perform real-time hand tracking may be a crucial step towards the development of the next generation of human-computer interaction systems.

1.2 Hand Gestures

Several studies present different methods to capture hand gestures, such as Video-based systems, and systems based on resistor strips, or Inertial Measurement Units (IMUs). Video-based systems are computer vision systems that utilize image processing algorithms to perceive the motion of the hand and its configuration. Many studies propose methods using image processing to perceive and record gestures of the hand [7]. These systems may provide hand tracking capabilities on the bases of images from one or several cameras. However, the principle of operation for these systems requires the hand to be always visible by the cameras. In addition, these systems also

need high resolution cameras and can tolerate only a minimal amount of interference (noise). Furthermore, the system needs enough lighting to capture the hand clearly. [8] Force Sensing Resistors, usually available as resistor strips, physically measure the movement of the fingers and the configuration of the hand posture by detecting the resistance changes due to stretching of the strip as the fingers bend [9] [10]. The resistor strips do not measure the orientation or the position of the hand. They can detect some actions of the fingers, such as grabbing, flexing, and pointing. Many studies that attempted to record complex hand gestures have resorted to combining resistor strips with IMUs to simultaneously acquire hand orientation. [11].

The use of miniaturized MEMS Inertial Measurement Units (IMUs) is one of the emerging approaches for hand motion tracking. The gyroscopes in IMUs provide the angular velocity of the moving hand parts and, by accumulation, can yield their orientation angle. Different types of IMUs are used in many industries and have a wide range of accuracy levels that tend to be in proportion to their price, from Navigation Systems in aviation to the smaller size IMUs used in portable devices (e.g., mobile phones). Therefore, it could be expected that IMUs might be utilized to determine the orientation of the human hand for interaction in virtual 3D spaces.

1.3 Hand Tracking using IMUs – Limitations and Concerns

Micro-Electro-Mechanical Systems (MEMS) accelerometers were first introduced in the 1990s and MEMS gyroscopes in 2009 [12]. The combination of MEMS accelerometers and gyroscopes are called Inertial Measurement Units (IMUs). MEMS magnetometers are included in some models. In that case, the sensor module is called a Magnetic, Angular-rate, Gravity (MARG) module. The angular velocity given from the gyroscopes in IMUs can, in principle, be accumulated through numerical

integration to obtain the orientation (angle) of an object in space. By mounting the MEMS IMU sensor on a moving object (which defines the "Body Coordinate Fame"), it can measure the object's acceleration and angular change. This method can be used to determine the current position of the object with respect to a fixed frame of reference ("Inertial Coordinate Fame") by using double numerical integration of the acceleration to determine position. Figure 1.1 shows the tracking process from the inertial motion using a tri-axial gyroscope and a tri-axial accelerometer.

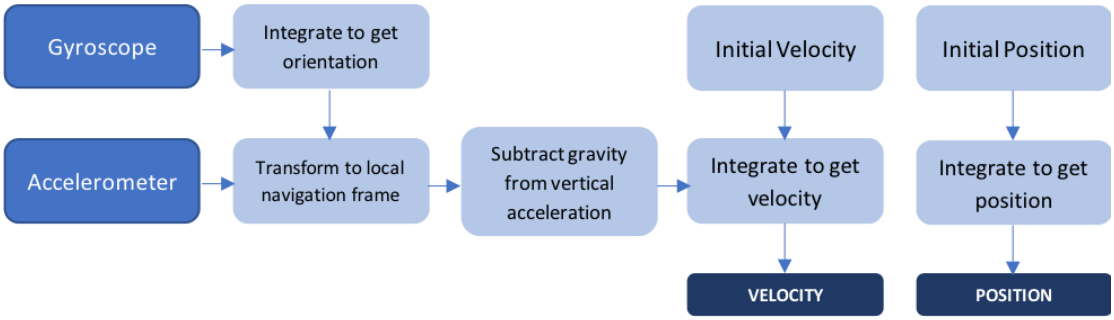

Figure 1.1Inertial Motion tracking process

Manufacturers provided many types of IMUs for different purposes. Each type is unique in terms of its level of accuracy, which varies with the price range of the different types. The different grades of IMU have significantly different error and noise characteristics, as shown in Table 1.1, listing the accuracy of IMUs utilized for strap-down inertial position tracking (from Foxlin's study [13].)

Table 1.1Functional parameters of different types of IMU components from Foxlin

	Commercial-Grade	Tactical-grade	Navigation-grade	Strategic-grade	Geophysical limit
Gyro bias stability	1500°/hr/√hr	15°/hr/√hr	0.015°/hr/√hr	0.000015°/hr/√hr	0°/ hr/√hr
Gyro bias initial uncertainty	150°/hr	1.5°/hr	0.0015°/hr	0.0000015°/hr	0°/hr
Accel bias stability	1 mg/√hr	100 µg/√hr	10 µg/√hr	0.5 µg/√hr	0 µg/√hr
Accel bias initial uncertainty	0.25 mg	10 µg	1 µg	0.1 µg	0.1 µg
Initial orientation alignment	1 arcsecond	1 arcsecond	1 arcsecond	0.1 µrad	0.01 µrad

Table 1.1lists the uncertainty and stability of the readings obtained from different types of gyroscopes. This type of error is called "the bias offset error," and is generated in the gyroscopes by providing a non-zero output when the sensors are static,

and no actual physical rotation is taking place. The bias offset error can result in high levels of orientation tracking error, as the angular velocity readings have to be integrated over time. This type of orientation error, called “drift,” is a common effect that continues to grow through time as the sensor operates and keeps integrating the rotational speed measurements to yield current orientation values (an approach also known as “Dead Reckoning”).

This dissertation proposes to use MEMS modules that contain three accelerometers, three rate gyroscopes, and three magnetometers, in combination with IR cameras to obtain a real-time estimate of the orientation and position of the hand of a human subject. In order to overcome the problems of orientation measurement through the use of gyroscopes that were described in previous paragraphs, an algorithm is introduced to fix the drift error utilizing the signals from all the sensors available in the MEMS modules.

1.4 Problem Statements and Hypotheses

Question 1: Can the gyroscope drift problem in the MARG module be corrected using the high-level, adaptable MARG module orientation corrections?

Hypothesis 1: The gyroscope drift problem in the MARG module will be corrected using the proposed algorithm, which determines and compensates the bias offset error and performs orientation correction on the basis of the gravity vector measured by the accelerometer and the magnetic North vector measured by the magnetometer.

Question 2: Can we map the magnetic distortions within the working area and use that mapping to adapt the relevance of magnetometer-based correction in the calculation of the overall orientation estimates produced?

Hypothesis 2: The system will create a voxel map and indicate the value of magnetic distortion in the specific cubic voxels visited by the sensor, determined by comparison of orientation estimates derived from magnetometer readings and from accelerometer readings, for intervals when the sensor is determined to be static. The number of voxels with an assessment of magnetic distortion level will grow as the systems continue in operation through time.

Question 3: Can we build the system to track the hand motion using several sensor modalities (gyroscope, accelerometer, and magnetometer)?

Hypothesis 3: The proposed hand motion tracking system will make it possible to efficiently track the human hand movement at each movable segment of the hand, attaching one MARG module to it. The system will make it possible to accurately track the hand motion by combining two different sources of data acquisition.

1.5 Literature Review on Gyroscope drift correction and IMUs limitations

Many systems use IMUs to track orientation in diverse applications, where the drift experienced in the dead reckoning approach is a common error known by the researchers. There are several studies and developments on denoising and error correction of IMUs to address this problem. Each method employs a different type of model and calculation. This section presents some examples of denoising methods for various types of applications that attempt to track parts of the body with IMUs. In addition, some specific technologies for Real-time Hand tracking are listed in this section.

1.5.1 General Motion Tracking

Kalman Filtering is a popular method used in many applications for gyroscope drift error correction. Zhang [14] integrates a low-cost IMU with an odometer for the

purpose of mapping an underground 3-D pipeline. Applying Extended Kalman Filtering, the outlier measurements from the odometer, due to the wheel-slip, were removed. His system, which included robust Kalman Filter, showed comparable results with an expensive Duct Runner pipeline mapping system in the market. DW. Qiu applied Kalman Filter to improve the running time and reduce IMU drift for his Binocular vision mobile measurement system. With the combination of cameras and an IMU system, his work could improve the measurement accuracy of stereoscopic vision by 84.0% [15]. In Attitude and Heading Reference and System (AHRS) estimation, Yang has introduced a fusion algorithm of Fast Euler Singular Value Decomposition Cubature Kalman Filter. His algorithm improves the filter accuracy, compared with the Cubature Kalman Filter alone, in both low and high dynamic flight conditions [16]. All three studies above have shown the improvement of their system to achieve an individual task but using Kalman Filter led to increases in complexity that they had to face. For example, it was essential to properly estimate the covariance matrices involved in the model.

To avoid the difficulty of Kalman Filter, Khankalantary applied an adaptive constrained type-2 fuzzy Hammerstein neural network (T2FHNN) on his Strap-down inertial navigation system / Global navigation satellite system (SINS/GNSS) approach [17]. During the GNSS outage, MEMs measured the vehicle acceleration and rotation rate using gyroscopes and accelerometers, which represent a SINS Dynamic. This proposed algorithm consists of four layers, identified as: input, nonlinear static gain, linear dynamic, and output layer. The stability of the algorithm depended on the learning rate of the HNN. A low learning rate can delay the system; on the other hand, a high learning rate can lead to the un-stability of the HNN, which related to the vehicle maneuvers. A type-2 Fuzzy system was applied to set the learning rate for HNN

weights. To overcome the drift error from the IMUs, GNSS was picked to compensate for the error. However, since GNSS is based on satellite data, the signal may be obstructed. Brossard [18] developed a Deep Learning method for denoising IMU gyroscopes for Open-Loop Attitude Estimation. The neural network computed the gyro correction from the leveraging information present in the past local window, where the learning problem of using time-varying data for calibration parameters remained. His proposed algorithm obtained remarkable accurate attitude estimates, which offered a new perspective for inertial learning methods. However, the performance of the algorithm is based on a prudent design and feature selection of a dilated convolutional network, and an appropriate loss function leveraged for training on orientation increment at the ground truth frequency.

1.5.2 IMUs tracking body motion.

Ergonomists have proposed different ways to measure body movement, and they consider a direct measurement method as the most efficient tool. Using IMUs is one of the approaches followed to correct kinematics. Qilong Yuan [19] studied dynamic motion from 4 activities: walk, run, jump, and swing. He mounted IMUs on the lower limb, the right thigh, the right shank, and the right foot of the subject to capture the lower limb's motion. He presented an uncertainty-based fusion approach with a model based on magnetic and acceleration measurements for an Extended Kalman Filter orientation estimator. This method achieved some success in tracking the different types of motion with and without acceleration shocks, but it still showed need for improvement to study long-term and extremely dynamic situations. Ming Hao [20] proposed a Smoother-Based method for 3-D foot trajectory estimation using IMUs attached to the heel of each shoe. The Zero Velocity Update (ZUPT) method was applied, followed by smoothing, and then an Extended Kalman Filter was used to

reduce drift-related error. The result showed a good performance among similar methods and can improve the accuracy of foot trajectory both on stride length and stride width. However, this method is still limited under some indoor assumptions and did not correct the drift error of yaw due to the sensitivity of magnetometers with indoor environments. ChandraTjhai [21] has also studied the walking motion. In this approach, IMUs were mounted at the shank and foot for each side. Rauch Tung Striebel (RTS) filter is used to yield motion and eliminate drift, while IMUs needed pre-calibration to remove bias before use. RTS also has a reverse loop, which improves the robustness. This proposed system presented similar movement result as the high-precision robot arm that was used as a reference. Nevertheless, the RTS filter required a proper initialization, and the sensor frames have to be aligned with the vertical gravity axis and the patient's direction of motion for the setup. Kiyoshi Irie [22] studied the swing motion in sports (for example, in table tennis) measured using an IMU and a monocular camera. The clocks from both sensors must be precisely synchronized at the beginning of the recordings. To overcome the IMU error, the Least-Squares method with Gauss-Newton, Hessian matrix, and Newton methods are applied to Loop-closure for Attitude, velocity, and position, respectively. The proposed method significantly improved the accuracy of the inertial motion estimation, compared to similar approaches, which will be useful for sports skill evaluations. However, the process of synchronizing the clock has to be careful since it is the key to the system, and it is highly sensitive.

Operation of modern prosthetics requires Real-Time feedback from the artificial body parts to enhance their performance. S. Shaikh [23] developed a Stump Angle Measurement (SAM) system using the accelerometers in IMUs to measure the “tilt” angle of the residual stump during various phases of the gait of a low-cost electronic

knee prosthesis. The sensor was placed and measured the thigh angle. He applied a Kalman Filter to improve the accuracy of IMU estimations. In addition, the SAM system tried to remove high-frequency noise from the gait events. The results from IMU provided a reliable feedback signal and successfully detected the gait events with 93% accuracy rate but only under limit movement conditions. Application to wider mobility conditions will be studied in the future. Clement Duraffourg [24] also studied the Real-Time estimation of the Pose of a Lower Limb prosthesis, placing the IMU at a shank. The data was captured during a swing of the gait cycle. The system used a nonlinear complementary filter with a variable gain to estimate attitude. The algorithm did not use the magnetometer in the IMU and assumed a drift-free operation in the experiment. This system allowed a better real-time estimation of the trajectory, potentially allowing faster gait mode detection.

1.5.3 Real-time Hand tracking by any method

To capture human hand gesture and motion, several studies have introduced systems using different types and numbers of sensing units. This section presents some examples of hand motion tracking systems and technologies.

Haihan Duan [25] tracked hand gestures using an ambient light-based system. The system relied on ubiquitous ambient light and low-cost photodiodes. A recurrent neural network (RNN) was used to process the signal data, which give an accurate recognition [26] rate of 99.31%. The system only captures the shape of the hand but not its orientation. Dinh-Son Tran also worked with a Neural Network (3D convolutional) for spotting hand gestures in real-time using a Camera-based system from the Kinect RGB-D camera. Kinect provides a skeletal tracker, which may be useful for tracking finger and hand shape. The system first extracts the hand region from the depth image, and then points the position of a fingertip using the K-cosine

corner detection algorithm. The data is then processed with a 3D convolutional neural network to recognize the gesture. The experiment was done with 50 participants, which generated 5250 samples. The researchers randomly select 70% of data as training data, 10% for validation, and 20% as testing data. The results with 3DCNN models gave an accuracy rate of more than 90% but required training times more than an hour and could be negatively impacted by changes in ambient lighting. Gabyong Park [27] combines a depth camera and a gyroscope to enhance the 3D hand tracking feature for fast movement. A matrix was constructed in order to alleviate the drift problem from the gyroscope. The time delay and pose offset between a depth camera and a hand-worn gyroscope have to calibrated before the beginning of the system operation. With this sensor-fusion method, the system successfully captures hand motion during fast movements even if the image is distorted due to excessive motion blur. Shuo Jiang [28] attached a stretchable e-skin patch on the back of the hand to recognize hand gestures by estimating skin strain. Each finger flexion changes the strain of the muscle at the back of the hand. Therefore, his study used this approach to classify the hand gestures for simple American sign language signs (e.g., numbers 0-9). The results showed classification accuracies of more than 90%. However, there are two key challenges in this research that must be overcome, the skin strain complexities and the sensitivity of the sensor.

1.5.4 Alternative algorithms for gyroscope drift corrections

Over the last several decades, there have been numerous approaches proposed for orientation estimation fusing measurements from gyroscope and accelerometer readings (i.e., from IMU modules) first, and later including the additional fusion of magnetometer readings. Nazarahari and Rouhani [29] offer a fairly comprehensive and systematic cataloguing of those efforts, identifying 3 major families of approaches:

Vector Observation (VO), Complimentary Filter (CF) and Kalman Filters (KF) .Further, these same authors did an experiment to compare 36 Sensor Fusion Algorithms from their survey which could be categorized into 7 major groups: Linear Complementary Filter (LCF), Nonlinear Complementary Filter (NLCF), Linear Kalman Filter (LKF), Extended Kalman Filter (EKF), Complementary Kalman Filter (CKF), Square-root Unscented Kalman Filter (SRUKF), and Square-root Cubature Kalman Filter (SRCKF) [30]. They concluded that the method proposed by Sabatini [31] showed lower errors when time is not a factor, while the methods from Hua et. al [32] or Justa et. al [33] were found to give the best results when the execution time is a factor.

Harindranath [34] created a simulation platform in MATLAB that compared another four popular orientation algorithms in a 9-axis MARG unit which are Madgwick Algorithm [35], Mahony Algorithm [36], Extended Kalman Filter and Two Stage KF-Q update. It was found that the Mahony filter performed best in the low level of noise while the Two Stage KF-Q worked well in a higher noise level.

The Kalman Filtering, envisioned by Dr.Rudolf E.Kalman [37], is one of the most popular methods to estimate the state of a dynamic system for which there is a model and instantaneous observations [38]. In its simples form the Kalman Filter obtains an enhanced ("posterior") fusing the results predicted from a model (use as "prior" estimate) with instantaneous measurements through Bayesian Estimation. It is noteworthy that in the Kalman Filter the predicted estimate resulting from the model is "corrected" in the second stage of the process by involvement of the instantaneous measurements. The final state estimate that results has fused the result from the model and the information derived from the instantaneous measurements according to the level of "trustworthiness" of both sources (represented by their covariance

matrices).Although the original Kalman Filter was developed of the basis of a linear state transformation and the assumption of Gaussian distributions for all the quantities involved, subsequent versions (e.g., “Extended” and “Unscented”) of the Kalman Filter concept have been adapted for application to non-linear models.

JL Marins [39] studied an extended Kalman Filter for Quaternion-Based Orientation Estimation Using MARG Sensors of a rigid body motion in real-time. According to the highly nonlinear functions of the process state variables from 3 sensors (gyroscope, accelerometer, and magnetometer), the partial derivatives needed for Kalman Filtering were very complicated and not applicable for real-time applications. To be able to use Kalman Filter in real-time, Marins needed to apply the Gauss-Newton iteration algorithm in his method. The complexity of using Kalman Filtering correction in real-time process is also shown in Peppoloni’s study [40] as it highlights the difficulty in correctly setting up and updating the critical Kalman Filter parameters.

Some commercial MARG modules used to offer an internally implemented (Extended) Kalman Filter. For example, the 3-Space sensor Micro USB model from Yostlab [41] provides the Kalman Filter as a default filter mode. In it, statistical techniques were used to combine normalized sensor data and reference vector data into a final orientation which be directly read from the module (This has been done in this research to have a basis for comparison). However, Yostlab has more recently developed an alternative proprietary filter algorithm called “QGRAD2” [42]. They claim that this new sensor fusion algorithm is more efficient and has 3 times faster update rate than their original Kalman Filter. Another potential drawback on many Kalman-based approaches is that the levels of “trustworthiness” of the several sources of information (gyroscope-based model and accelerometer- and magnetometer-based

measurements) are represented by constant covariance matrices, which is not an exact match with the reality that governs the appropriateness of the accelerometer- or magnetometer-based correction estimates. As Mahoney et al. pointed out [36] "Traditional linear Kalman Filter techniques including EKF techniques have proved extremely difficult to apply robustly to applications with low quality sensors systems."

More recently, some groups have attempted to consider dynamic assessments of the varying levels of "trustworthiness" that must be assigned in making accelerometer- and magnetometer-based orientation corrections. Madgwick Algorithm [35], indicates that his algorithm "contains 1 (IMU) or 2 (MARG) adjustable parameters defined by observable system characteristics." For the case of an IMU (i.e., no magnetometer) he indicates "The filter gain, β, represents all mean zero gyroscope measurement errors, expressed as the magnitude of a quaternion derivative" However, Madgwick adjusted these parameters just once for each of his implementations ("The proposed filter's gain β was set to 0.033 for the IMU implementation and 0.041 for the MARG implementation.") These parameters are not, therefore truly dynamic in terms of being re-assigned as frequently as every iteration according to the instantaneous circumstances in which the system is performing.

There have also been studies that have attempted to assess and account for the reduced level of "trustworthiness" associated to the magnetometer-based corrections. Roetenberg et al. [43] showed that the Kalman Filter's performance would deteriorate when there is a disturbance of the magnetic field. They attempt the identification of a possible magnetic disturbance on the basis of the magnitude of the total magnetic flux recorded by the magnetometer and the detection of change in the magnetic declination ("magnetic dip angle") derived from the magnetometer measurements and the current orientation estimate of the MARG module. Then in 2015, Daponte et al. [44] proposed

a new way to estimate the orientation of MARG units with the capability of compensating short-duration magnetic disturbances using the Gradient Descent Algorithm. He continued his research for long-duration disturbances from the magnetometer embedded on a smartphone in 2017 [45] by modeling the disturbances from both hard iron and soft iron. Jin Wu [46] proposed a novel nonlinear optimization approach to address magnetometer disturbances in real-time, using the interior-point method. He proposed that his unique solution could correct the issue efficiently and with a fast response, but this proposed method only deals with soft-iron disturbances that are not very strong.

In recent years, Valenti et al. [47] and our own group have independently proposed an alternative way to execute the "correction" phase of the sensor fusion algorithm for MARG orientation estimation. Based on the work of Shoemake [48], Valenti proposed the use of linear quaternion interpolation (LERP), for small corrections and spherical linear quaternion interpolation (SLERP) only for larger corrections, calculating the correction quaternion (i.e., Δq_{acc}) and executing the correction in the global (inertial) frame of reference. Based on the report from Dam et al. [49] our group proposed the use of SLERP for all corrections, calculating the quaternion correction (i.e., Δq_A) and executing it in the MARG's body frame, in our initial algorithm, GMV-S [50]. Valenti et al. control the amount of interpolation through a parameter $0 < \alpha < 1$, which characterizes the cutoff frequency of their complementary filter, as described by Franceschi and Zardi [51]. Our interpolation control variable is derived from the "confidence" parameter representing how close the MARG is to being static [41]. In their report, Valenti et al., found that their method achieved better results in all three angles (roll, pitch, and yaw) in comparison to the

Madgwick filter and the Extended Kalman Filter for situations with and without magnetic disturbances.

In 2019, Meyer developed an approach similar to Valenti's but with a more cautious incorporation of the accelerometer measurement [52]. He added layers for checking the accelerometer magnitude error, rate of change of the magnetic field vector and a model of the gyro bias before he fed the data into the estimation correction system. He performed a simulation test with modeled Gaussian noise added to the three sensors. In results from 50 test runs, his model was successful in distinguishing slow dynamic maneuvers from biases and could eliminate the problem of pseudo steady-states. However, he indicated that it was too soon to be sure that the filter would be suitable for extended periods of dynamic motion and the filter's robustness to magnetic distortion would need to be investigated more extensively.

CHAPTER 2 - TRANSFORMATIONS IN THREE-DIMENSIONAL SPACE

This chapter will briefly explain the equations and models available for the transformations in three-dimensional space that apply to this research. The linear three-dimensional transformations consist of four types: Translation, Rotation, Scaling Shearing, and Reflection. This research focuses only on rotation. Two main systems that are used in this research to model rotations are Euler angles and Quaternions.

2.1 Three-Dimensional Coordinate Systems

The locations of points or geometric elements can be represented in coordinate systems, which may be orthogonal or non-orthogonal. Non-orthogonal coordinate systems are rarely used for the study of the topics relevant to this dissertation, while the orthogonal are most commonly used. With the information from the coordinate system, measuring distance, area, volume, and direction can be obtained using an algebraic system. Examples of orthogonal coordinate systems are the Cartesian or Rectangular, the Circular Cylindrical, the Spherical, the Elliptic Cylindrical, the Parabolic Cylindrical, the Conical, the Prolate Spheroidal, the Oblate Spheroidal, and the Ellipsoidal. This research will primarily use the Rectangular or Cartesian system. The Cartesian coordinate system in three-dimensional space consists of three axes (x, y, z), perpendicular to each other. In a two-dimensional space, the x-axis is the horizontal axis, where the numbers increase from left to right. The y-axis is the vertical axis, where the numbers increase in an upward direction. These two axes form a plane where the y-axis is 90 degrees counterclockwise apart from the x-axis. In three-dimensional space, the z-axis is added to the x-y plane. The direction assigned to the z-axis depends on the use of “left-hand rule” or the “right-hand rule”. The left-hand rule and the right-hand

rule are shown in Figure 2.1, where the thumb, index finger, and middle finger indicate the x-axis, y-axis, and z-axis, respectively. The curved arrows represent the direction of positive rotation about each axis according to the rule.

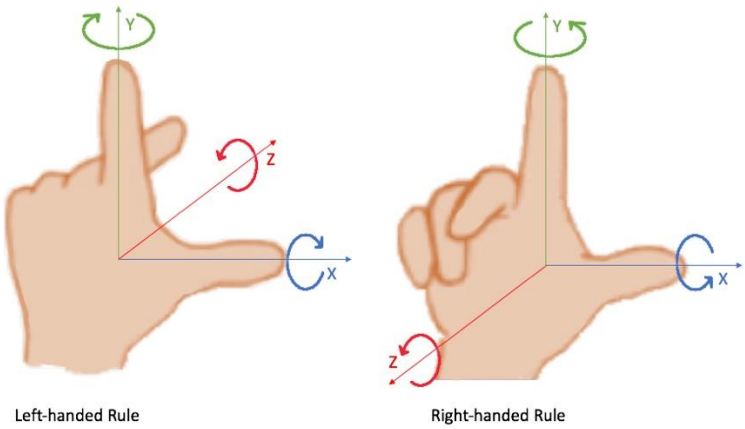

Figure 2.1The Cartesian Coordinate in Three-Dimensional Space

The German geodesist F.R. Helmert [53] introduced a transformation method within three-dimensional space that changes coordinates from one reference frame to another. Defining the frames of reference and their axes is necessary to unambiguously specify the location, direction, and orientation of objects in a navigation system. In this research, there are three reference frames used to describe the three-dimensional rotation: the inertial frame, body frame, and earth-centered-earth-fixed frame. All the frames are orthogonal and right-handed Cartesian frames.

2.2.1 The Inertial Frame

A fundamental coordinate system, used in the study of Newton's laws of motion, is the inertial frame. This frame of reference is commonly used when a body is at rest (or moving at a constant speed in a linear motion) [54]. The origin of this frame is located at the center of the Earth. The frame is not rotating under the gravitational influence of the stars.

2.2.2 The Body Frame

The body frame is the frame commonly used to represent an object under study. The origin of this frame is located at the center of gravity of the rotating object. The axes are determined along the forward direction as x-axis (roll), in the right direction as y-axis (pitch), and through-the-floor direction as z-axis (yaw). Figure 2.2 depicts the body frame of an aircraft, indicating the corresponding directions of rotation.

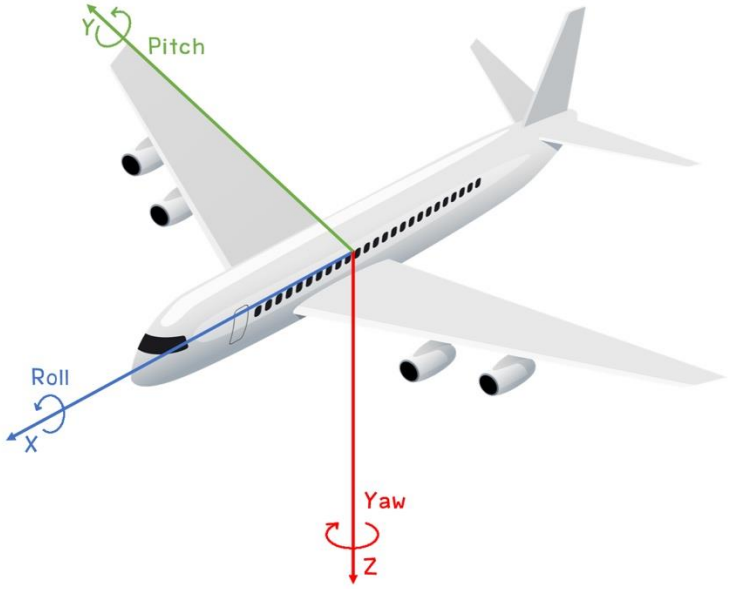

Figure 2.2Body frame of an aircraft

2.2.3 The Earth-Centered-Earth-Fixed Frame

The third frame of reference considered is fixed to the Earth, with its origin located at the center of the Earth's mass. The Earth frame is constantly rotating with the polar motion of the Earth about the international reference pole (IRP), which is defined as the z-axis. The point where the prime meridian in Greenwich (0° longitude) and the Earth's equator (0° latitude) intersects, create the fixed x-axis of the Earth's frame. The x-axis and z-axis generate a plane, and the y-axis is a line perpendicular to this xz-plane. The graphic in Figure 2.3 shows the location of the axes of the Earth's frame.

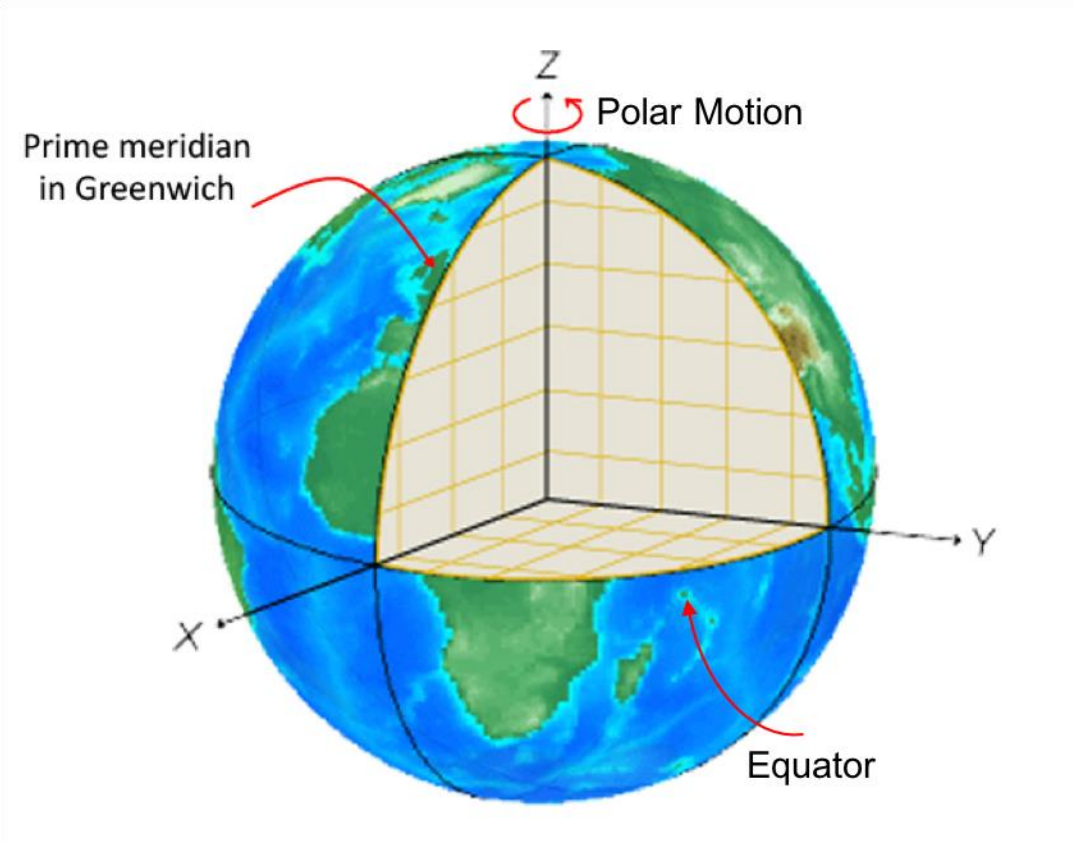

Figure 2.3Earth-Centered-Earth-Fixed Reference Frame. Adapted from Mathworks [55].

2.3 Transformations

A transformation is a process for re-position and orientation of a rigid body from one frame to another with respect to known coordinates. It can be simply defined by a vector of coordinate differences which is equally applied to all the points in a frame. If the frame coordinates are orthogonal, the transformation will be linear. There are three approaches to implement the linear transformation: Direction Cosines, Euler Angles (or Rotation Angles), and Quaternions. In this research, Quaternions is the main approach applied in the proposed algorithm and will be described in detail in the next section.

2.3.1 Direction Cosines

The direction cosines are used to define the angles between the three coordinate axes and a vector, which characterize the direction of the vector. To find the relationship between two frames, "A" and "B," let's consider that each frame is represented by orthogonal unit vectors $\vec{x}, \vec{y}, \vec{z}$. Each vector in the frame is defined by components x, y, and z. Therefore, the frames A and B are shown as the matrices in Equations 2.1 and 2.2.

$$A = [\,\vec{x}_A \;\; \vec{y}_A \;\; \vec{z}_A] = \begin{bmatrix} x_{A1} & x_{A2} & x_{A3} \\ y_{A1} & y_{A2} & y_{A3} \\ z_{A1} & z_{A2} & z_{A3} \end{bmatrix} \qquad (2.1)$$

$$B = [\,\vec{x}_B \;\; \vec{y}_B \;\; \vec{z}_B] = \begin{bmatrix} x_{B1} & x_{B2} & x_{B3} \\ y_{B1} & y_{B2} & y_{B3} \\ z_{B1} & z_{B2} & z_{B3} \end{bmatrix} \qquad (2.2)$$

Then the relationship between frame A and frame B is defined as C_B^A, where the original frame and the transformed frame are indicated in the lower index and upper index, respectively. C_B^A can be calculated using the dot product, which equals the cosine of the angle between the two-unit vectors. The direction cosine matrix is derived as the following equations.

$$A = C_B^A B \qquad (2.3)$$

$$C_B^A = AB^{-1} = \begin{bmatrix} \vec{x}_A \cdot \vec{x}_B & \vec{y}_A \cdot \vec{x}_B & \vec{z}_A \cdot \vec{x}_B \\ \vec{x}_A \cdot \vec{y}_B & \vec{y}_A \cdot \vec{y}_B & \vec{z}_A \cdot \vec{y}_B \\ \vec{x}_A \cdot \vec{z}_B & \vec{y}_A \cdot \vec{z}_B & \vec{z}_A \cdot \vec{z}_B \end{bmatrix} \qquad (2.4)$$

$$\begin{bmatrix} \vec{x}_A \cdot \vec{x}_B & \vec{y}_A \cdot \vec{x}_B & \vec{z}_A \cdot \vec{x}_B \\ \vec{x}_A \cdot \vec{y}_B & \vec{y}_A \cdot \vec{y}_B & \vec{z}_A \cdot \vec{y}_B \\ \vec{x}_A \cdot \vec{z}_B & \vec{y}_A \cdot \vec{z}_B & \vec{z}_A \cdot \vec{z}_B \end{bmatrix} = \begin{bmatrix} \cos\theta_{\vec{x}_A, \vec{x}_B} & \cos\theta_{\vec{y}_A, \vec{x}_B} & \cos\theta_{\vec{z}_A, \vec{x}_B} \\ \cos\theta_{\vec{x}_A, \vec{y}_B} & \cos\theta_{\vec{y}_A, \vec{y}_B} & \cos\theta_{\vec{z}_A, \vec{y}_B} \\ \cos\theta_{\vec{x}_A, \vec{z}_B} & \cos\theta_{\vec{y}_A, \vec{z}_B} & \cos\theta_{\vec{z}_A, \vec{z}_B} \end{bmatrix} \qquad (2.5)$$

The direction cosine matrix has these properties:

$$C(C)^T = I \implies C = C^{-1} = (C)^T \qquad (2.6)$$

The relative orientation is dominated by only three degrees of freedom due to the orthogonality assumption of the dependence among the nine elements in C.

Now, the relationship between frames A and B can be derived as Equations (2.7) to (2.9), following the properties above.

$$C_B^A = (C_B^A)^T \tag{2.7}$$

$$[\,\vec{x}_B \;\; \vec{y}_B \;\; \vec{z}_B]^T = C_B^A[\,\vec{x}_A \;\; \vec{y}_A \;\; \vec{z}_A]^T \tag{2.8}$$

$$[\,\vec{x}_A \;\; \vec{y}_A \;\; \vec{z}_A]^T = C_B^A\,[\,\vec{x}_B \;\; \vec{y}_B \;\; \vec{z}_B]^T \tag{2.9}$$

2.3.2 Euler Angles and Euler Rotation

Euler angles are common systems that describe the orientation relation of two frames in three-dimensional Euclidean space by a sequence of rotations. These coordinate frames are successfully transformed using the rotation matrices about specific axes. These rotations around axes follow the direction cosine matrix for a right-handed (counterclockwise) rotation, creating the rotational angles or Euler angles as ϕ, θ, and ψ for the x-axis, y-axis, and z-axis, respectively. Therefore, the rotation matrices of a coordinate frame are as follows:

$$R_x(\phi) = \begin{bmatrix} 1 & 0 & 0 \\ 0 & \cos(\phi) & \sin(\phi) \\ 0 & -\sin(\phi) & \cos(\phi) \end{bmatrix} \tag{2.10}$$

$$R_y(\theta) = \begin{bmatrix} \cos(\theta) & 0 & \sin(\theta) \\ 0 & 1 & 0 \\ -\sin(\theta) & 0 & \cos(\theta) \end{bmatrix} \tag{2.11}$$

$$R_z(\psi) = \begin{bmatrix} \cos(\psi) & -\sin(\psi) & 0 \\ \sin(\psi) & \cos(\psi) & 0 \\ 0 & 0 & 1 \end{bmatrix} \tag{2.12}$$

A 3-by-3 rotational matrix ‘R’ is used to multiply with a 3-by-1 coordinate vector in order to rotate a primary vector in three-dimensional space. The new vector can be obtained from Equation (2.13).

$$\vec{V}_2 = R\,\vec{V}_1$$

$$\begin{bmatrix} v_{2x} \\ v_{2y} \\ v_{2z} \end{bmatrix} = \begin{bmatrix} r_{11} & r_{12} & r_{13} \\ r_{21} & r_{22} & r_{23} \\ r_{31} & r_{32} & r_{33} \end{bmatrix} \begin{bmatrix} v_{1x} \\ v_{1y} \\ v_{1z} \end{bmatrix} \qquad (2.13)$$

To prove Euler's Theorem, that states: "*Any two independent orthogonal coordinate frames can be related by a sequence of rotations (not more than three) about coordinate axes, where no two successive rotations may be about the same axis"* [56], there are twelve different independent rotation sequences in three Euclidean axes, which are:

xyx xyz xzx xzy

yxy yxz yzx yzy

zxy zxz zyx zyz

In the global coordinate frame, the rotation about the x-axis is called 'roll', the rotation about the y-axis is called 'pitch', and the rotation about the z-axis is called 'yaw'. The Euler angle-axis sequence ZYX is commonly used to describe rotations in the aerospace field for tracking the aircraft's heading and attitude. The global rotation matrix is shown in the following equations:

$$R_{zyx} = R_z(\psi)R_y(\theta)R_x(\phi) \qquad (2.14)$$

$$= \begin{bmatrix} \cos(\psi) & -\sin(\psi) & 0 \\ \sin(\psi) & \cos(\psi) & 0 \\ 0 & 0 & 1 \end{bmatrix} \left(\begin{bmatrix} \cos(\theta) & 0 & \sin(\theta) \\ 0 & 1 & 0 \\ -\sin(\theta) & 0 & \cos(\theta) \end{bmatrix} \begin{bmatrix} 1 & 0 & 0 \\ 0 & \cos(\phi) & \sin(\phi) \\ 0 & -\sin(\phi) & \cos(\phi) \end{bmatrix} \right)$$

$$= \begin{bmatrix} \cos(\psi)\cos(\theta) & \cos(\psi)\sin(\theta)\sin(\phi) - \cos(\phi)\sin(\psi) & \sin(\psi)\sin(\phi) + \cos(\psi)\cos(\phi)\sin(\theta \\ \cos(\theta)\sin(\psi) & \cos(\phi)\cos(\psi) + \sin(\theta)\sin(\phi)\sin(\psi) & \cos(\phi)\sin(\theta)\sin(\psi) - \cos(\psi)\sin(\phi) \\ -\sin(\theta) & \cos(\theta)\sin(\phi) & \cos(\theta)\cos(\phi) \end{bmatrix}$$

This rotation matrix R_{abc} where a, b, and c can be any x, y, and z are an alternative transformation of the direction cosine matrix but expressed in the Euler angles form.

Even though the direct cosine matrix and Euler angles are very straightforward and clearly describing the rotation transformation in three-dimensional space, there is a

weakness in this approach. When the pitch angle approaches +/- 90 degrees and causes the loss of one degree of freedom in a three-dimensional space, the phenomenon called "Gimbal lock" occurs. Gimbal lock happens when the axis of the first rotation is parallel to the third rotation axis and becomes a system in two-dimensional space. The gimbal lock blocks the possibility of finding the individual angles for each of the axes. To avoid the gimbal lock disadvantage, quaternions were introduced to express rotations in three-dimensional space.

2.4 Quaternions

2.4.1 Quaternion Definition

Quaternion were first proposed by an Irish mathematician, William R. Hamilton, in 1843 [57]. A quaternion is a combination of a real number and three imaginary components which makes it a hyper-complex number. A quaternion 'q' can be denoted in different ways. For the orthogonal basis in R^3, a quaternion is defined as the grouping of a vector $\vec{q}$ in three-dimensional space and a scalar q_w, as shown in Equation 2.15.

$$q = \vec{q} + q_w = q_x\hat{\imath} + q_y\hat{\jmath} + q_z\hat{k} + q_w \qquad (2.15)$$

In the previous Equation, q_x , q_y , q_z ,*and* q_w are all real numbers. Therefore, the quaternion can turn to be the orthogonal basis of R^4 simply defined using only those four scalar quantities, as shown in Equation 2.16. This definition and arrangement of quaternion will be used throughout this research.

$$q = [q_x , q_y , q_z , q_w] \quad (2.16)$$

2.4.2 Basic Definitions and Properties of Quaternions

Hence, $a = a_x\hat{\imath} + a_y\hat{\jmath} + a_z\hat{k} + a_w$ and $b = b_x\hat{\imath} + b_y\hat{\jmath} + b_z\hat{k} + b_w$ are quaternions.

Addition : The addition of two quaternions is a quaternion.

The sum of $a\ and\ b$ is defined by Equation 2.17.

$$a + b = (a_x + b_x)\,\hat{\imath} + (a_y + b_y)\hat{\jmath} + (a_z + b_z)\hat{k} + (a_z + b_z) \qquad (2.17)$$

Multiplication : The multiplication of a quaternion with a scalar is a quaternion. Let *c* be a scalar. Equation 2.18 shows the multiplication of a quaternion and a scalar.

$$ca = (ca_x)\hat{\imath} + (ca_y)\hat{\jmath} + (ca_z)\hat{k} + (ca_w) \qquad (2.18)$$

Also, the multiplication of two quaternions is a quaternion. However, the fundamental products of the elements $\hat{\imath}, \hat{\jmath}, and\ \hat{k}$ must be considered as in Equations 2.19 to 2.22.

$$\hat{\imath}^2 = \hat{\jmath}^2 = \hat{k}^2 = \hat{\imath}\hat{\jmath}\hat{k} = -1 \qquad (2.19)$$

$$\hat{\imath}\hat{\jmath} = \hat{k} = -\hat{\jmath}\hat{\imath} \qquad (2.20)$$

$$\hat{\jmath}\hat{k} = \hat{\imath} = -\hat{k}\hat{\jmath} \qquad (2.21)$$

$$\hat{k}\hat{\imath} = \hat{\jmath} = -\hat{\imath}\hat{k} \qquad (2.22)$$

The product of two quaternions is indicated using the symbol '⊗'. Equation 2.23 defines the product of two quaternions.

$$\begin{aligned} a \otimes b &= \left(a_x\hat{\imath} + a_y\hat{\jmath} + a_z\hat{k} + a_w\right)\left(b_x\hat{\imath} + b_y\hat{\jmath} + b_z\hat{k} + b_w\right) \\ &= a_x b_x\hat{\imath}^2 + a_x b_y\hat{\imath}\hat{\jmath} + a_x b_z\hat{\imath}\hat{k} + a_x b_w\hat{\imath} \\ &\quad + a_y b_x\hat{\jmath}\hat{\imath} + a_y b_y\hat{\jmath}^2 + a_y b_z\hat{\jmath}\hat{k} + a_y b_w\,\hat{\jmath} \\ &\quad + a_z b_x\hat{k}\hat{\imath} + a_z b_y\hat{k}\hat{\jmath} + a_z b_z\hat{k}^2 + a_z b_w\,\hat{k} \\ &\quad + a_w b_x\hat{\imath} + a_w b_y\hat{\jmath} + a_w b_z\hat{k} + a_w b_w \end{aligned} \qquad (2.23)$$

Note that, the quaternions multiplication is non-commutative.

By applying the fundamental rules, the product of two quaternion can be simplified and rewritten as Equation 2.24.

$$a \otimes b = a_w b_w - \left(a_x b_x + a_y b_y + a_z b_z\right) + a_w\left(b_x\hat{\imath} + b_y\hat{\jmath} + b_z\hat{k}\right) + b_w\left(a_x\hat{\imath} + a_y\hat{\jmath} + a_z\hat{k}\right) + \left(a_y b_z - a_z b_y\right)\hat{\imath} + (a_x b_z - a_z b_x)\hat{\jmath} + (a_x b_y - a_y b_x)\hat{k} \qquad (2.24)$$

The quaternion multiplication can also be written in matrix form by grouping the coefficients for each component: $\hat{\imath}, \hat{\jmath}, \hat{k}$ and real part together using Equation 2.23.

$$a \otimes b = \begin{bmatrix} b_w & b_z & -b_y & b_x \\ -b_z & b_w & b_x & b_y \\ b_y & -b_x & b_w & b_z \\ -b_x & -b_y & -b_z & b_w \end{bmatrix} \begin{bmatrix} a_x \\ a_y \\ a_z \\ a_w \end{bmatrix} \qquad (2.25)$$

Conjugation : A quaternion *a* can define a conjugate *a** as in Equation 2.26.

$$a^* = -a_x\hat{\imath} - a_y\hat{\jmath} - a_z\hat{k} + a_w \qquad (2.26)$$

Norm : The norm of a quaternion is scalar, denoted by ||*a*||. It is simply described as the square root of the sum of each component squared, as shown in Equations 2.27 and 2.28.

$$\|a\| = \sqrt{a^* \otimes a} \qquad (2.27)$$

$$\|a\| = \sqrt{a_x^2 + a_y^2 + a_z^2 + a_w^2} \qquad (2.28)$$

Unit quaternion : If the quaternion *a* is a unit quaternion, denoted as '*u*', then the norm is equal to 1, $\|u\| = 1$. Equation 2.29 defines a unit quaternion *u* which equals the multiplication of the inverse norm of quaternion *a*, $\left(\frac{1}{\|a\|}\right)$, and that quaternion *a*.

$$u = \frac{1}{\|a\|}\left(a_x\hat{\imath} + a_y\hat{\jmath} + a_z\hat{k} + a_w\right) \qquad (2.29)$$

Inverse : The inverse of a quaternion *a* is defined as in Equation 2.30, where $a^{-1}a = aa^{-1}$. In this case, *a* is a unit quaternion, and therefore the inverse is its conjugate *a**.

$$a^{-1} = \frac{a^*}{\|a\|^2} \qquad (2.30)$$

Exponential : The exponential of a quaternion is denoted by e^a as shown in Equation 2.31. The scalar quantity of the quaternion a^w can directly apply the exponential rule. However, the vector quantity of quaternion $\vec{a}$ is derived through the Taylor series expansion for the exponential function. The final result is shown in Equation 2.32, s

acquired from O-larnnithipong [58], which applied Taylor series expansion formulas for sine and cosine.

$$e^{a} = e^{(\vec{a}+a_w)} = e^{\vec{a}}e^{a_w} \tag{2.31}$$

$$e^{a} = e^{a_w}\left(\frac{\vec{a}}{\|\vec{a}\|}\sin(\|\vec{a}\|) + \cos(\|\vec{a}\|)\right) \tag{2.32}$$

2.4.3 Quaternion Transformations

The previous section has explained most of the essential basics of quaternion algebra. Now we will apply those basic equations to perform a three-dimensional rotation using quaternions. The simple rotation of a point, or a vector within one coordinate frame, can be obtained as in Equation 2.33 where the $\vec{v}$ is a vector, in three-dimension space and $\vec{w}$ is a rotated vector with angle of θ around an axis in the same reference frame.

$$\vec{w} = q \otimes \vec{v} \otimes q^{*} \tag{2.33}$$

Where, q is a unit quaternion (i.e., norm $\|q\|$ equal to 1).

Previously, the rotation of Frame A with respect to Frame B, was denoted as R_B^A. This is equivalent to $\vec{q}_B^A$ in terms of quaternions. One property of rotating a reference coordinate frame with respect to another coordinate frame is that the rotation of frame "A" with respect to frame "B" can be paired with the rotation of frame "B" with respect to frame "A" depending on the point of view. Therefore, the quaternion $\vec{q}_B^A$ is equal to the quaternion $\vec{q}_A^B$ in counter-rotation, as shown in Equation 2.34. Then Equations 2.35 and 2.36 describe the relationship of vector $\vec{v}_A$ and $\vec{v}_B$ referenced in frame "A" and "B", respectively.

$$\vec{q}_A^B = \vec{q}_B^{A*} \quad \text{or} \quad \vec{q}_B^A = \vec{q}_A^{B*} \tag{2.34}$$

$$\vec{v}_B = \vec{q}_A^B \otimes \vec{v}_A \otimes \vec{q}_A^{B*} \tag{2.35}$$

$$\vec{v}_B = \vec{q}_B^{A*} \otimes \vec{v}_A \otimes \vec{q}_B^A \tag{2.36}$$

According to the multiplication rule for quaternions, the R^3 vectors $\vec{v}_A$ and $\vec{v}_B$ must be transformed into quaternion space R^4. First, the three components of the R^3vector become the three imaginary elements, in the $\hat{\imath}, \hat{\jmath}, and\ \hat{k}$ directions. Then a zero real part is added. Equation 2.37 represents any vector $\vec{v}$ in the form of quaternion space.

$$\vec{v} \in R^4 = \vec{v} + 0 = v_x\hat{\imath} + v_y\hat{\jmath} + v_z\hat{k} + 0 = \left[v_x, v_y, v_z, 0\right] \qquad (2.37)$$

This type of quaternion, with zero real part is called a 'pure quaternion'.

Equation 2.38 shows the unit quaternion 'q' as a rotation operator which is written in trigonometrical form. The symbol θ represent a half of the rotating angle about the unit vector $\vec{u}$ (rotational axis).

$$q = \vec{q} + q_w = \vec{u}\sin(\theta) + \cos(\theta) \qquad (2.38)$$

Knowing the desired axis of rotation and the angle to be rotated, the process for representing the desired rotation with quaternions is better explained considering the initial and final positions of the rotated vector as existing in a common plane. The angular relationship involved in a rotation represented by a quaternion product can be found recalling the dot product and cross product of two vectors as shown in the Equations 2.39 and 2.40, respectively, where $\vec{a}$ and $\vec{b}$ are the two vectors in three-dimensional space and 2θ is the angle between them.

$$\vec{a} \times \vec{b} = \|\vec{a}\|\left\|\vec{b}\right\| \sin(2\theta)\,\vec{n} \qquad (2.39)$$

$$\vec{a} \cdot \vec{b} = \|\vec{a}\|\left\|\vec{b}\right\| \cos(2\theta) \qquad (2.40)$$

Let $\vec{n}$ be a unit quaternion where its norm squared equals to 1. After solving algebraic equations, the unit quaternion *'q''* in Equation 2.41 then represents the rotation of angle 2θ about $\vec{n}$ and describes the angular difference between two vectors $\vec{a}$ and $\vec{b}$.

$$q' = \vec{a} \times \vec{b} + (\vec{a} \cdot \vec{b} + \|\vec{a}\|\left\|\vec{b}\right\|) \qquad (2.41)$$

The $\vec{a} \times \vec{b}$ portion contains the vector part $\vec{q}$ of the quaternion where $(\vec{a} \cdot \vec{b} + \|\vec{a}\|\|\vec{b}\|)$ portion is the scalar part q_w. Then we can rewrite the equation as in Equation 2.42.

$$q' = \Delta q = \mathrm{H}(\vec{q}, q_w) \qquad (2.42)$$

2.4.4 Conversion between Euler Angles and Quaternion.

To better describe 3-D angles and perform rotations, it is necessary to be able to convert back and forth between Euler Angles and Quaternions.

Firstly, the angles Phi (ϕ), Theta (θ) and Psi (ψ) represent the value of the angles rotated about axis x, y and z respectively in the Euler Angles method. Therefore, Equations 2.43 to 2.45 show how to convert angles for each orthogonal axis into quaternion form.

$$q_{\phi}^{\hat{\imath}} = \cos\left(\frac{\phi}{2}\right) + \hat{\imath}\sin\left(\frac{\phi}{2}\right) \qquad (2.43)$$

$$q_{\theta}^{\hat{\jmath}} = \cos\left(\frac{\theta}{2}\right) + \hat{\jmath}\sin\left(\frac{\theta}{2}\right) \qquad (2.44)$$

$$q_{\psi}^{\hat{k}} = \cos\left(\frac{\psi}{2}\right) + \hat{k}\sin\left(\frac{\psi}{2}\right) \qquad (2.45)$$

The common Euler angle-axis sequence used to describe a rotation in the aerospace field is ZYX. Then, Equations 2.46 and 2.47 construct the quaternion rotation of 'q' according to that sequence.

$$q = q_{\psi}^{\hat{k}} \otimes q_{\theta}^{\hat{\jmath}} \otimes q_{\phi}^{\hat{\imath}} \qquad (2.46)$$

$$q = q_x\hat{\imath} + q_y\hat{\jmath} + q_z\hat{k} + q_w \qquad (2.47)$$

Given that,

$$q_x = \cos\left(\frac{\psi}{2}\right)\cos\left(\frac{\theta}{2}\right)\sin\left(\frac{\phi}{2}\right) - \sin\left(\frac{\psi}{2}\right)\sin\left(\frac{\theta}{2}\right)\cos\left(\frac{\phi}{2}\right)$$

$$q_y = \cos\left(\frac{\psi}{2}\right)\sin\left(\frac{\theta}{2}\right)\cos\left(\frac{\phi}{2}\right) + \sin\left(\frac{\psi}{2}\right)\cos\left(\frac{\theta}{2}\right)\sin\left(\frac{\phi}{2}\right)$$

$$q_z = \sin\left(\frac{\psi}{2}\right)\cos\left(\frac{\theta}{2}\right)\cos\left(\frac{\phi}{2}\right) - \cos\left(\frac{\psi}{2}\right)\sin\left(\frac{\theta}{2}\right)\sin\left(\frac{\phi}{2}\right)$$

$$q_w = \cos\left(\frac{\psi}{2}\right)\cos\left(\frac{\theta}{2}\right)\cos\left(\frac{\phi}{2}\right) + \sin\left(\frac{\psi}{2}\right)\sin\left(\frac{\theta}{2}\right)\sin\left(\frac{\phi}{2}\right)$$

After the quaternion is calculated and used to rotate the vector, Equations 2.48 to 2.50 can be used to convert a unit quaternion 'q' back into the Euler angles.

Angle rotate about x-axis; $$\psi = tan^{-1}\left[\frac{2(q_w q_z + q_x q_y)}{1-2(q_y^2+q_z^2)}\right] \quad (2.48)$$

Angle rotate about y-axis; $$\theta = sin^{-1}\left[2(q_w q_y + q_x q_z)\right] \quad (2.49)$$

Angle rotate about z-axis; $$\phi = tan^{-1}\left[\frac{2(q_w q_x + q_y q_z)}{1-2(q_x^2+q_y^2)}\right] \quad (2.50)$$

CHAPTER 3 – MEMS MAGNETIC, ANGULAR-RATE, GRAVITY (MARG) SENSORS

Micro-electromechanical Systems or MEMS were first introduced in the 1950's and further developed to be widely used in commercial products in the mid-1990's [59] [60]. A MEMS system is a small integrated device that consists of mechanical and electrical components. It is mostly made from the silicon material which is the same type of an electrical processor found in the computers. MEMS can be constructed to use in various systems such as temperature control, air pressure control, force control, etc. MEMS have significant advantages, such as their small sizes, low power consumption and low in cost of manufacturing. Nevertheless, the data obtained from MEMS have errors and noises that require calibrations and filtering processes. One type of MEMS systems that is commonly used in tracking motion or for navigation are called MEMS inertial sensors or inertial measurement units (IMUs).

An inertial measurement unit is a measurement electronic device composed of an accelerometer and a gyroscope sensor. This device may be used to capture the motion of the body. Some IMUs may include magnetometers for better measuring results. The combination of three sensors creates a 9-degree of freedom system. IMUs are commonly used in the attitude and heading reference system for ships and aircraft. With the current technological developments, the IMU model, which are smaller in size and cheaper, are available in the market. This increases the number of applications using IMUs, such as in the mobile telephony field.

3.1 Gyroscopes

A gyroscope is a device used to measure orientation and angular velocity. It is originally a spinning disc able to spin rapidly about an axis which is itself free to alter

its direction. With the conservation of angular momentum, the orientation of the axis is not affected by tilting of the mounting and it is able to maintain its spinning axis. While the wheel is spinning along the spin axis, if there is a rotational force applied to the input axis, the rotational force will show about the output axis, which is perpendicular to the plane of the spinning and input axes according to the right-hand rule. This occurrence is known as "Gyroscopic Effect".

MEMS gyroscopic sensors are not composed by spinning discs or gimbals. Instead, they use the concept of the Foucault pendulum, the Coriolis effect [61] and apply it to a vibrating mechanism to detect the changes in orientation. When a mass is driven constantly at velocity $\vec{v}$, and an external angular rate $\vec{\Omega}$ is applied, the flexible part of the proof mass would vibrate out of the plane and create a perpendicular displacement known as the Coriolis forces ($\vec{F}_{Coriolis}$), sensed capacitively with a specific CMOS ASIC. This type of MEMS gyroscopes is called "Tuning Fork Gyroscopes" where the comb-type structures drive the turning fork into resonance. Equation 3.1 represents the relationship between the driven velocity and the angular velocity.

$$\vec{F}_{Coriolis} = -2m\vec{\Omega} \times \vec{v} \qquad (3.1)$$

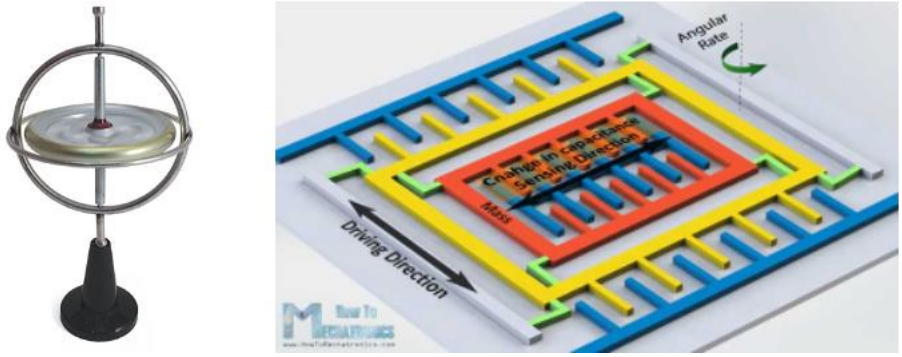

Figure 3.1A classic gyroscope (left), A structure of MEMS gyroscope from Howtomechatronics.com [62] (right).

3.2 Accelerometers

An accelerometer is a device that is used to measure the rate of change of velocity, known as acceleration, that is applied to a body. The amount of acceleration is the combination from two types of acceleration forces: dynamic forces (external forces act to produce linear motion) and static forces (the Earth's gravity). Some examples of MEMS accelerometers are piezo-electric, piezo-resistance and capacitive. For consumer grade accelerometer (low cost), MEMS capacitive accelerometers are commonly used over other types [63]. Figure 3.2 shows the microstructure of MEMS capacitive accelerometers. They consist of two main parts, which are static and dynamic. The static part is constituted by fixed electrodes and the dynamic part has a flexible spring leg attached with a movable proof mass. At rest position (no applied acceleration), the gap between the left side of a fixed plate and the movable part (d_1) equals the gap on the right side (d_2). When the acceleration is applied, the distance between both gaps changes in the direction of the force applied. Therefore, the output signal of MEMS capacitive accelerometer is generated from the change of capacitance between the fixed and the moving mass electrodes. With today's technology, a MEMS accelerometer consists of 3 axes placed orthogonally.

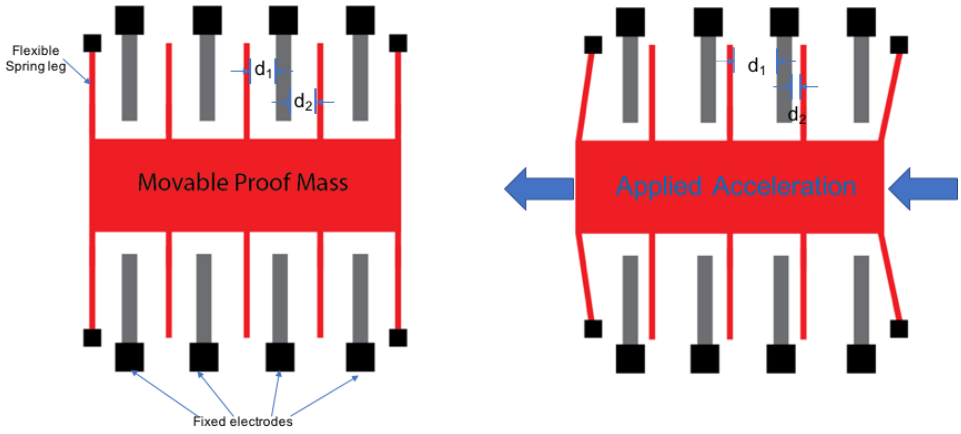

Figure 3.2Micro-structure of MEMS accelerometer, at rest position (left) and applied acceleration (right).

3.3 Magnetometers

A magnetometer can be used to measure the direction and strength or the change in a magnetic field. A compass is a classic analog device that provides an output indicating the direction of the ambient Earth's magnetic field. A German mathematician and physicist, Johann Carl Friedrich Gauss, introduced the magnetometer in 1833 [64]. Then in the 19th century, magnetometers were develop using the Hall effect, which is the most common method until today.

The Hall effect or Magneto Resistive Effect uses a thin metallic plate with electric current flowing through it. When a strong magnetic field passes through the plate, in a perpendicular direction, a voltage called 'Hall voltage', is generated, as shown in Figure 3.3. The intensity and direction of the magnetic field will disturb the flow of electrons to one side of the plate, which results in the Hall voltage.

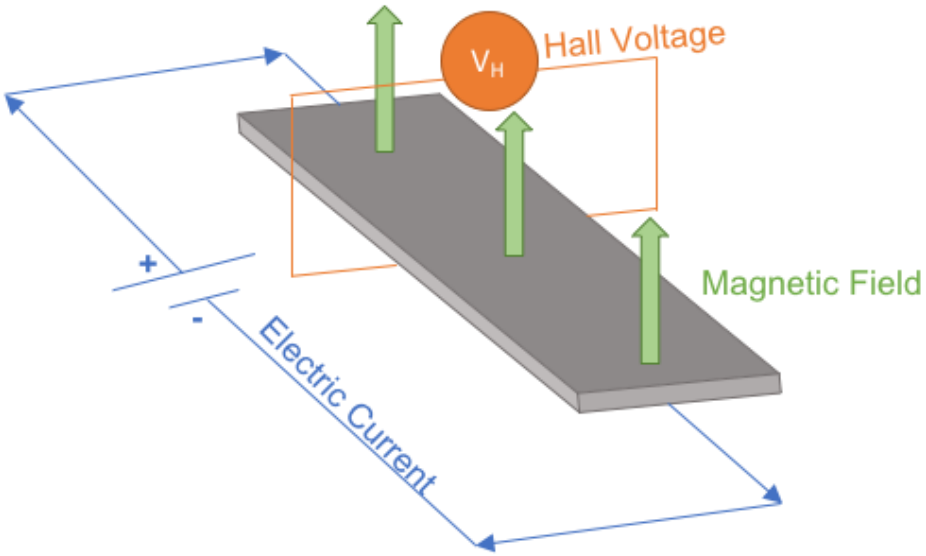

Figure 3.3The Hall Effect principle.

3.4 Errors and Limitations in MEMS Inertial Sensors

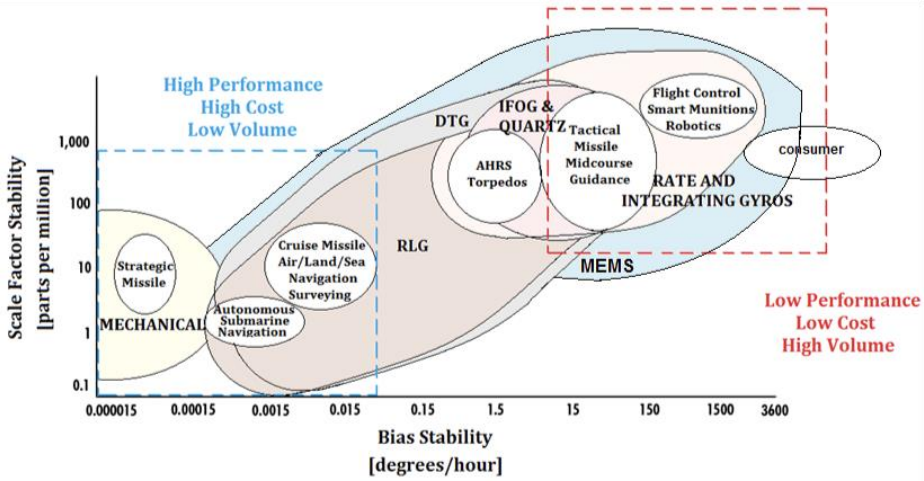

Figure 3.4Types of Inertial sensors based on their bias Stability and Scale Factor stability. [65]

Inertial sensors have different types according to their performance and costs. MEMS Inertial Sensors are commonly used for the commercial applications due to their low cost and small size. However, they generate significant amounts of errors in their measurement. Figure 3.4 shows a graph mapping different types of Inertial Sensors with respect to their errors. The errors in commercial grade MEMS have 2 main categories, which are Systematic errors (deterministic) and Stochastic errors (random). To improve the performance of low-cost MEMS, any error from the sensor that affects the accuracy of the measurement needs to be addressed.

3.4.1 Gyroscopes Errors

The raw drift on the gyroscope of the MEMS module used in this research is rated by the manufacturer as 11º/hour, but the actual error measured from a module at the FIU DSP Lab was 55.2º/hour [66].

The drift error phenomenon involves both types of errors, Systematic and Stochastic. The Systematic errors are the module defects created in the manufacturing process and can be predicted, for example Bias offset error, Thermal, Repeatability,

Scale factor, and non-orthogonality. These types of errors can be calibrated from the raw gyroscope data using pre-assigned mathematical models.

The bias offset error is specifically targeted by the proposed algorithm. The inertial sensors should, ideally, give zero output when they are in their static states and no input forces are applied. However, even in a static state, the low-cost MEMS provide some negative and positive values that deviate from zero, called “offset”, as shown in Figure 3.5 (top). Once the raw gyroscope data is integrated to obtain the angle of the sensor shown in Figure 3.5 (bottom), the angle output from the offset value shows a pattern that can be fixed using mathematical models. An angle error (θ_e) from the bias offset of gyroscope is proportional to the time (t) as shown in Equation 3.1, where b_w is the bias offset error magnitude.

$$\theta_e = \int (b_w) dt = b_w t \qquad (3.1)$$

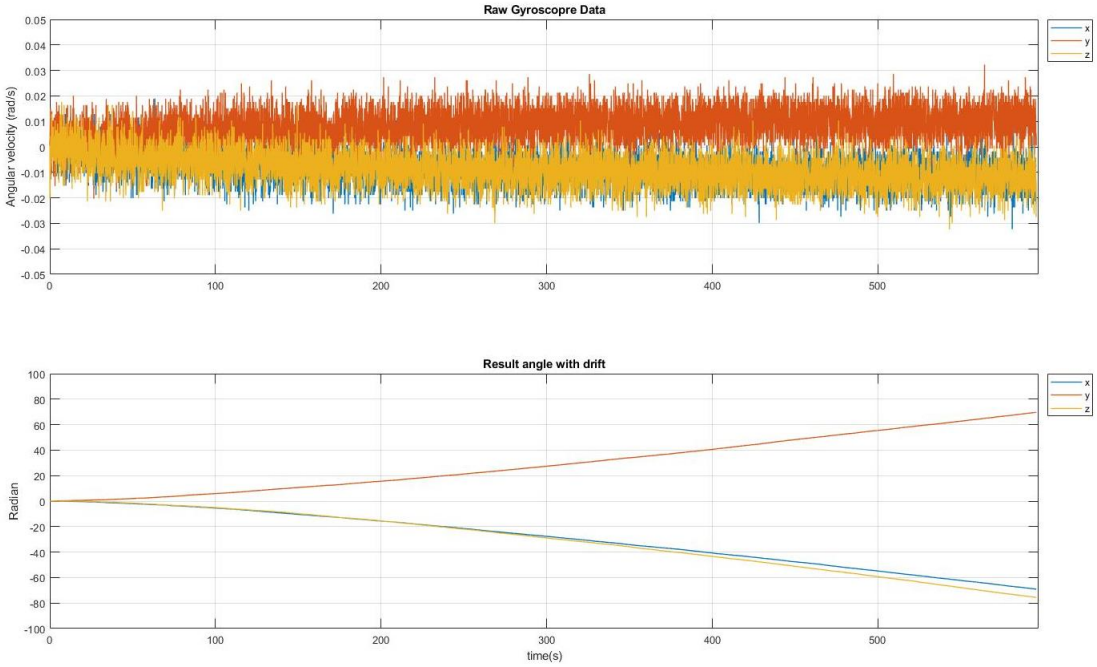

Figure 3.5(Top) Raw gyroscope with Bias offset error. (Bottom) Integrated result in angle with drift.

In addition to the bias offset error, Stochastic errors or Random errors are the major cause of drift in the output of the sensor. The Stochastic errors are randomly

created over time and cannot be predicted or determined by fixed models. There are some types of random process that can be used to describe the random errors of the sensors.

The Gaussian Random process is a common process used to define a common type of random error. It is described by the normal distribution of x(t) for any time (t) using its probability density function, as shown in Equation 3.2.

$$f[x(t)] = \frac{1}{\sigma\sqrt{2\pi}} e^{-\frac{1}{2}\left(\frac{x-\mu}{\sigma}\right)^2} \qquad (3.2)$$

The random walk process is another random process that may be applied to model the inertial sensor's errors. Equation 3.3 describes the relationship of a random variable $\dot{b}(t)$ and a white noise process $w(t)$ integrated.

$$\dot{b}(t) = w(t) \qquad (3.3)$$

This output white noise from the MEMS will be integrated into velocity and angle errors known as "velocity random walk (VRW)" and "angular random walk (ARW)".

To obtain more accurate outputs, those random errors needed to be addressed. The research reported in this dissertation takes advantage of the diversity of sensors in the MEMS module, using two other types of sensors included in the module, accelerometers, and magnetometers, to compensate errors. Accelerometers and magnetometers sensors also give output in angular formats. Therefore, the gyroscope drift from random error can be detected and corrected by comparison to the angular results of the other sensors. By correcting the error directly to its output, all noises and errors involved in the MEMS sensor will be comprehensively addressed.

3.4.2 Limitations of Accelerometers

The accelerometers measure the rate of change of velocity produced by both dynamic forces (external forces that act to produce linear motion) and static forces (the Earth's gravity), as describe in Section 3.2. The proposed algorithm uses the exclusive acceleration due to the gravity while the module is static, or near static to predict and compensate the output angle of the MEMS module. The vector measured from gravity always points vertically and in a downward direction, to the center of the Earth, in the Earth frame. It is necessary to restrict the use of accelerometer correction only to time interval when the MEMS module is static, and no force is applied to the sensor.

3.4.3 Limitations of Magnetometers

To correct the gyroscope drift while the sensor is moving, the use of magnetometers is an alternative option. The algorithm uses the magnetic North vector measured by the magnetometers in the MEMS module as the reference to correct the estimated output angle of the sensor. However, the magnetometers measure the direction and strength or the change in a magnetic field. Therefore, the proximity of large ferromagnetic objects; such as metal desk, electronic devices, metal shelves, etc., in the working area can cause distortions in the local magnetic field.

A study of the distortion of the magnetic field in the proposed experimental area was conducted, in order to assess the level of trustworthiness of using magnetometers as a means for gyroscope drift correction. The experiment was set up as shown in Figure 3.6(a). The non-ferromagnetic frame was built to create a 5'x5'x5' grid with 1' spacing in all 3 directions. Figure 3.6(b) shows the result of mapping the magnetic North vector within the grid. The level of consistency of those distortions through time was also captured during this experiment, as show in Figure 3.7.

The results show that ferromagnetic objects do affect the magnetic field and cause the magnetic north vector to be distorted. In this working space, the metal desk is the key object causing the most significant distortion of the magnetic field.

In the space regions where the magnetic field is distorted, the correction of the module orientation errors cannot be applied directly [67].

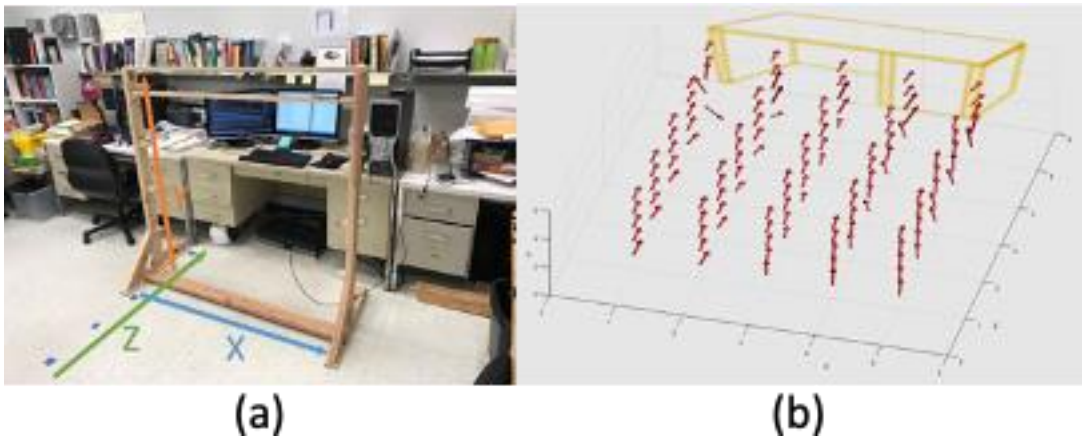

Figure 3.6 (a) Office environment space where the experiment took place.(b) 3D plot of Magnetic Vector recordings in the 5x5x5 Dense Grid (separation between nodes in 1' in all directions)

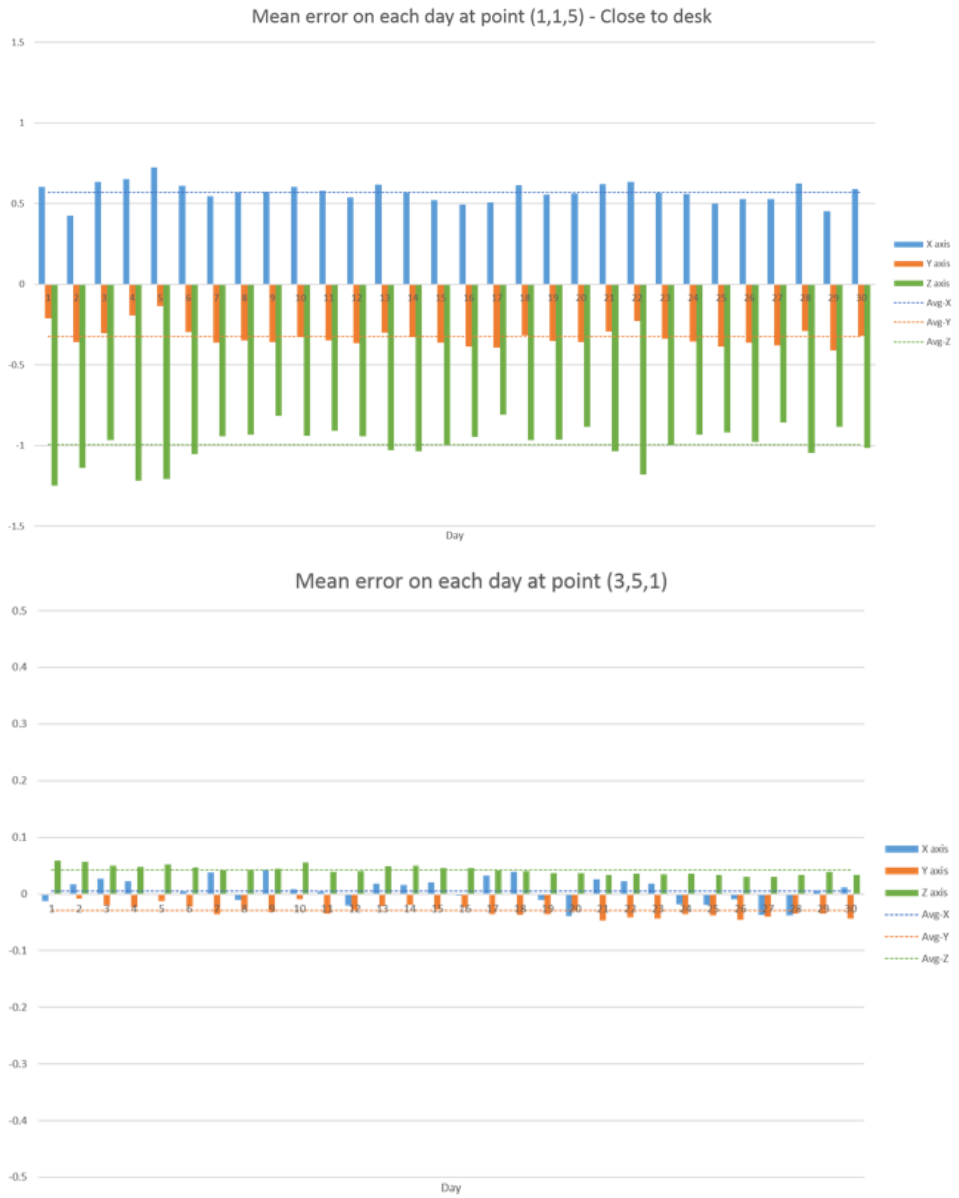

Figure 3.7The bar chart of mean error at the most critical point (1,1,5) compared with the least critical point (3,5,1) from day 1 to day 30.

CHAPTER 4 - SENSOR FUSION AND ORIENTATION CORRECTION ALGORITHM

4.1 Gravity-Magnetic Vector Compensation (GMV)

The Gravity-Magnetic Vector Compensation (GMV) approach was introduced by O-larnithipong [50]. He created an algorithm that used the benefit of sensor fusion to solve the drift problem commonly present in obtained from the low-cost gyroscope sensors. His algorithm has the flow as described in Figure 4.1.

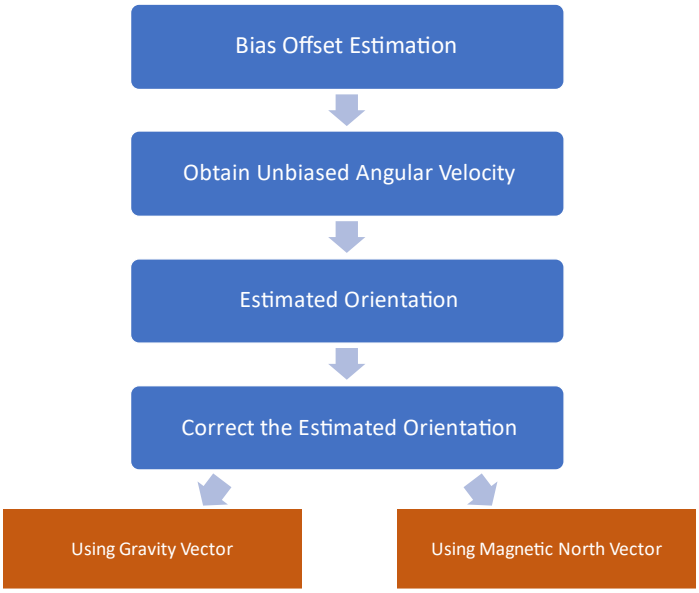

Figure 4.1The flow chart explained Gravity-Magnetic Vector Compensation (GMV) Algorithm.

Firstly, the Bias Offset was estimated. This includes the bias error generated from manufacturing defects. In this algorithm, the bias offset error is assessed for every sampling data to prepare for calculation of an unbiased angular velocity ($\vec{\omega}_B$), which will be used in the algorithm. The simple linear regression model [68] was applied to determine the bias offset error and use the Equations (4.1) – (4.4) were used to obtain the unbiased angular velocity ($\vec{\omega}_B$) by subtracting the raw gyroscope data with calculated bias offset error from the raw gyroscope data.

$$\hat{b} = \beta_0 + \beta_1 t \quad (4.1)$$

$$\beta_0 = \bar{b} - \beta_1 \bar{t} \quad (4.2)$$

$$\beta_1 = \frac{\sum_{t=1}^{n}(t_i - \bar{t})(b_i - \bar{b})}{\sum_{t=1}^{n}(t_i - \bar{t})^2} \quad (4.3)$$

Then; $$\vec{\omega}_B = \vec{\omega}_0 - \hat{b} \quad (4.4)$$

Where, $\vec{\omega}_0$ is the raw gyroscope reading from the sensor.

This algorithm mainly used quaternion notation to represent the rotation, which avoids ambiguities created by the gimbal lock problem. The unbiased angular velocity ($\vec{\omega}_B$) in R3 is transformed into the quaternion space, R4, by augmenting a zero as the fourth component of the quaternion. The quaternion rate (q) is calculated using the zero degree or initial state of a quaternion as [0,0,0,1] and the value of unbiased angular velocity ($\vec{\omega}_B$) in quaternion form as shown in Equation (4.5). This Equation can also be written in a matrix form, Equation (4.6).

$$\dot{q} = \frac{1}{2}\hat{q}_0 \otimes \vec{\omega}_B \quad (4.5)$$

$$\dot{q} = \frac{1}{2}\begin{bmatrix} 0 & \omega_{Bz} & -\omega_{By} & \omega_{Bx} \\ -\omega_{Bz} & 0 & \omega_{Bx} & \omega_{By} \\ \omega_{By} & -\omega_{Bx} & 0 & \omega_{Bz} \\ -\omega_{Bx} & -\omega_{By} & -\omega_{Bz} & 0 \end{bmatrix}\begin{bmatrix} \hat{q}_{0x} \\ \hat{q}_{0y} \\ \hat{q}_{0z} \\ \hat{q}_{0w} \end{bmatrix} \quad (4.6)$$

The estimated orientation (q_G) is calculated from Equation (4.7) using the integration method, where the rate (Δt) is from the sampling interval used by the IMU. By integrating the quaternion rate, the orientation of the sensor module was obtained from its initial position.

$$q_G = e^{((\Delta t)\dot{q} \otimes \hat{q}_0^*) \otimes \hat{q}_0} \quad (4.7)$$

This proposed method's main goal is to correct the drift error from the gyroscope and its impact on the estimated orientation (q_G). Two additional sensing units, which are accelerometers and magnetometers, are used for that purpose. The output from the

accelerometer ideally results from the acceleration due to the gravity, called "gravity vector." Simultaneously, the magnetometer measuring the "magnetic North vector" represents the direction of the Earth's magnetic field. The concept of comparing between the sensor's body frame and the Earth's frame was applied to calculate the module's orientation using these two sensing units, as indicated by Equation (4.8).

The vector in the sensor's body frame can be expressed as ${}^{B}\vec{v}$, which uses the triple-product quaternion operator shown in Equation (4.9). By referring to Equation (4.8), the ${}^{B}\vec{v}$ can be calculated using only a unit quaternion representing the sensor's body frame orientation, with respect to the earth's frame, created in Equation (4.10).

$$ {}^{B}_{E}q = {}^{E}_{B}q^{*} \qquad (4.8) $$

$$ {}^{B}\vec{v} = {}^{B}_{E}q \otimes {}^{E}\vec{v} \otimes {}^{B}_{E}q^{*} \qquad (4.9) $$

$$ {}^{B}\vec{v} = {}^{E}_{B}q^{*} \otimes {}^{E}\vec{v} \otimes {}^{E}_{B}q \qquad (4.10) $$

The Earth's frame referred to in the measurement from the accelerometer (gravity vector) is assumed to be pointing towards the center of the Earth, while the magnetometer results are expected to be pointing to the North magnetic pole. Both sensing units were used to follow similar approaches to the quaternion correction challenge, as described in the following equations.

Enhancement of the estimated quaternion with gravity vector correction ($\hat{q}_{GA}$):

$$ \hat{q}_{GA} = q_G \otimes \Delta q_A \qquad (4.11) $$

where;

$$ \Delta q_A = \mathrm{H}(\vec{q}_{Av}, q_{Aw}) \qquad (4.12) $$

$$ \vec{q}_{Av} = \vec{a}_0 \times \vec{a}(q_G) \qquad (4.13) $$

and

$$ q_{Aw} = \left|\left|\vec{a}_0\right|\right|\left|\vec{a}(q_G)\right| + \vec{a}_0 \cdot \vec{a}(q_G) \qquad (4.14) $$

$$ \vec{a}(q_G) = q_G^{*} \otimes A_{int} \otimes q_G \qquad (4.15) $$

In these equations $\vec{a}_0$ is the measured gravity vector from the accelerometer, $\vec{a}(q_G)$ is the calculated gravity vector referenced in the sensor's body frame and A_{int} is the initial gravity vector that is assumed to be pointing towards the Earth's center (in the Earth frame).

Enhancement of the estimated quaternion with magnetic north vector correction ($\hat{q}_{GM}$):

$$\hat{q}_{GM} = q_G \otimes \Delta q_M \qquad (4.16)$$

where;
$$\Delta q_M = \mathrm{H}(\vec{q}_{Mv}, q_{Mw}) \qquad (4.17)$$

$$\vec{q}_{Mv} = \vec{m}_0 \times \vec{m}(q_G) \quad (4.18)$$

and
$$q_{Mw} = \left||\vec{m}_0|\right||\vec{m}(q_G)|| + \vec{m}_0 \cdot \vec{m}(q_G) \qquad (4.19)$$

$$\vec{m}(q_G) = q_G^* \otimes M_{int} \otimes q_G \qquad (4.20)$$

In these equations $\vec{m}_0$ is the measured magnetic North vector from the magnetometer, $\vec{m}(q_G)$ is the calculated magnetic North vector referenced in the sensor's body frame and M_{int} is the initial magnetic North vector that is assumed to be pointing to the Earth's North pole (in the Earth frame).

Both $\hat{q}_{GA}$ and $\hat{q}_{GM}$ are required to be normalized before using them as a rotation operator in the next step. As described, the discussion of the limitations of each sensor (Chapter 3), the compensation using $\hat{q}_{GA}$ could be directly and exclusively applied if the sensor module is static or moving without change of speed. Similarly, the $\hat{q}_{GM}$ represents the corrected estimated orientation that uses the measurement from the magnetometer, under the assumption that the Earth's magnetic field is constant in orientation. This assumption may be disrupted in areas where there is significant magnetic field distortion. To define the final estimated orientation, the quaternion

interpolation uses a control parameter, which assigns complementary weights to the contributions of the calculated $\hat{q}_{GA}$ and $\hat{q}_{GM}$.

4.1.1 Spherical Linear Quaternion Interpolation

Spherical Linear Quaternion Interpolation (SLERP) or great arc interpolation is an approach that defines a final orientation estimates given two initial rotation estimates in quaternion from by using a parametric weight. Erik Dam [49] has proved the equivalence of the expressions for SLERP and introduced the SLERP without exponentiation as shown in Equations (4.21) and (4.22).

$$cos(\Omega) = q_0 \cdot q_1 \qquad (4.21)$$

$$SLERP(q_0, q_1, h) = \frac{q_0 sin((1-h)\Omega) + q_1 sin(h\Omega)}{sin(\Omega)} \qquad (4.22)$$

A parameter Ω is obtained from the dot product of the two initial quaternions (q_0 *and* q_1). The control parameter (h) varies between 0 and 1 to specify the interpolated orientation. Figure 4.2 shows a step in the interpolation, where the value of $h \in [0,1]$, makes the resulting orientation, indicated by the endpoint (O), moves from q_0 to q_1.

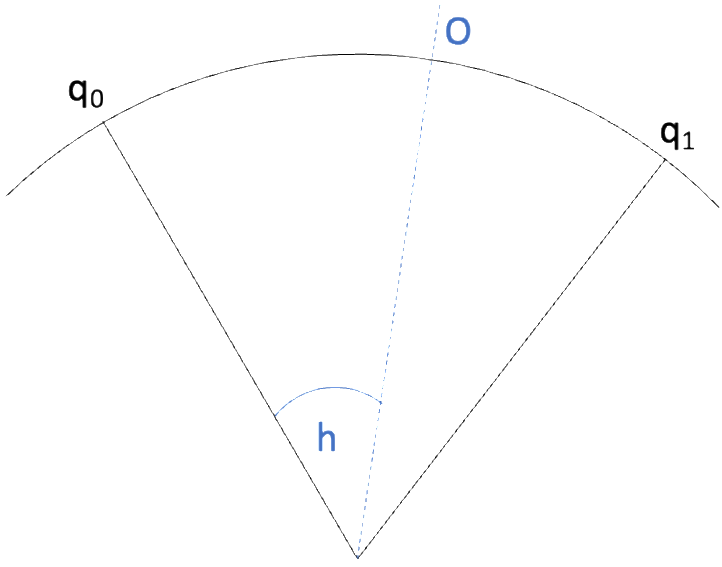

Figure 4.2the output (o) from the interpolation between two quaternions (q_0 and q_1) with the control parameter (h)

This SLERP method yields the optimal interpolation curve between two rotations with the preservation of the magnitude of a unit quaternion on the same great arc.

The original GMV method [50] always defines the final orientation quaternion from SLERP interpolation between $\hat{q}_{GA}$ and $\hat{q}_{GM}$, and it uses only one control parameter for the SLERP operation, which is h = α, the "stillness" parameter, using it as representative of how close the state of the module is static (Alpha is explained further in the following sections). If this parameter, alpha is close to 1, the assumption that is necessary for exact validity of gravity vector correction is essentially being fulfilled and $\hat{q}_{GA}$ is favored over $\hat{q}_{GM}$ in the SLERP interpolation. The magnetic North vector correction contribution plays a "passive" role in the weighting of the 2 contributions and is only allowed to play a significant role in the definition of the final orientation estimate as an "else" condition, when it is known that the gravity vector correction alone will not be fully adequate.

4.2 Gravity-Magnetic Vector Compensation with Double SLERP (GMV-D)

This dissertation proposes a new multisensory orientation estimation algorithm which combines the possible ways of correcting the initial orientation estimation from gyroscope signals, $\hat{q}_G$, in a manner that takes full advantage of all the information available to an orientation and position tracking system. In this new approach, position estimates are utilized in an interactive way to assign a value (in a 0-to-1 scale) to the trustworthiness (m) of a tentative magnetic North vector correction, as a counterpart to the alpha parameter ("stillness"), which quantizes the adequacy of the gravity vector correction.

Moreover, in this new approach, if the merging of both the gravity vector correction and the magnetic North vector correction is appropriate, it will be performed by an algorithm that is controlled by two parameters: α and μ, allowing both contributions to play an "active" role in the weighing of the partial corrections. This new method of merging the partial corrections has been called "Double SLERP"

4.2.1 Double SLERP

Considering the limitations in using both accelerometers and magnetometers for orientation correction, the double application of SLERP was proposed to estimate the final orientation estimate ($\hat{q}_{out}$) in the new algorithm. The double SLERP process uses two control parameters, Stillness (α) and Magnetic Trustworthiness (μ) to define the output (final) orientation, as shown in the Equation (4.23). There are three tentative estimates of orientation available, which are the estimated quaternion ($\hat{q}_G$), the estimated quaternion with gravity vector correction ($\hat{q}_{GA}$), and the estimated quaternion with magnetic North vector correction ($\hat{q}_{GM}$). The consideration of both α and μ yields four possible stages as described in the Table 4.1, which also the correction source that will be given preference in each of the 4 stages.

$$\text{Let's } (q_0 \cdot q_1(h)) = SLERP(q_0, q_1, h) = \frac{q_0 sin((1-h)\Omega) + q_1 sin(h\Omega)}{sin(\Omega)}$$

$$\hat{q}_{out} = \{[\hat{q}_G \cdot \hat{q}_{GM}(\mu)] \cdot [\hat{q}_G \cdot \hat{q}_{GA}(\alpha)](\alpha)\} \qquad (4.23)$$

Table 4.1Four possibilities of the final estimate orientation from the Double SLERP method.

STAGE	CONTROL PARAMETER		The final estimated orientation ($\hat{q}_{out}$) tend to use the compensation from:
	(α) close to:	(μ)close to:	
0	0	0	$\hat{\boldsymbol{q}}_{\boldsymbol{G}}$: correction did not apply
1	1	0	$\hat{\boldsymbol{q}}_{\boldsymbol{GA}}$: correction using gravity vector
2	0	1	$\hat{\boldsymbol{q}}_{\boldsymbol{GM}}$: correction using magnetic North vector
3	1	1	$\hat{\boldsymbol{q}}_{\boldsymbol{GA}}$: correction using gravity vector

4.2.2 The Control Parameters (α and μ)

4.2.2.1 Sensor's Stillness (α)

The stillness of the sensor indicates the confidence that exists to apply the orientation correction with the gravity vector. Section 3.4.2 described the limitations of accelerometers-based correction in different circumstances. Therefore, the control parameter of quaternion interpolation for gravity vector (α) is calculated from the stillness data given out as the Yost Labs 3-Space Sensor's confidence value.

Prior to being used to determine the value of the control parameter for quaternion interpolation by gravity vector (α), the average confidence value (stillness), read from the IMU module, was processed by a first-order Gamma memory filter to smoothen the signal. The Gamma memory filter uses a weight parameter (W_α) that ranges between 0 to 1 to control the filtering characteristics of the lowpass filter it implements on the signal. The first-order Gamma memory filter has the transfer function in z-domain derived in Equations (4.24) – (4.27).

$$H(z) = \frac{Y(z)}{X(z)} = \frac{W}{z-(1-W)} \qquad (4.24)$$

$$Y(z) = (W)z^{-1}X(z) + (1-W)z^{-1}Y(z) \qquad (4.25)$$

$$y[n] = (W)x[n-1] + (1-W)y[n-1] \qquad (4.26)$$

$$\alpha_g = W_\alpha\,(Stillness(n-1)^2) + (1-W_\alpha)\alpha_g(n-1) \qquad (4.27)$$

By experimentation with the IMU module, a weight parameter (W_α) value of 0.25 was found to be adequate to smooth the signal, while avoiding the introduction of a large amount of delay. Once the stillness signal is smoothened, a linear equation was applied to accelerate the drop of the α value when the sensor begins departing a static status,

driving the value of the stillness parameter down. This equation is characterized by the value of its slope (m_α). The higher the value of this slope, the quicker the graph will drop below 1, as shown in Figure 4.3. The final value of the control parameter for quaternion interpolation of gravity vector correction (α) is calculated from Equations 4.28 and 4.29.

$$\alpha = m_a \alpha_g + (1 - m_a) \qquad (4.28)$$

$$\alpha = \alpha + \frac{|\alpha|}{2} \qquad (4.29)$$

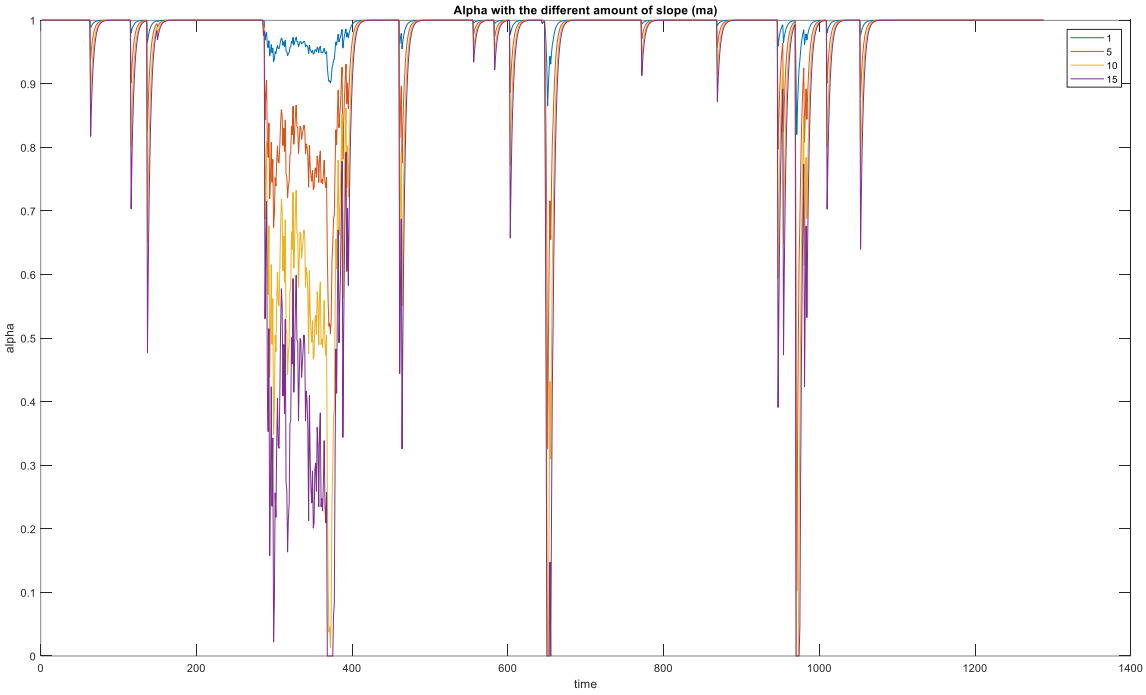

Figure 4.3Calculated alpha with Four different slopes (m_α), smallest no. of slope = Blue, Largest no. of slope = Violet.

4.2.2.2 Magnetic Correction Trustworthiness (μ)

From the studies described in Section 3.4.3, the distortion of the magnetic field is usually only significant in the areas around items that contain soft iron. Therefore, it is possible to interactively develop a position-dependent assessment of how significant the magnetic distortion within the overall environment in which is the IMU module is to be used. It was decided to design this position-dependent parameter to take on values

between μ=1 (which will indicate negligible distortion) to α = 0 (which will indicate very strong distortion of the magnetic North vector's direction). To define this Magnetic Correction Trustworthiness parameter (μ) data from both the IR cameras included in the system setup and the MARG sensors are utilized. The cameras locate the position in the working area to map the amount of magnetic distortion locally present, which is calculated using a comparison between data from the magnetometer and the accelerometer in the MARG sensor. The Magnetic Correction Trustworthiness was initialized as 'zero' for the complete working space. The calculation of a new μ value for reassignment to a specific position started only when the MARG sensors adopt a static state at that position. The estimated quaternion successfully corrected using the gravity vector correction ($\hat{q}_{GA}$) is now stored in a temporary variable called "$\hat{q}_{Gpost}$". The concept of mapping a three-dimensional vector between two different frames was applied, as previously described in Equation 4.10. Therefore, the initial (and supposedly also current) position of the magnetic North vector is mapped to the corrected orientation of the module's body frame using ($\hat{q}_{Gpost}$), as shown in Equation 4.30, as $\vec{\mu}(q_{Gpost})$. Next, the cosine of the angle, γ, between the mapped North magnetic vector and the components of the North magnetic vector sensed by the magnetometer in the IMU ($\vec{m}_0$), is determined, as shown in Equation 4.31. The angle γ represents the angle between the current magnetic North vector and the corrected quaternion. If this angle were 0, it would mean that the corrected estimation by means of the gravity vector and the correction by means of the magnetic North vector coincide exactly. As this whole process is undertaken only when the stillness parameter indicates that the gravity vector correction is highly justified. This would, in turn, imply that the magnetic North vector correction, at this particular position, is fully trustworthy. Larger

values of g would indicate that larger levels of distortions in the Earth's magnetic field can be suspected at the position being considered. The magnetic correction trustworthiness parameter (μ) is calculated in Equations 4.32 and 4.33 to capture in a single number the level of adequacy of a prospective magnetic correction on the basis of g. Table 4.2 illustrates the relation of angle g and the value of Magnetic Correction Trustworthiness (μ). A linear Equation with the negative slope (m_m) is also applied to accelerate the change of the μ parameter, as the sensor is placed at locations where the distortion of the Earth's magnetic fields is more and more intense. The higher of the value of the slope (m_m), the quicker the resulting μ value will be driven down, as exemplified in Figure 4.4.

$$\vec{\mu}(q_{Gpost}) = q^{*}_{Gpost} \otimes M_{int} \otimes q_{Gpost} \qquad (4.30)$$

$$cos(\gamma) = \frac{\vec{m}_0 \vec{\mu}(q_{Gpost})}{|\vec{m}_0||\vec{\mu}(q_{Gpost})|} \qquad (4.31)$$

$$\mu_{temp} = -m_m(acos(cos(\gamma))) + 1 \qquad (4.32)$$

$$\mu = \frac{(1+\mu_{temp})}{2} \qquad (4.33)$$

Table 4.2Relations between the current magnetic North vector ($\vec{m}_0$) and the corrected quaternion, $\vec{\mu}(q_{Gpost})$, given the Magnetic Correction Trustworthiness (μ) value.

Vectors	θ	$\cos(\gamma)$	μ
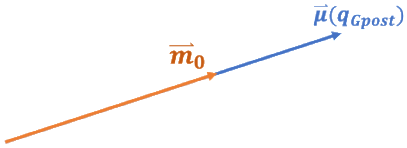	~ 0º	1	1
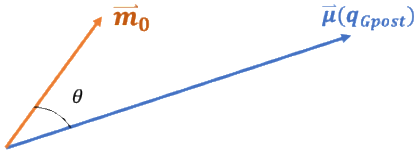	0º < θ < 90º	0 < $\cos(\gamma)$ < 1	0.5 < μ < 1

	θ = 90º	0	0.5
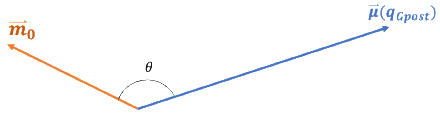	90º < θ < 180º	-1 < cos(γ) < 0	0 < μ < 0.5
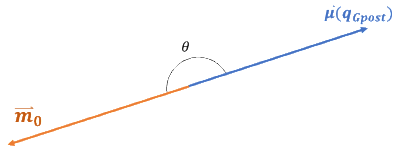	θ = 180º	-1	0

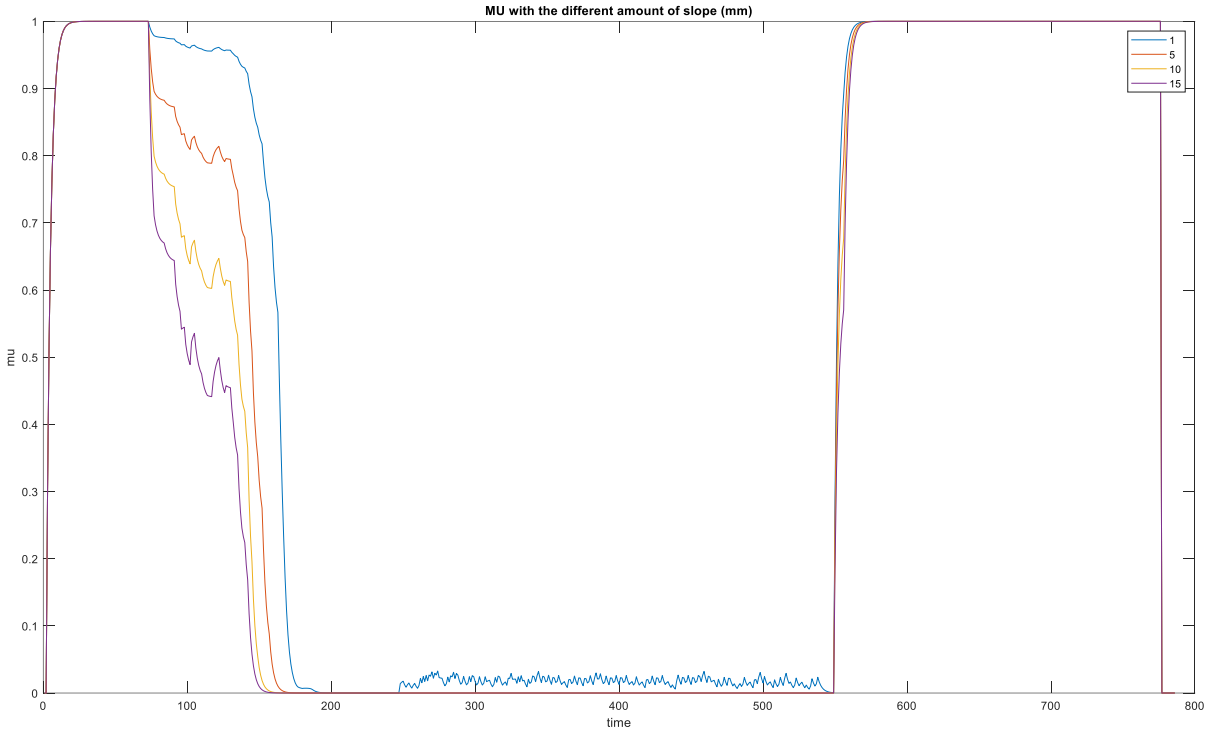

Figure 4.4Calculated MU with Four different slopes (m_m), smallest no. of slope = Blue, Largest no. of slope = Violet.

4.2.2.3 Studies of the relationship between settings for both parameters

The previous sessions described the definition and impact of each of the two control parameters for the double SLERP function. Linear equations were involved in both calculations to accelerate the decrease of the parameter values when the limitations

for each of the two sensors becomes increasingly significant. Small variations in the values of the slopes of those linear functions affects the overall output of the algorithm. This section shows the study of the behavior of the algorithm, as these two slopes, m_α and m_m, are varied in the processing of recordings that include four possible scenarios for the sensor module: rotation in an area without magnetic distortion, rotation in an area with magnetic distortion, translation in an area without magnetic distortion, and translation in an area with magnetic distortion. The experiment investigated three levels for both slopes: low (m_a, m_m = 1), mid (m_a, m_m = 5), and high (m_a, m_m = 10), yielding nine cases for each scenario, as shown in Figure 4.5(a-d). The green boxes indicate the settings that shows acceptable outputs of the Double SLERP algorithm for each case.

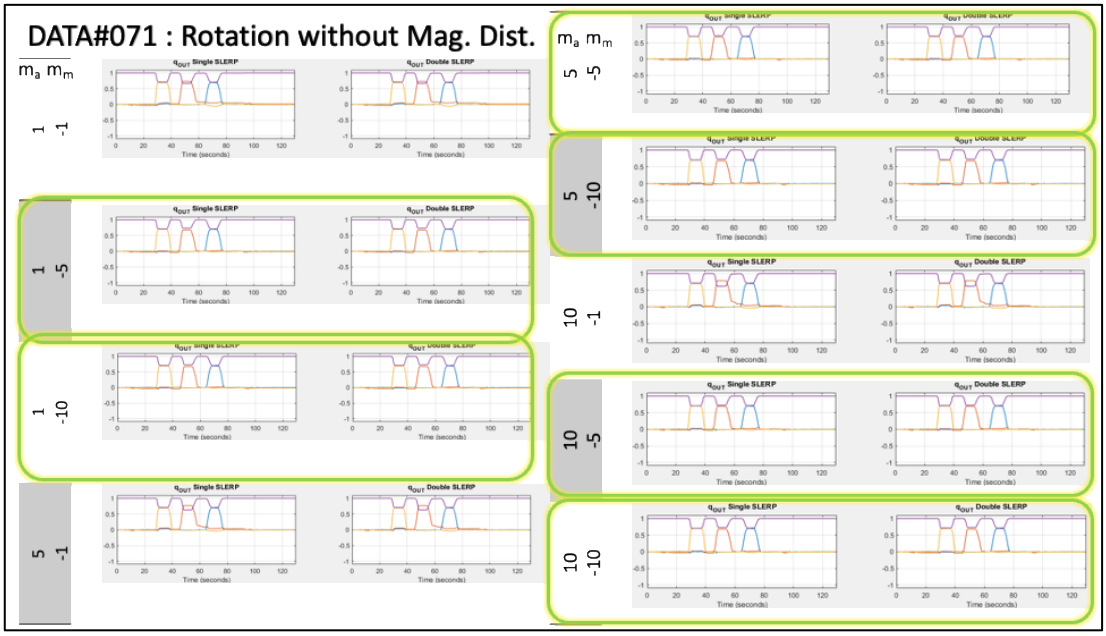

(a)

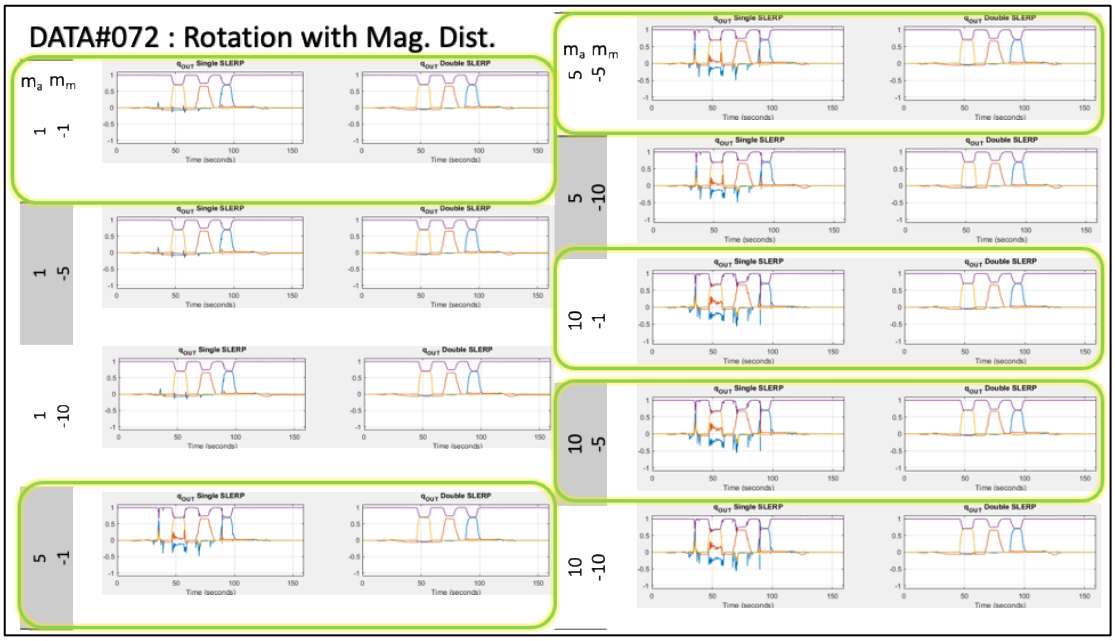
DATA#072 : Rotation with Mag. Dist.
m_a m_m
1 -1
1 -5
1 -10
5 -1
5 -5
5 -10
10 -1
10 -5
10 -10
q_{OUT} Single SLERP
q_{OUT} Double SLERP
Time (seconds)

(b)


DATA#077 : Translation without Mag. Dist.
m_a m_m
1 -1
1 -5
1 -10
5 -1
5 -5
5 -10
10 -1
10 -5
10 -10
q_{OUT} Single SLERP
q_{OUT} Double SLERP
Time (seconds)

(c)

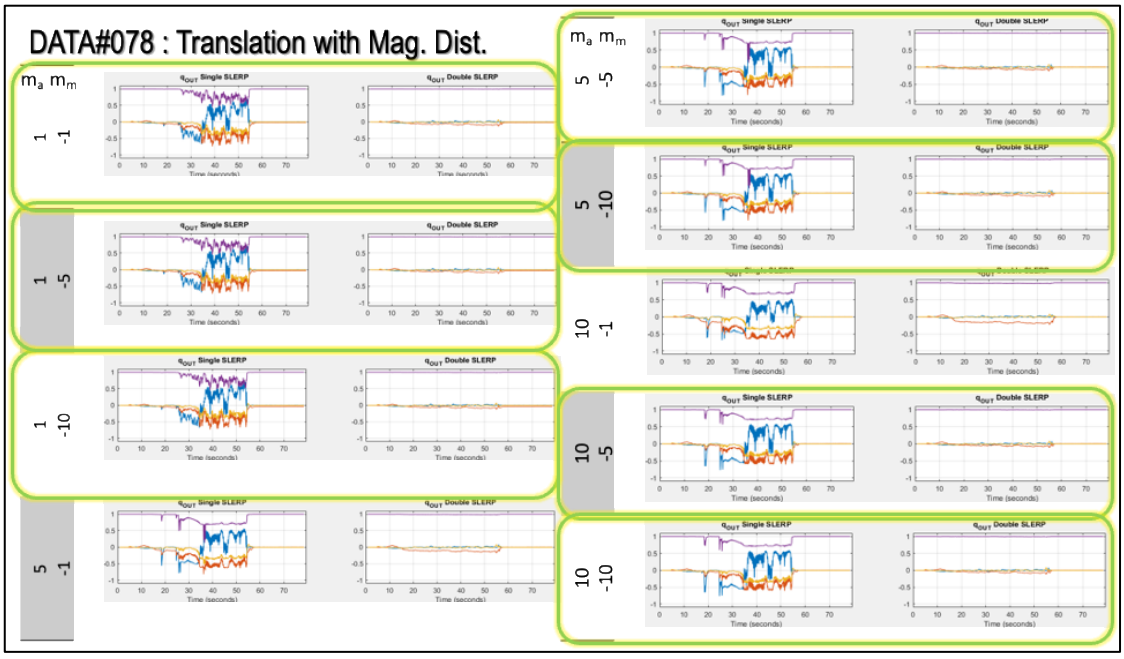

(d)

Figure 4.5The output of Single SLERP vs Double SLERP with varying Slope ma and mm at 4 Scenarios (a)Rotation without Magnetic Distortion, (b) Rotation with Magnetic Distortion, (c)Translation without Magnetic Distortion, and (d) Translation with Magnetic Distortion.

By analyzing all possible outcomes with different slope settings, the slope for alpha (m_a) was set as 1, while the slope for mu (m_m) was varied between 1 and 5. Therefore, another experiment was held to test with a fine-tuning value of slope (m_m) running from 1 to 5 with 1 as increment. The set of slope values for both α and μ were then set finally as m_a =1 and m_m =2, which yields adequate results in all four scenarios.

4.2.2.4 Voxel partition of the working space

Section 4.2.2.3 mentioned that the IR cameras were used to verify the MARG sensors' location that mapped within the working space of the system, for storing the value of the calculated μ parameter. However, attempting to deal with the position coordinates as continuous variables in this process is unnecessary and would slow the performance of the algorithm. Instead, the level of magnetic distortion in different regions of the working space for the system can be evaluated in small discrete sub-regions. These sections outline a method to divide the working space into a 3-

dimensional array of sub-regions, which creates an appropriate dreamwork, easily mapped to an adequate data structure where the position-dependent values of μ can be stored.

Firstly, the units of the position coordinates output by the camera system must be defined and converted into the units used to map the working space. This research has used the metric system units to split the working space into a cubic grid (unit=cm). Each box in the cubic grid is called a "voxel," which has a specific size in each of its 3 dimensions (width, height, depth); a smaller size would allow a higher resolution mapping, which is desirable. However, the trade-off between resolution and processing time must be taken into account. This research has set the voxel size to be 1 cm. Equation 4.34 shows how a voxel index is assigned from the current coordinate of the marker identified by the camera system, in any of the 3 spatial directions. For example, if the marker position is indicated by a coordinates value between 0 to 1 cm, the marker is now located at Voxel #1 (in that particular dimension), and a coordinate value running between 1 to 2 cm will yield a Voxel index of 2.

$$Location\ of\ marker\ (index)\ =\ floor(\frac{Current\ Coordinate}{Voxel\ Size}\ )\ +1 \qquad (4.34)$$

All voxels in cubic area initialize with μ = zero. The system will gradually store actual values of μ in each voxel only when that specific region of the working space is visited by the system and if the accelerometer-corrections were found to be valid (the sensor is static). In time, more and more voxels will be assigned measured non-zero μ values, and a considerable proportion of magnetometer-corrections will also be enabled, shown in Figure 4.6. Numerically, the system keeps the μ values as a 3-D array, $\mu(x, y, z)$, for all the voxels in the space where the sensor will operate.

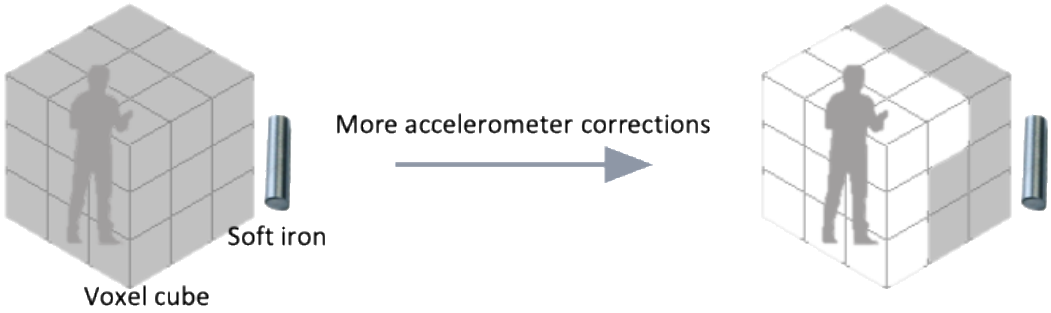

Figure 4.6The cubic grid with voxels in the working space. Black voxels indicate μ = zero. White voxels indicate non-zero μ with no magnetic distortion.

CHAPTER 5 – SETUP AND IMPLEMENTATION OF THE HAND MOTION TRACKING SYSTEM

In this chapter, the hand motion tracking system was described. Two devices were used to set up the system: the infrared cameras and Magnetic, Angular-rate, Gravity (MARG) module. The infrared cameras purposely determined the position of the hand in three-dimensional space while the MARG was used to detect the hand orientation. The Cartesian coordinates of an infrared-reflective marker attached to the holding box were obtained from the infrared cameras. The orientation of the hand is captured from the MARG units attached to the holding box. MARG module consists of three types of sensors: gyroscope, accelerometer, and magnetometer, giving the tri-axial data. The hand motion tracking system with the proposed algorithm uses the combined data from both infrared cameras and the MARG module. We choose two specific devices in this research: for tracking position using OptiTrack V120: Trio infrared cameras, and for orientation measurement using Yost Labs 3-Space sensors.

5.1 Equipment

5.1.1 Used of OptiTrack V120: Trio for Position Tracking

The infrared camera model V120: Trio was picked from OptiTrack company. Three infrared sensing units are horizontally aligned in a single bar with the size of 23”

W x 1.6” H x 2” D, shown in Figure 5.1, which allows for tracking up to 6 degrees of freedom objects. Each image sensor has an image resolution of 640x480 with 120 FPS frame rate surrounded by 26 adjustable brightness infrared LEDs. The OptiTrack V120: Trio operates using only two ports: the power supply of 12 VDC 3A through the given adapter and data transfer via USB 2.0 port. The fixed distances of the three cameras are self-contained and pre-calibrated by the manufacturer, and ready to use. Camera lenses contain the field of view of 47 degrees horizontally and 43 degrees vertically with a 3.5mm focal length, giving the visible operation distance of 2 to 17 feet away from the device. The operation volume size of the OptiTrack V120:Trio is displayed in Figure 5.2.

Figure 5.1The infrared camera model V120: Trio. From Optrictrack, NaturalPoint, Inc., March 2021 [69].

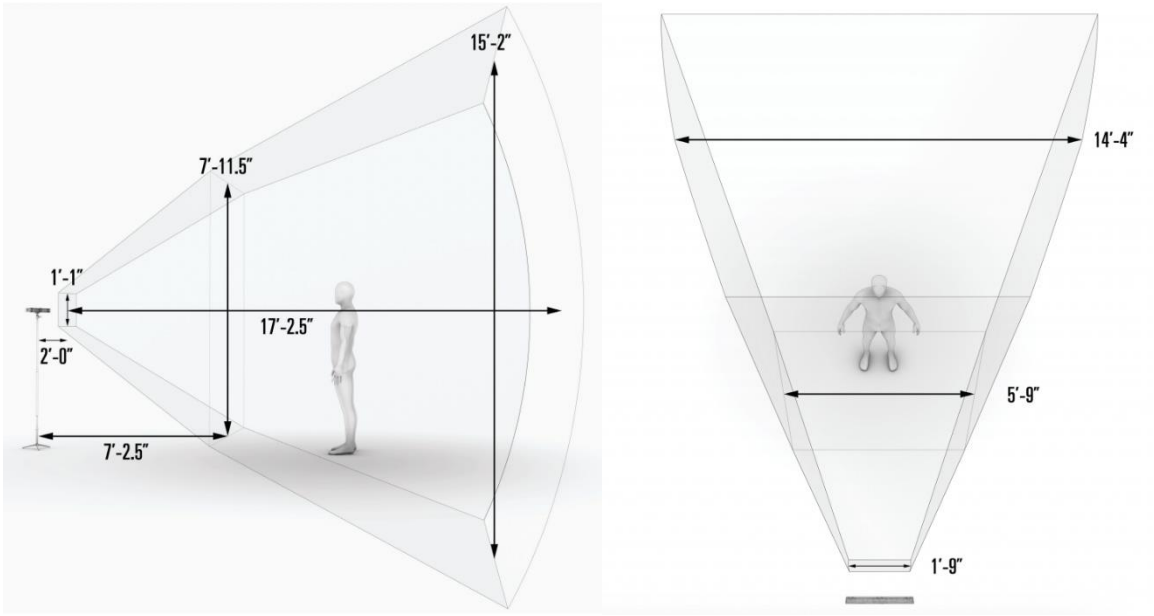

Figure 5.2The operation volume size of the OptiTrack V120: Trio from side view (left) and top view (right). [70]

OptiTrack provides an engineering-grade software called “Motive: Tracker.” This software modifies the camera setting such as broadcasting channel, assign markers or rigid body, adjust the exposure of LEDs, etc. Adjusting the exposure value in the motive setting helps eliminate an unwanted reflection that appears on the image. OptiTrack also developed a plug-in that allows us to link the position of designated markers obtained from the cameras with a virtual 3D object in Unity. The Motive application establishes the local connection to a NatNet server and streams the tracking coordinate data using the NatNet protocol.

Three IR-reflective dot markers are attached at each side of the holding box, shown in Figure 5.3. One dot marker is visible to the infrared cameras and appears as a single point in the three-dimensional space, representing the sensor module's position. The LEDs from cameras emit infrared light to reflect with the marker and capture the dot marker using the image-sensing units. Then, the Motive Tracker computes three-dimensional Cartesian coordinate (x, y, and z) in real-time as the position of the dot marker. The coordinates x, y, and z will be used to represent the position of the holding

box in a 3D environment and used to calculate the location of the Voxels to determine the magnetic distortion area.

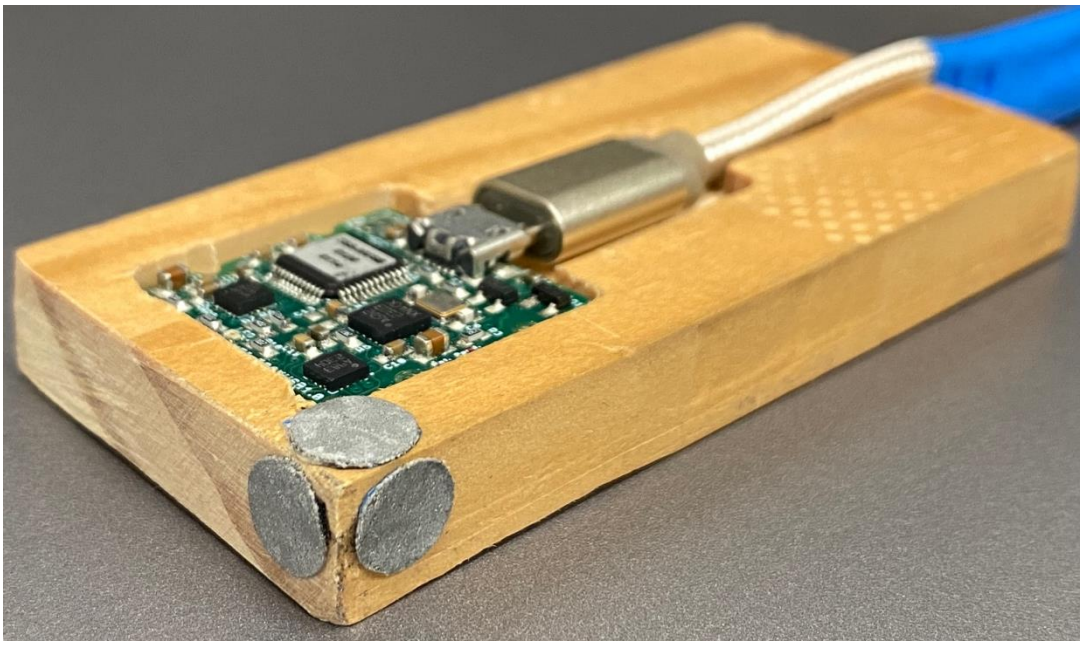

Figure 5.3A wooden box with Infrared-reflective markers.

5.1.2 Used of Yost Lab 3-Space Sensors for Orientation Tracking

The commercial-grade MEMS IMUs from the Yost Lab 3-space sensor are chosen for detecting the orientation, shown in Figure 5.4. These MEMS IMUs consist of a gyroscope, accelerometer, and magnetometer, capable of measuring the body's rotational motion, body's, and Earth's magnetic field in three-dimensional space, respectively. The Yost Lab 3-space^{TM} sensor Micro USB model is an ultra-miniature, low-cost inertial measurement unit with high precision and high reliability. The sensor costs $65 per unit with 23mm x 23mm x 2.2 mm in size and weight only 1.3 grams. The sensor is installed inside the holding box to capture the movement. The Yost Lab 3-space^{TM} sensor consumes power of 45mA at 5V and transfers data using a single port of mini USB2.0 (Asynchronous Serial) connection. The sensor model provides several data types, such as Quaternion, Euler angles, Axis angle rotation matrix, and the

processed data such as normalized sensor data and calibrated sensor data. The specification of Yost Lab 3-space^{TM} sensor Micro USB is shown in Table 5.1.

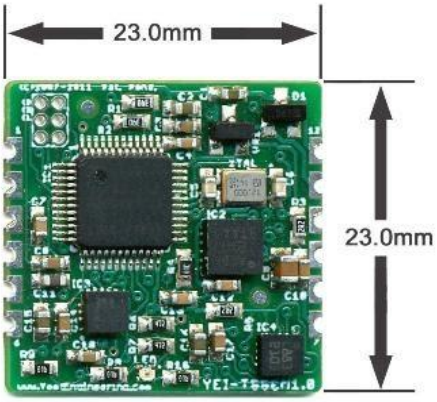

Figure 5.4Yost Lab 3-spaceTM sensor Micro USB with dimension

Yost labs provided software called “3-space Software Suite” to calibrate the sensor before implementing the proposed algorithm. The sensor is connected to the host PC using a micro-USB to type-A USB cable. To activate the sensor port and obtain the data, specific ASCII characters' commands [41] have to be sent to the sensor.

The C# script was written in Unity to receive the streamed measurement data via the communication ports, which are the timestamp (4 bytes), sensor’s confidence value (4 bytes), accelerometer data (12 bytes, 4 bytes for each x, y and z axes), angular velocity (12 bytes), and magnetometer data (12 bytes). The rotational movement is obtained from the parsed data of angular velocity streaming and compensate by the proposed correction algorithm using the streaming data from the accelerometer and the magnetometer. The overall algorithm was implemented using within the C# script in Unity.

Table 5.1Specifications of Yost Lab 3-spaceTM sensor Micro USB [71]

Specifications	Value
Orientation range	360º about all axes
Orientation accuracy	±1º for dynamic conditions & all orientations
Orientation resolution	<0.08º
Orientation repeatability	0.085º for all orientations
Accelerometer scale	±2g / ±4g / ±8g selectable for standard models ±6g / ±12g / ±24g selectable for HH models ±100g / ±200g / ±400g selectable for H3 models
Accelerometer resolution	14 bit, 12 bit(HH), 12 bit(H3)
Accelerometer noise density	99µg/√Hz, 650µg/√Hz(HH), 15mg/√Hz(H3)
Accelerometer sensitivity	0.00024g/digit-0.00096g/digit 0.003g/digit-0.012/digit(HH) 0.049g/digit-0.195g/digit(H3)
Accelerometer temperature sensitivity	±0.008%/°C, ±0.01%/°C(HH, H3)
Gyro scale	±250/±500/±1000/±2000 º/sec selectable
Gyro resolution	16 bit
Gyro noise density	0.009º/sec/√Hz
Gyro bias stability @ 25°C	2.5º/hr average for all axes
Gyro sensitivity	0.00833º/sec/digit for ±250º/sec 0.06667º/sec/digit for ±2000º/sec
Gyro non-linearity	0.2% full-scale
Gyro temperature sensitivity	±0.03%/°C
Compass scale	±0.88 Ga to ±8.1 Ga selectable (±1.3 Ga default)
Compass resolution	12 bit
Compass sensitivity	0.73 mGa/digit
Compass non-linearity	0.1% full-scale

5.1.3 Wooden box to hold the sensor.

A non-ferromagnetic (wooden) box was created to restrain the Yost Lab 3-space^{TM} sensor. The box has the 8cm x 4cm x 1cm in sizes attached with the holding stick at one end, shown in Figure 5.5. Each side of the box is perpendicular, which allows the position to be trusted with a 90-degree rotation reference. The flat surface of the box is controlled with a level surface with a genuinely horizontal position. Using the restrained sensor box helps to eliminate the error created from the hand. Hand has

offset gaps between the HAND to glove and fabric glove to the sensor, as illustrated in Figure 5.6. The box keeps the consistency from each subject (size of the hand is not affect) and reduces and controls the error that might occur. Therefore, the output from the experiment represents the true difference of e ach algorithm only.

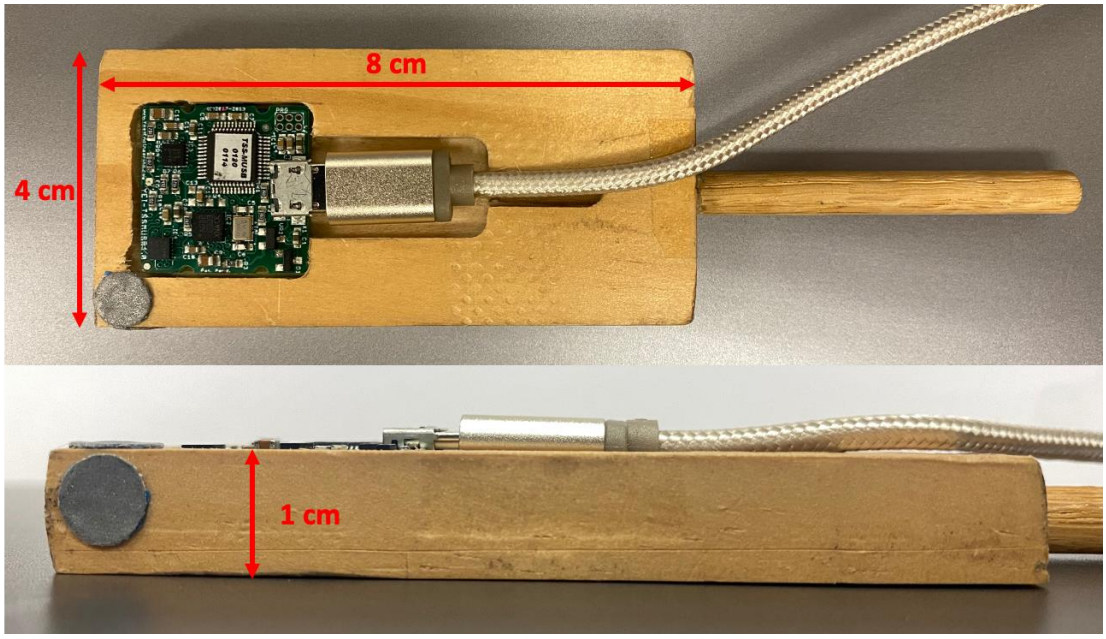

Figure 5.5The non-ferromagnetic box with Yost Lab 3-spaceTM sensor attached.

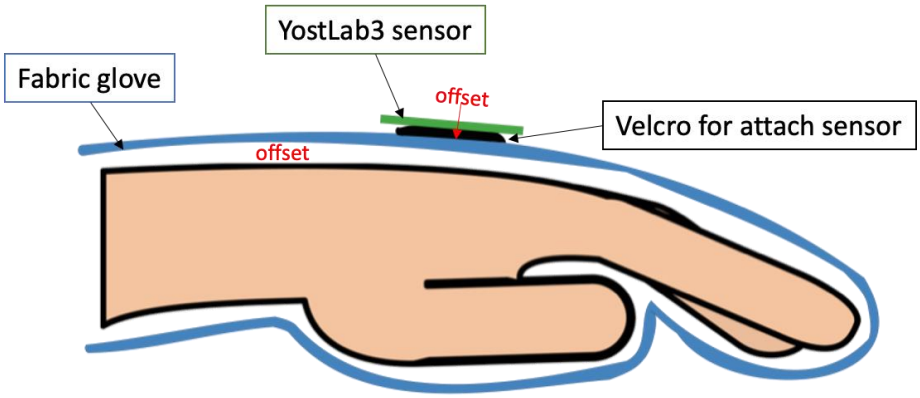

Figure 5.6The illustration of the hand inside the fabric glove with the sensor attached.

5.2 Implementation

In order to evaluate the performance of the motion tracking system, based on the MARG sensor, an experiment with the human subjects was conducted (the experiment received FIU Internal Review Board authorization #IRB-19-0110). Thirty

human subjects were asked to participate in the experiment. Each of the subjects came to the testing area and performed the movement tasks. During the performance, the grasped box's location was recorded using the marker coordinate from OptiTrack V120: Trio, and the oriented angle data from a Magnetic, Angular-rate, Gravity (MARG) embodied in the grasped box was recorded. The proposed algorithm was implemented to calculate the estimated orientation. The calculated results obtained from the Gravity Vector and Magnetometer with Double SLERP (GMV-D) are compared with the orientation estimates obtained from the Gravity Vector and Magnetometer with Single SLERP (GMV-S), Fixed Bias offset, and the Kalman-based filter quaternion output that provided directly from the Yost Labs 3-Space sensor module.

5.2.1 Hardware and Environment setup

Experiment space was set up with a wooden frame with the confirmation of non-ferromagnetic involved as a non-magnetic distortion area. On the opposite side, a piece of metal is placed on the high stool on the same level as the non-magnetic distortion area to imitate a magnetic distortion area. There is a docking position where the sensor box rest before and after the trials are done. The docking position controlled the initial data that will be used in the algorithm. The OptiTrack V120: Trio camera was placed in front of the mock-up area with a PC with a monitor next to it. Participants will follow animated on-screen instructions created by Unity software. The testing area is shown in Figure 5.7. The Figure 5.8 mapped between the real position of with/without magnetic distorted area and the voxel of MU plot in 3D axis, where blue indicated the MU ≥ Threshold value (0.9) and red represented MU < 0.9.

Figure 5.7The subject performs the experiment at the testing area.

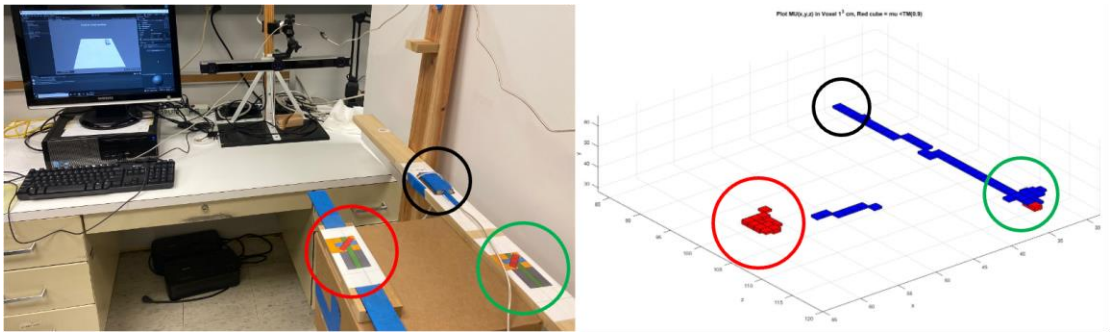

Figure 5.8The experiment station compares with MU plot in 3D cube voxel. Red cube indicated the magnetic distortion (MU<0.9)

5.2.2 Software setting

The quaternion-based correction using the gravity vector and magnetic North vector was created as depicted in the block diagram shown in Figure 5.9. The Gravity Magnetic Vector using double SLERP (GMV-D) C# script was created to implement the orientation correction, operate along with the unity plugin package from Optitrack to determine the position of the sensor. A flowchart showing the algorithm is displayed in Figure 5.10. A virtual 3D environment was also created in the same project with

Unity. A 3D rectangle shape was created and indicated the wooden sensor box. The C# script was written to pre-defined the movements of the sensor box, which consists of an initial position at the dock area, nine sequences at the non-magnetic distorted area, nine sequences at the magnetic distorted area, and the ending position at the dock area. The 3D box model was visualized as the movement guide for the subjects to follow and perform the experiment. Nine sequences at both non-magnetic distorted area and magnetic distorted area are identical, as shown in Figure 5.11.

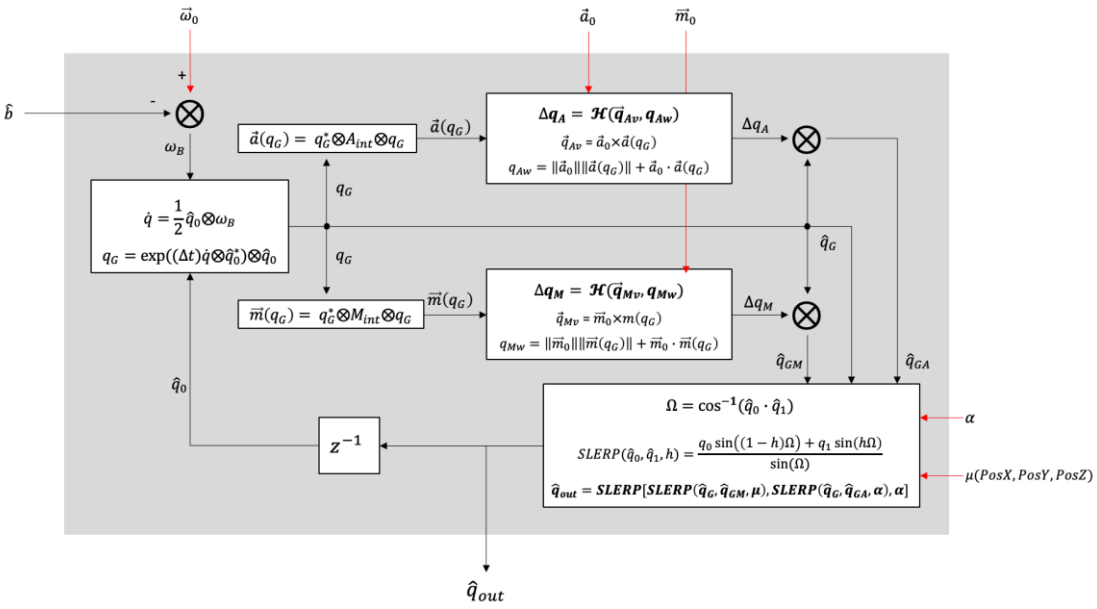

Figure 5.9Block diagram of the orientation correction algorithm using the gravity vector and magnetic North vector with Double SLERP.

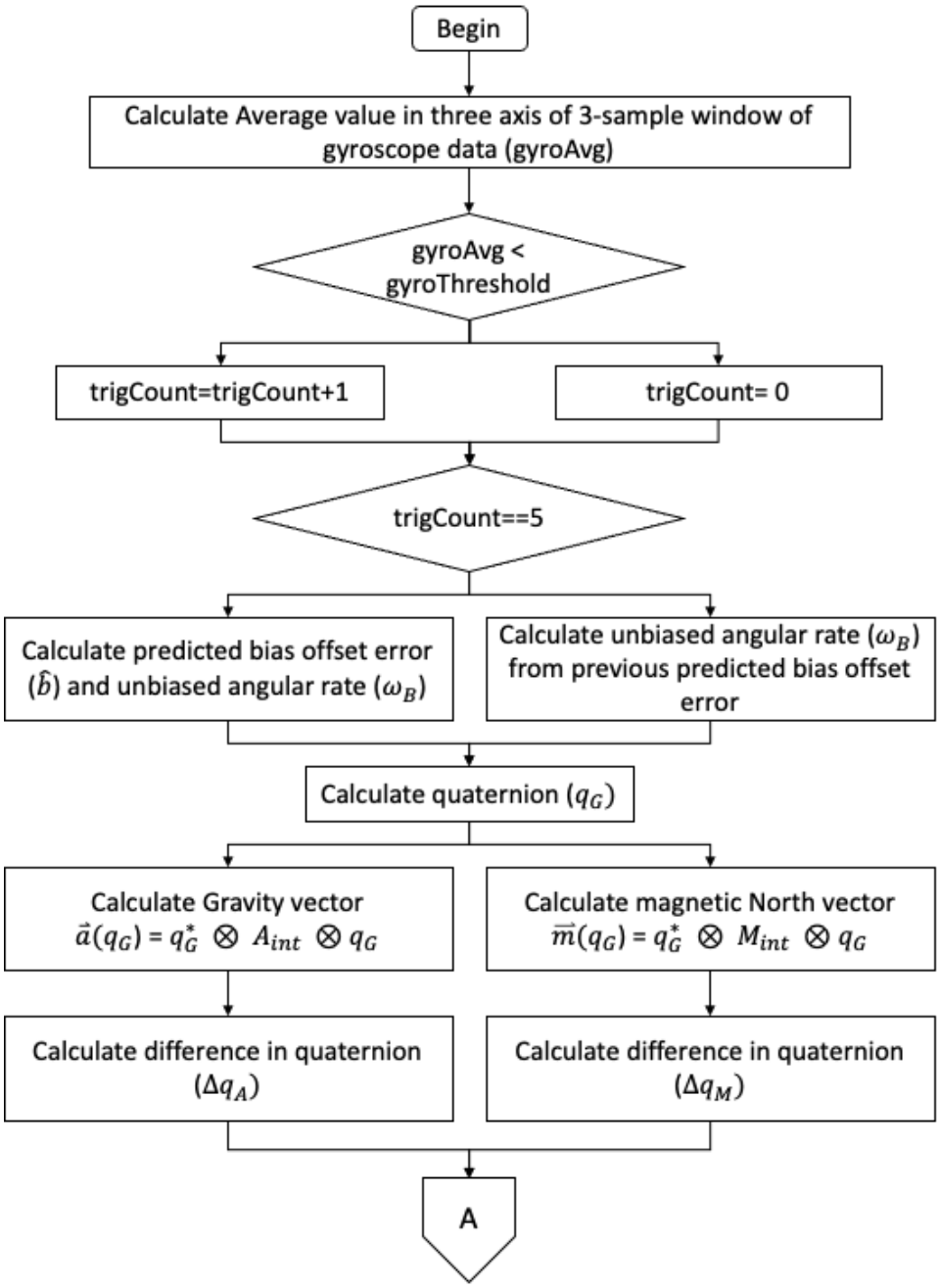
Begin
Calculate Average value in three axis of 3-sample window of gyroscope data (gyroAvg)
gyroAvg < gyroThreshold
trigCount=trigCount+1
trigCount= 0
trigCount==5
Calculate predicted bias offset error ($\hat{b}$) and unbiased angular rate (ω_B)
Calculate unbiased angular rate (ω_B) from previous predicted bias offset error
Calculate quaternion (q_G)
Calculate Gravity vector $\vec{a}(q_G) = q_G^* \otimes A_{int} \otimes q_G$
Calculate magnetic North vector $\vec{m}(q_G) = q_G^* \otimes M_{int} \otimes q_G$
Calculate difference in quaternion (Δq_A)
Calculate difference in quaternion (Δq_M)
A

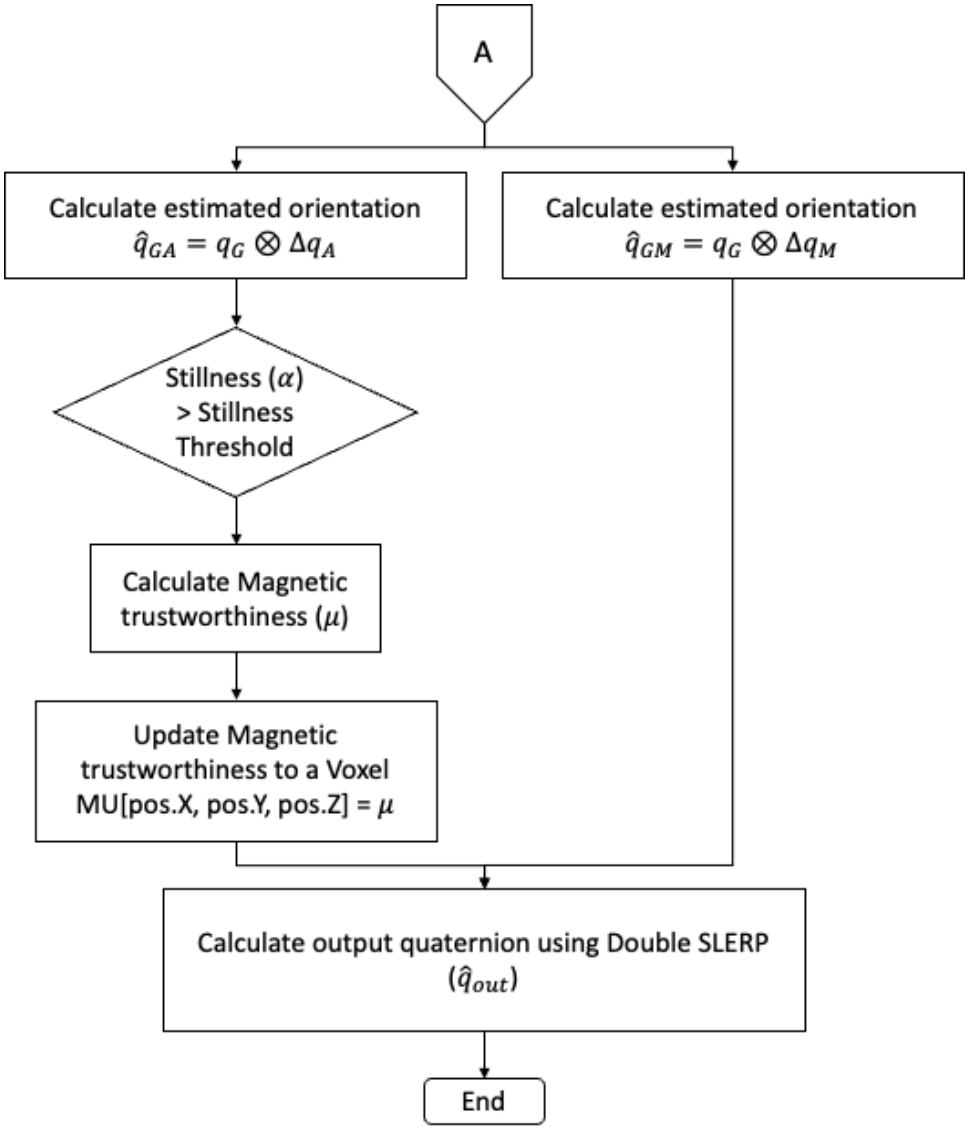

Figure 5.10Flowchart showing the implementation of Gravity Magnetic Vector using Double SLERP corrections algorithm for one iteration, where pos.X, pos.Y and pos.Z obtained from OptiTrack's Unity Plugin.

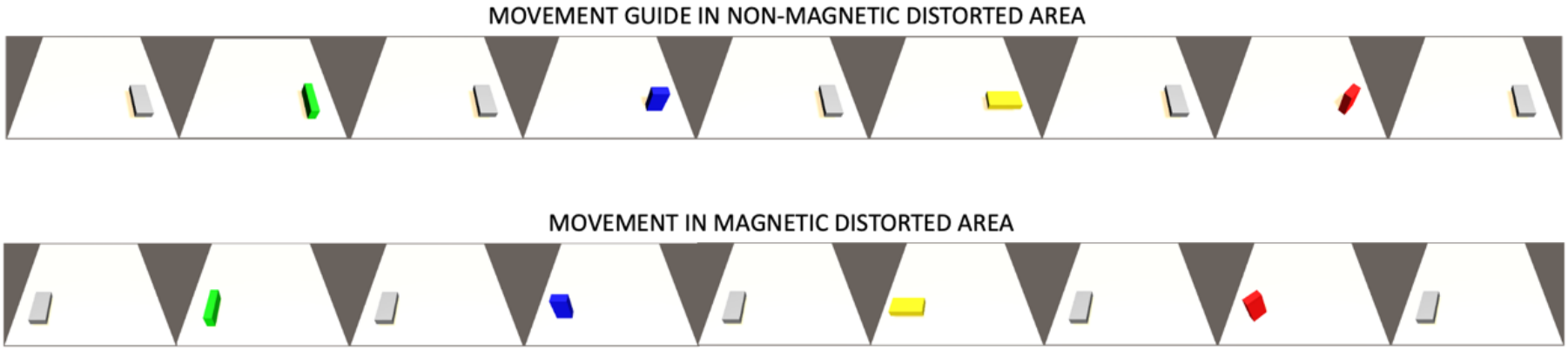

Figure 5.11The movement guide animation in Non-magnetic distorted and Magnetic distorted area showing identical rotation.

5.2.3 Experiment Procedure (from the instruction to the subject approved by FIU IRB)

1. Firstly, the subject was asked to stand in the testing area, which facing toward the IR camera and a desktop monitor with the box of a sensor placed in front of his/her. Then, the experimenter started the program.
2. The experimenter clicked on the button “Mark this position and orientation” to record the initial position and orientation of the sensor.
3. The experimenter clicked on the button “Show next movement” to show the animation of the 3D box model. The 3D box model rotated or translated to the next state (pose) of the box movement sequence.
4. The subject grasped the box and moved to match the position and orientation as shown by the movement guide on the screen.
5. The experimenter clicked on the button “Mark this position and orientation” to record the current position and orientation of the held box.
6. Steps 3 to 5 were repeated to complete 20 states or poses of the movement of the 3D box model had been performed by the subject.
7. The subject was asked to repeat the experiment two times. Then, the subject was asked to answer the simple questionnaire about age, gender, and his/her dominant hand.

Before the experiment began, all participants were asked to read and signed the agreement of the consent to participate in a research study form. This protocol received approval number “IRB-19-0110” on March 29, 2019, from the FIU Internal Review Board.

CHAPTER 6 - EXPERIMENTAL RESULTS

In this chapter, the experiment results are analyzed and described in two ways. Firstly, four types of methods are compared in Time domain present in four component of quaternion graph and illustrate with 3D hand model. Statistical evaluation is explained in the second section where the Fixed Bias method was disregarded due to the obvious poor result showed in Section 6.1.

6.1 Comparison of quaternion components

To verify the result of the proposed GMV-D algorithm, the corrected orientation was expressed as a quaternion ($\hat{q}_{out}$ in Figure 5.9) for the GMV-D method and compared with three other methods (Fixed Bias, Kalman Filtering, and GMV-S). Three of the numbers contained in a quaternion (in our case, $\hat{q}_x$, $\hat{q}_y$and $\hat{q}_z$) represent an axis vector in 3-dimensional space, and the 4th component ($\hat{q}_w$in our case), indicates the amount of rotation to be performed [6]. Therefore, we display the 4 components of the output orientation quaternion through time in order to analyze the results (Figure 6.1). The panels in Figure 6.1 show the evolution of the 4 quaternion components from the 4 methods for the complete duration of the experiment (The horizontal axes are labeled in samples, where the sampling interval was 10ms). The first half of the record (left of the vertical green dividing line) corresponds to the rotations that took place in the area that was not magnetically distorted. The second part of the record (to the right of the green line) represents the same sequence of rotations, now performed in the magnetically distorted area. The 4 quaternion components in the top panel ("Fixed Bias") display drift that grows gradually throughout the experiment, with and without magnetic distortion. All other methods ("Kalman Filter", "GMV-S", and "GMV-D") performed very similarly when magnetic distortion was not present. However, both the

Kalman Filter and GMV-S show erroneous results in the magnetically distorted area. The bottom panel of Figure 6.1 shows the corresponding output quaternion components obtained from the newly proposed GMV-D algorithm, which displays performance that was much less deteriorated when the rotations took place in the magnetically distorted area.

6.2 Orientation Visualizations

The black numerals in Figure 6.1 (1 to 10) help identified short segments during the experiment when the subject was instructed to sustain specific hand orientations or "poses". The corresponding instructed poses are visualized in 3-D, in Figure 6.3 and Figure 6.3, under "Sequence Reference" (leftmost column). In each pose, the 4 visualizations that are shown to the right of the instructed pose are defined (in Unity) by the quaternion results obtained from "Fixed Bias", "Kalman Filter", "GMV-S", and "GMV-D", from the left to right, respectively. This additional form of visualization shows that the orientations obtained from GMV-D were much closer to the orientations that the subject was instructed to temporarily maintain, particularly when the rotations took place in the magnetically distorted zone (Poses 6 through 10). Figure 6.1, Figure 6.3 and Figure 6.3 confirm that the added processing integrated with GMV-D has made it more resilient to the potential distortion of the magnetic field that may exist some in regions of the working space for the MARG module.

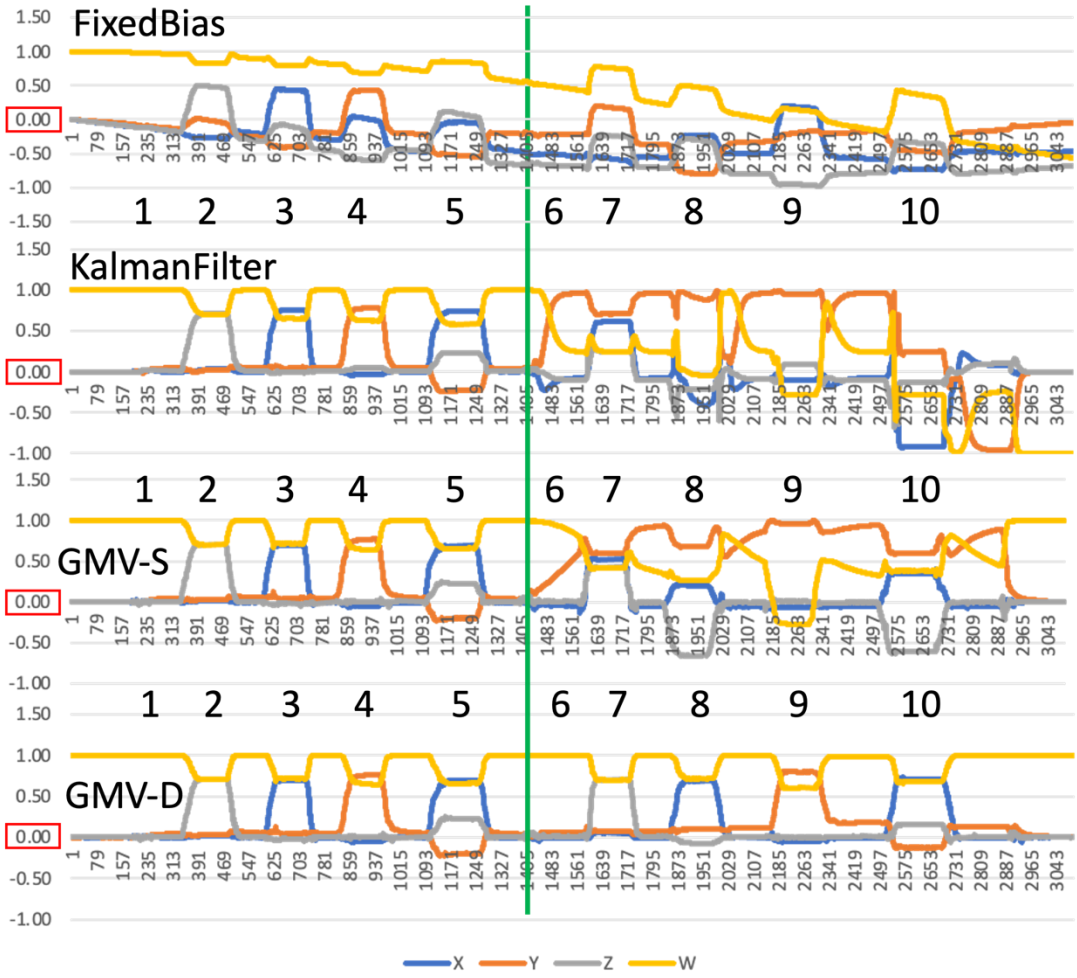

Figure 6.1The evolution of the 4 quaternion components from 4 orientation estimation methods for a complete duration of experiment with interval sampling rate = 10ms.

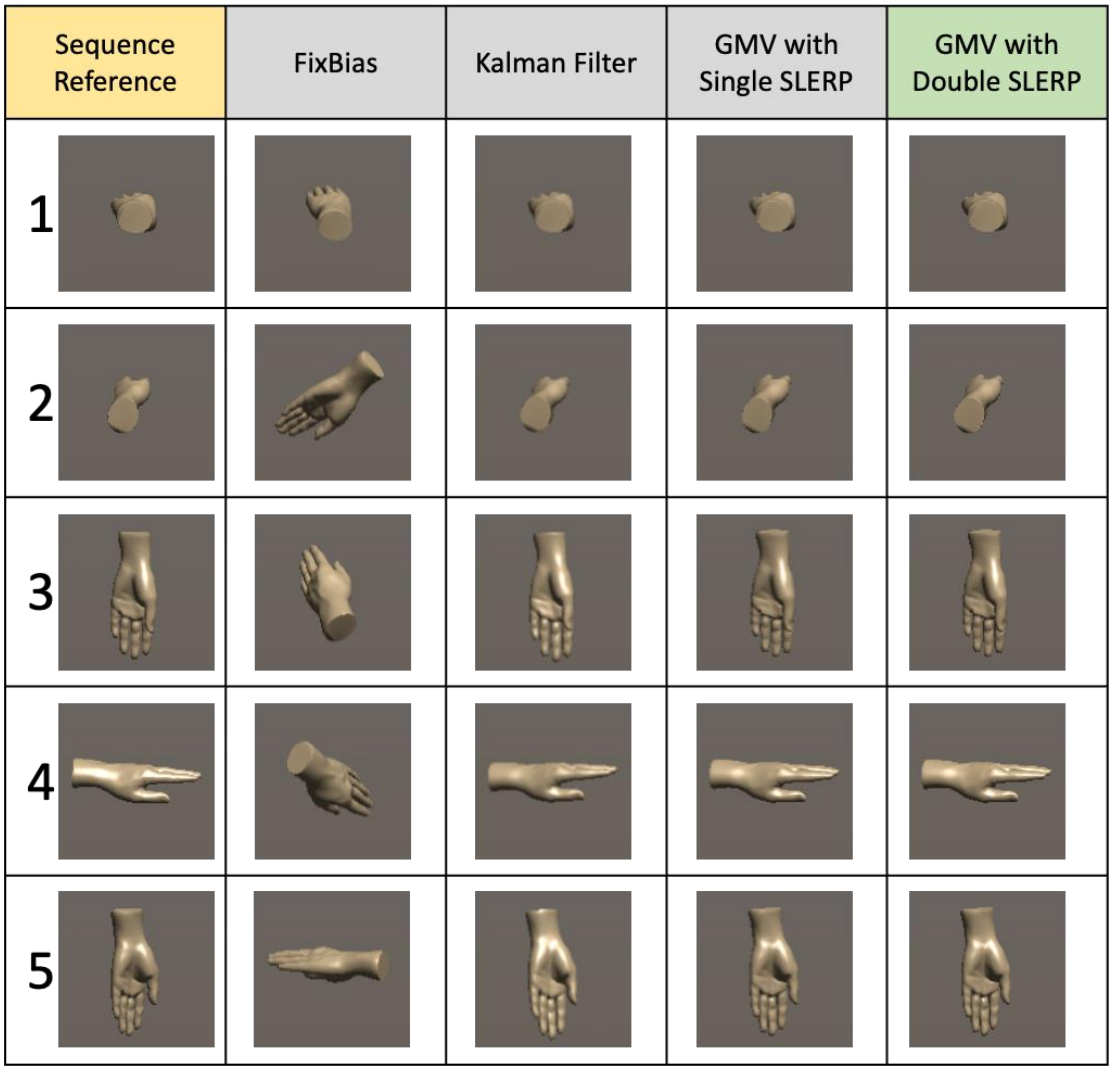

Figure 6.2 3D hand rendering oriented according to the orientation estimation output from 4 different methods while in the non-magnetically distorted area (Poses 1-5)

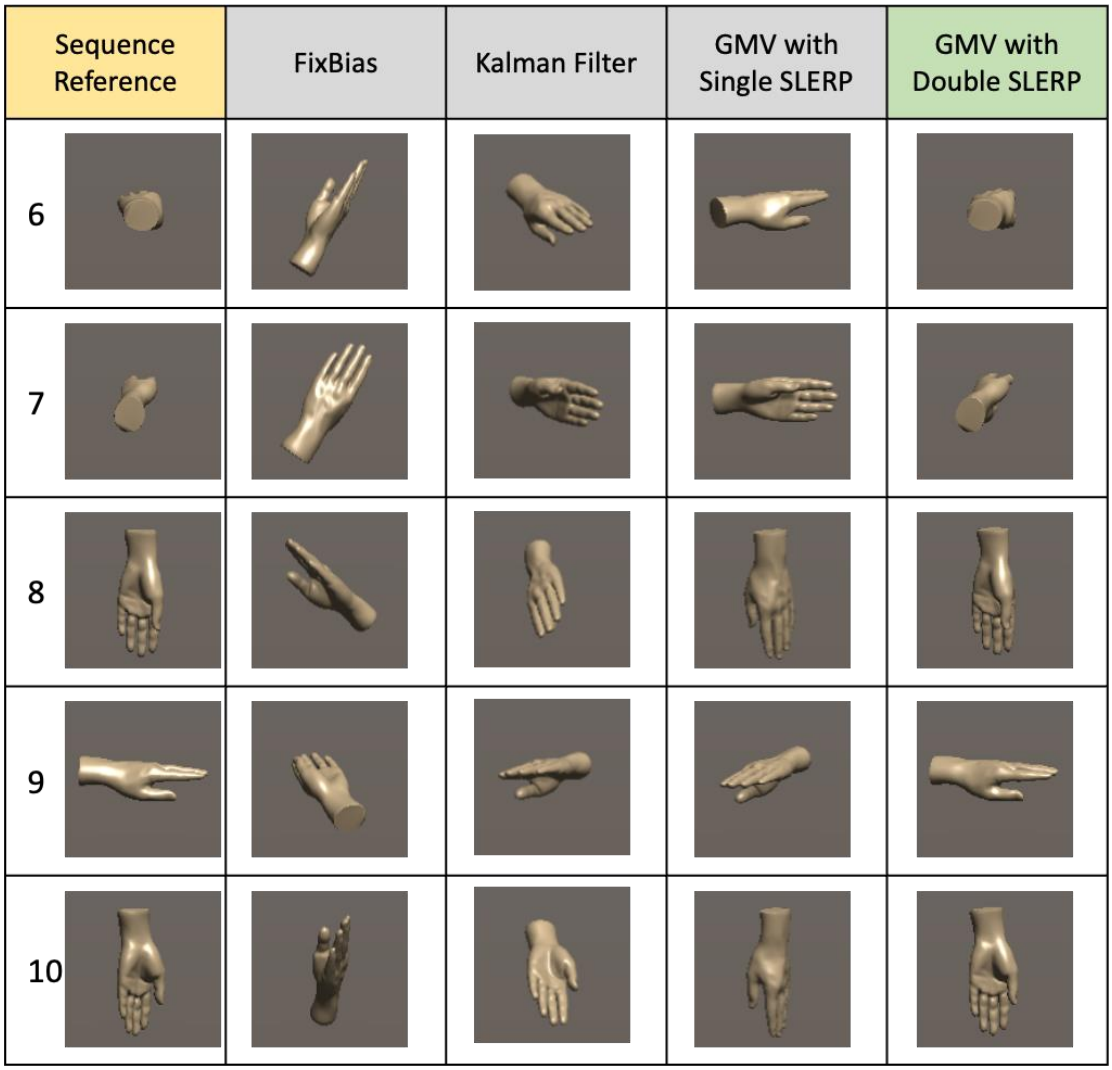

Figure 6.3 3D hand rendering oriented according to the orientation estimation output from 4 different methods while in the magnetically distorted area (Poses 6-10).

6.2 Statistical Evaluations

To quantify the performance of the proposed algorithm, the orientations estimated by the methods implemented while the subjects were sustaining specific instructed poses were analyzed statistically. In the area without magnetic distortion, each subject held 9 poses (First, pose 1, then poses 2, 3, 4 and 5, with a return to Pose 1 after each). Similarly, each subject held 9 poses in the magnetically distorted area (Pose 6 and then 7, 8, 9 and 10 with returns to 6). Since the Fixed Bias method was seen to perform very poorly (Figures 6-1, 6-2 and 6-3), the statistical analysis is concentrated only on 3 algorithms: Kalman Filter (KF), GMV-S, and GMV-D. The

total of 1620 rows of data (30 subjects x 18 orientations x 3 algorithms) were recorded and statistically analyzed using the SPSS statistical package. The recorded data represent the difference between the reference orientation (instructed to the subjects) and the output from the algorithms, measured in terms of the corresponding Euler Angles (Phi, Theta and Psi, which represent the value of the angles rotated about the x, y and z axes). If the orientation algorithm worked correctly, these differences were expected to be 'zero'. The estimated means and standard deviation of the orientation errors in all Euler Angles in both areas (with and without magnetic distortion) is shown in the Table 6.1. It is clearly seen that the means and standard deviation of the orientation errors for GMV-D are much less than that of other two methods (GMV-S, KF) in every Euler Angle. Figure 6.4 to Figure 6.6 show the estimated marginal means of the orientation errors for Phi, Theta and Psi from all methods, respectively.

Table 6.1Estimated means and Standard Deviation of the orientation output. (In degree)

Dependent Variable	Algorithm	Phi	Theta	Psi
GMV-D	Mean	1.858	8.231	3.992
	Std. Deviation	2.658	10.818	8.554
GMV-S	Mean	5.053	38.318	16.104
	Std. Deviation	14.769	52.557	37.527
KF	Mean	11.065	53.452	17.887
	Std. Deviation	17.071	65.382	40.489
Total	Mean	5.992	33.334	12.661
	Std. Deviation	13.659	52.302	32.821
	N	1800	1800	1800

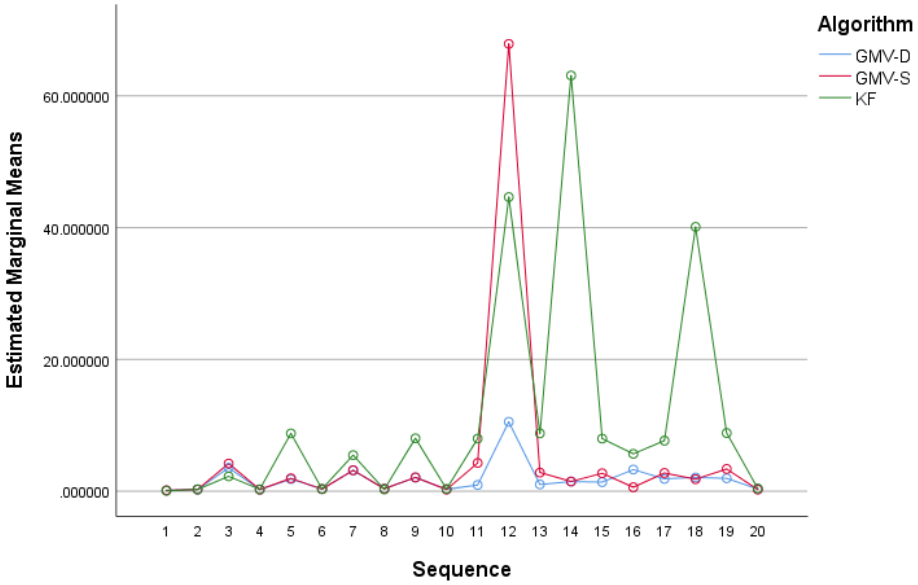

Figure 6.4Estimated Marginal means of the orientation errors for Phi (In degree)

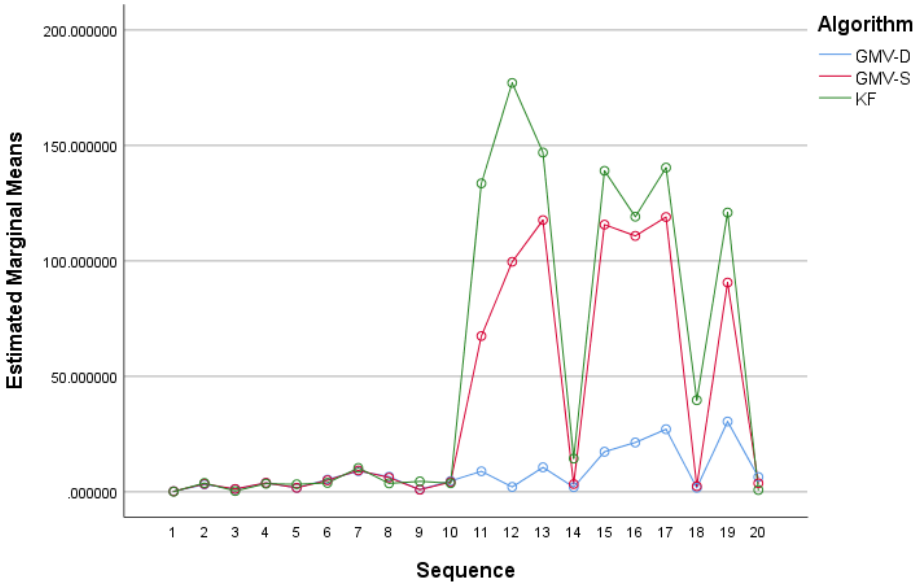

Figure 6.5Estimated Marginal means of the orientation errors for Theta (In degree)

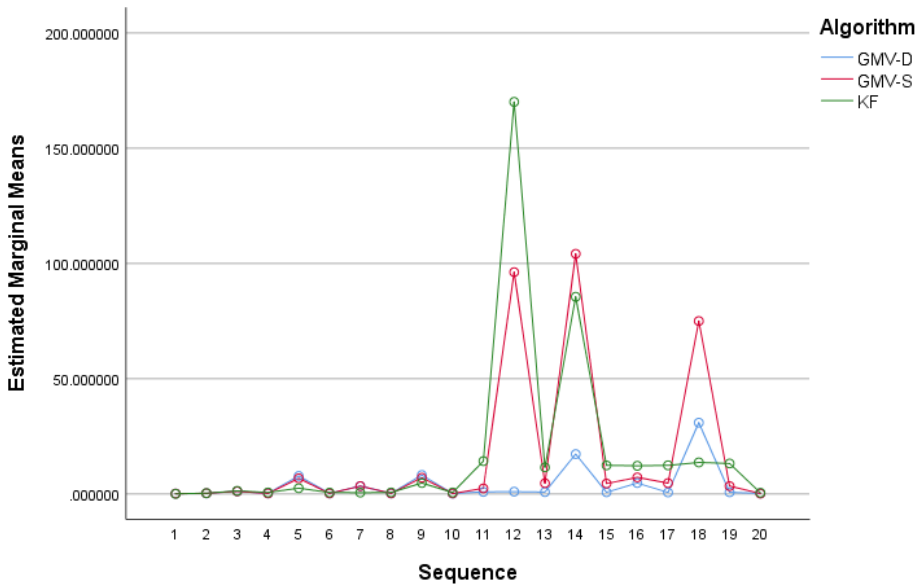

Figure 6.6Estimated Marginal means of the orientation errors for Psi (In degree)

The multivariate analysis of variance (MANOVA) was originally chosen to test for the effects of three algorithms on the orientation output errors. However, the appropriate application of MANOVA analysis requires verification of two key assumptions in the data, which are normality of the error and equal variances across treatments. The null hypothesis for normality test is that the data are normally distributed within each treatment group. The results from the tests of normality (Kolmogorov-Smirnov and Shapiro-Wilk) are shown in Table 6.2 having the p-values of 0.000 for all angles and all methods. These results provided strong evidence that the orientation output errors are not normally distributed, which can be confirmed graphically in the Normal Q-Q plots in Figure 6.7, Figure 6.9, and Figure 6.9, for angles Phi, Theta, and Psi, respectively.

Table 6.2Tests of Normality: Kolmogorov-Smirnov and Shapiro-Wilk

		Kolmogorov-Smirnov[a]			Shapiro-Wilk		
	Algorithm	Statistic	df	Sig.	Statistic	df	Sig.
Phi	GMV-D	.243	600	.000	.591	600	.000
	GMV-S	.424	600	.000	.314	600	.000
	KF	.319	600	.000	.643	600	.000
Theta	GMV-D	.224	600	.000	.692	600	.000
	GMV-S	.348	600	.000	.707	600	.000
	KF	.302	600	.000	.733	600	.000
Psi	GMV-D	.321	600	.000	.498	600	.000
	GMV-S	.412	600	.000	.462	600	.000
	KF	.377	600	.000	.446	600	.000

a. Lilliefors Significance Correction

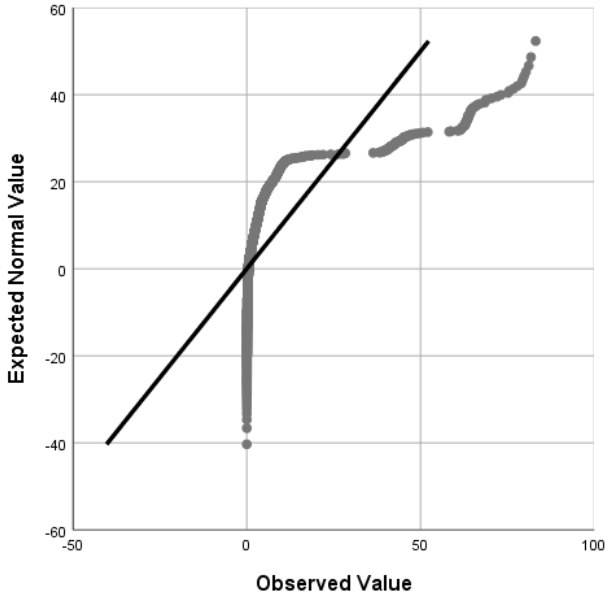

Figure 6.7 The Normal Q-Q plot of Phi

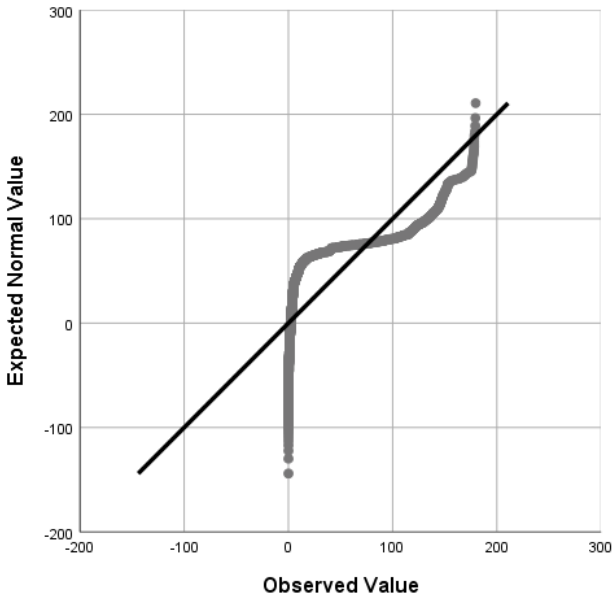

Figure 6.8The Normal Q-Q plot of Theta

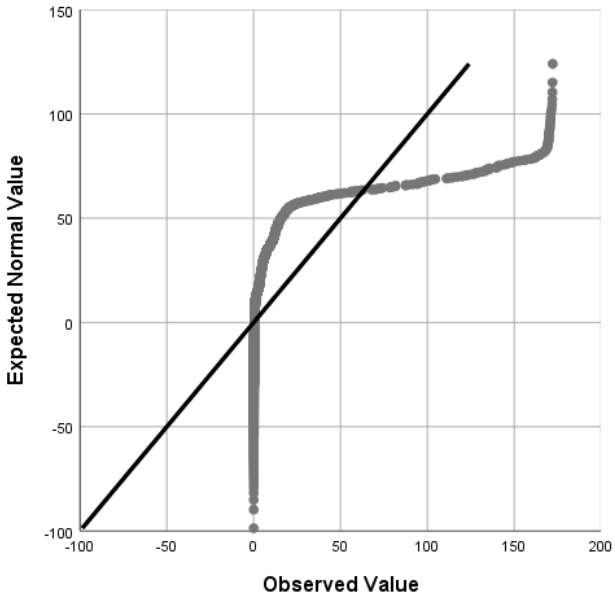

Figure 6.9The Normal Q-Q plot of Psi

Next, the homogeneity of variances was tested with the null hypothesis that the error variance of the dependent variable is equal across treatment groups, yielding the results shown in the Table 6.3. The p-values = .000 from all three dependent variables of the test of homogeneity of variances, provide strong evidence that the error variances are not equal among three treatment groups (GMV-D, GMV-S and KF) which, therefore, results in rejection of the null hypothesis.

Table 6.3Levene's Test of Equality of Error Variances.

		Levene Statistic	df1	df2	Sig.
Phi	Based on Mean	24.062	59	1740	.000
	Based on Median	21.110	59	1740	.000
	Based on Median and with adjusted df	21.110	59	131.746	.000
	Based on trimmed mean	22.299	59	1740	.000
Theta	Based on Mean	61.970	59	1740	.000
	Based on Median	37.068	59	1740	.000
	Based on Median and with adjusted df	37.068	59	193.641	.000
	Based on trimmed mean	58.456	59	1740	.000
Psi	Based on Mean	105.361	59	1740	.000
	Based on Median	64.094	59	1740	.000
	Based on Median and with adjusted df	64.094	59	96.072	.000
	Based on trimmed mean	103.864	59	1740	.000

Dependent variable: Phi, Theta, Psi
Design: Intercept + Algorithm + Sequence + Algorithm * Sequence

As the MANOVA analysis was found not to be appropriate for the data, the nonparametric Kruskal-Wallis H test was chosen to perform the analysis, since it does not require the assumptions of variance homogeneity and normality of errors [72]. The Kruskal-Wallis is a rank-based nonparametric test, commonly used for determining the statistical significance of the differences of a dependent variable across two or more treatment groups [73]. Each dependent variable (Phi, Theta and Psi) was tested with the Kruskal-Wallis approach at a level of significance of 0.05 to determine if there are

differences in means across the three algorithms (treatments). The analysis was performed separately for the poses held in the area that was not magnetically disturbed and the area that was magnetically disturbed.

For the area which was not magnetically distorted, the summary of results in Table 6.4 shows that the distributions of both Phi and Theta were not significantly different across the three algorithms, as shown in more detail by Figure 6.11 and Figure 6.11, with H=5.478, p=0.065 and H=2.439, p=0.295, respectively. The null hypothesis that the distribution of orientation errors is the same across algorithms was rejected only for the Psi angle (Figure 6.12), for which H(2)=14.586, p=0.001, with a mean rank of 381.70 for GMV-S, 384.93 for GMV-D and 449.86 for KF. Through pairwise comparisons, the results indicate that there are no statistically significant differences of the orientation errors in Psi between GMV-S and GMV-D (p=1.000) while KF shows statistically significant differences of the orientation errors with GMV-S (p=0.002) and GMV-D (p=0.004).

Table 6.4Summary results of Kruskal-Wallis Test for the orientation errors in all three angles (Phi, Theta, Psi), across three different methods in the non-magnetically distorted area

Hypothesis Test Summary

	Null Hypothesis	Test	Sig.	Decision
1	The distribution of Phi is the same across categories of Algorithm.	Independent-Samples Kruskal-Wallis Test	.065	Retain the null hypothesis.
2	The distribution of Theta is the same across categories of Algorithm.	Independent-Samples Kruskal-Wallis Test	.295	Retain the null hypothesis.
3	The distribution of Psi is the same across categories of Algorithm.	Independent-Samples Kruskal-Wallis Test	.001	Reject the null hypothesis.

Asymptotic significances are displayed. The significance level is .05.

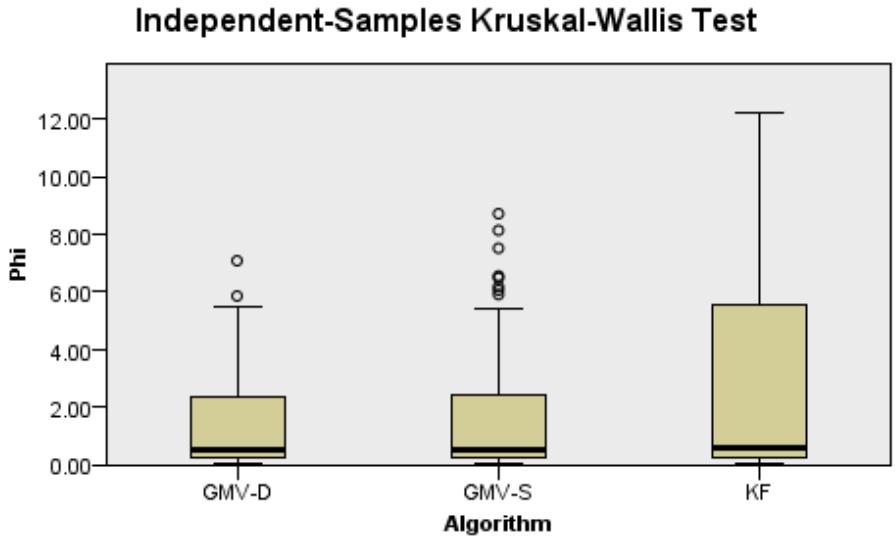

Total N	810
Test Statistic	5.478
Degrees of Freedom	2
Asymptotic Sig. (2-sided test)	.065

1. The test statistic is adjusted for ties.
2. Multiple comparisons are not performed because the overall test does not show significant differences across samples.

Figure 6.10 Kruskal-Wallis test statistics results for the orientation errors in the Euler angle Phi, across three different methods in the non-magnetically distorted area.

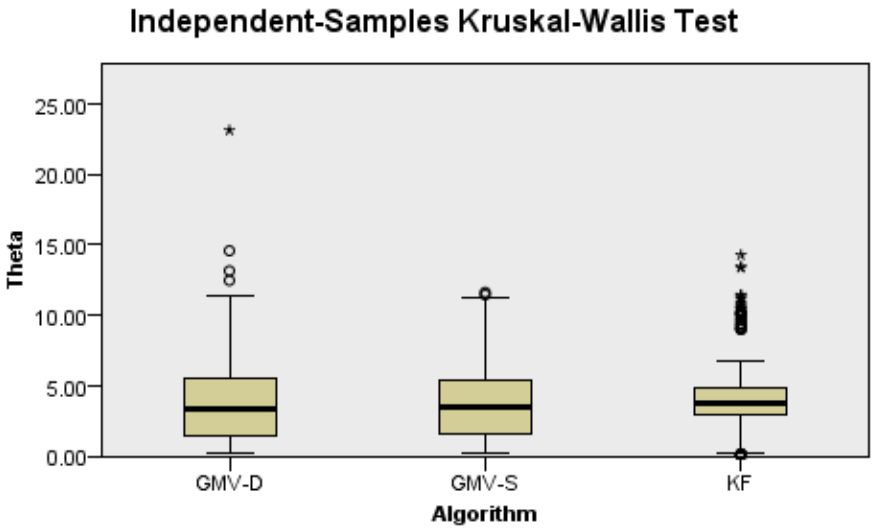

Total N	810
Test Statistic	2.439
Degrees of Freedom	2
Asymptotic Sig. (2-sided test)	.295

1. The test statistic is adjusted for ties.
2. Multiple comparisons are not performed because the overall test does not show significant differences across samples.

Figure 6.11 Kruskal-Wallis test statistics results for the orientation errors in the Euler angle Theta, across three different methods in the non-magnetically distorted area.

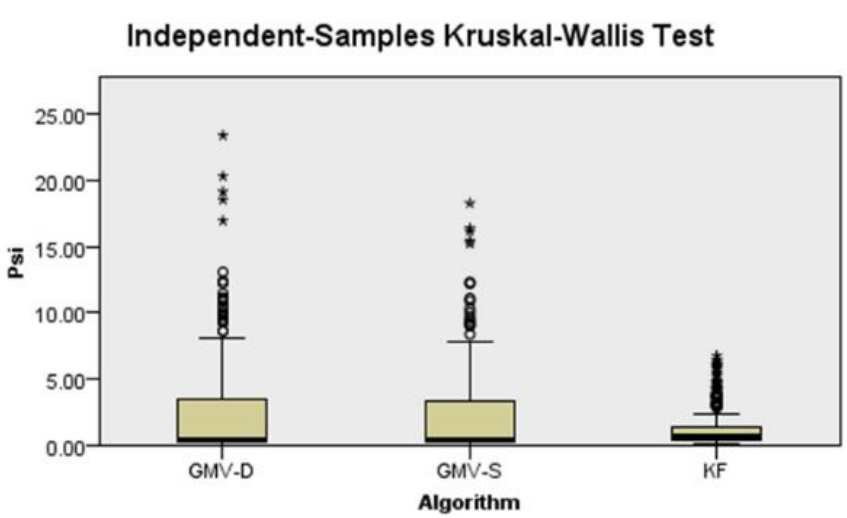

Total N	810
Test Statistic	14.586
Degrees of Freedom	2
Asymptotic Sig. (2-sided test)	.001

1. The test statistic is adjusted for ties.

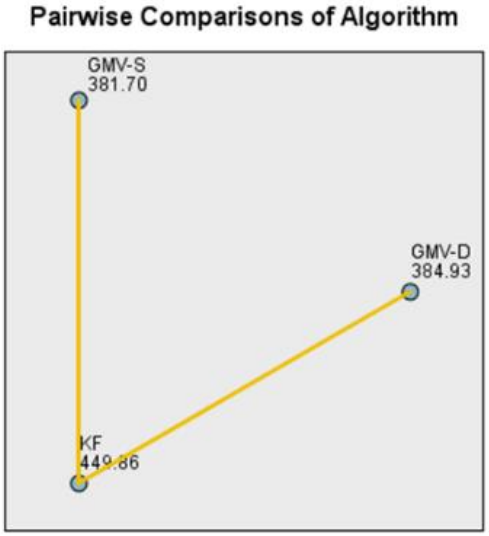

Each node shows the sample average rank of Algorithm.

Sample1-Sample2	Test Statistic	Std. Error	Std. Test Statistic	Sig.	Adj.Sig.
GMV-S-GMV-D	3.230	20.137	.160	.873	1.000
GMV-S-KF	-68.159	20.137	-3.385	.001	.002
GMV-D-KF	-64.930	20.137	-3.224	.001	.004

Each row tests the null hypothesis that the Sample 1 and Sample 2 distributions are the same.
Asymptotic significances (2-sided tests) are displayed. The significance level is .05.
Significance values have been adjusted by the Bonferroni correction for multiple tests.

Figure 6.12Kruskal-Wallis test statistics results for the orientation errors in the Euler angle Psi, across three different methods in the non-magnetically distorted area.

For the area affected by magnetic distortion, Table 6.5 shows the test summary, which leads to rejection of the null hypothesis that the distribution of orientation errors for all the angles (Phi, Theta and Psi) is the same across algorithms.

Figure 6.13 shows the test statistics for the orientation output errors in the Euler Angle Phi, across the three algorithms. In this test the null hypothesis is that the distribution of orientation errors is the same across the algorithms. The results from the test indicate that there is a statistically significant difference between the orientation errors in Phi produced by different algorithms ($H(2) = 365.929$, $p = 0.000$), with a mean rank of 252.20 for GMV-D, 342.62 for GMV-S and 621.69 for KF. Through pairwise comparisons among the three algorithms, it was found that there are statistically significant differences of the orientation errors in Phi between GMV-D and GMV-S ($p = 0.000$), between GMV-D and KF ($p = 0.000$), and between GMV-S and KF ($p = 0.000$). GMV-D shows the best performance, which is 9.539 less than GMV-S and 16.631 less than KF, in standard test statistic value.

Figure 6.14 shows the test statistics for the orientation output errors in the Euler Angle Theta, across the three algorithms. In this test the null hypothesis is that the distribution of orientation errors is the same across the algorithms. The results from the test indicate that there is a statistically significant difference between the orientation errors in Theta produced by the different algorithms ($H(2) = 377.616$, $p = 0.000$), with a mean rank of 197.76 for GMV-D, 432.47 for GMV-S and 586.27 for KF. Through pairwise comparisons among the three algorithms, it was found that there are statistically significant differences of the orientation errors in Theta between GMV-D and GMV-S ($p = 0.000$), between GMV-D and KF ($p = 0.000$), between GMV-S and KF ($p = 0.000$). GMV-D shows the best performance, which is 11.656 less than GMV-S and 19.293 less than KF in standard test statistic value.

Figure 6.15 shows the test statistics for the orientation output errors in the Euler Angle Psi, across the three algorithms. In this test the null hypothesis is that the distribution of orientation errors is the same across the algorithms. The results from the test indicate that there is a statistically significant difference between the orientation errors in Psi for different algorithms (H(2) = 278.583, p = 0.000), with a mean rank of 229.84 for GMV-D, 421.93 for GMV-S and 564.73 for KF. Through pairwise comparisons among the three algorithms, it was found that there are statistically significant differences of the orientation errors in Psi between GMV-D and GMV-S (p = 0.000), between GMV-D and KF (p = 0.000), and between GMV-S and KF (p = 0.000). GMV-D shows the best performance, which is 9.539 less than GMV-S and 16.631 less than KF in standard test statistic value.

Table 6.5Summary results of Kruskal-Wallis Test for the orientation errors in all three angles (Phi, Theta, Psi), across three different methods at the magnetic distortion area

Hypothesis Test Summary

	Null Hypothesis	Test	Sig.	Decision
1	The distribution of Phi is the same across categories of Algorithm.	Independent-Samples Kruskal-Wallis Test	.000	Reject the null hypothesis.
2	The distribution of Theta is the same across categories of Algorithm.	Independent-Samples Kruskal-Wallis Test	.000	Reject the null hypothesis.
3	The distribution of Psi is the same across categories of Algorithm.	Independent-Samples Kruskal-Wallis Test	.000	Reject the null hypothesis.

Asymptotic significances are displayed. The significance level is .05.

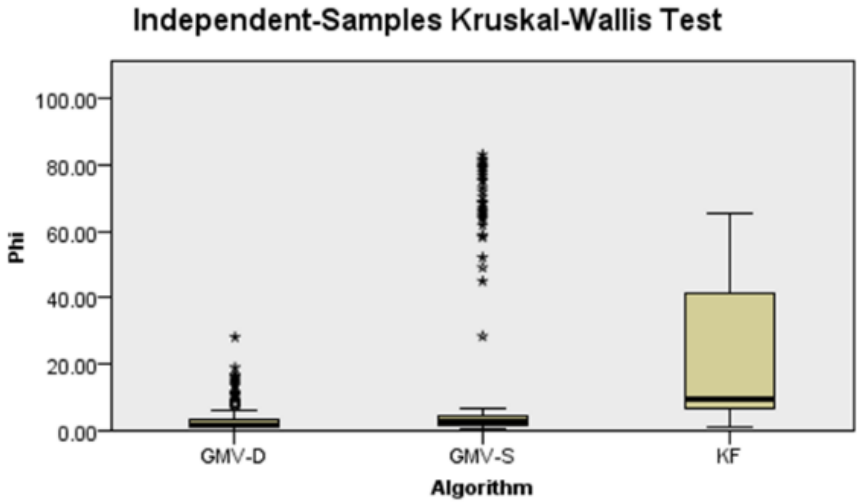

Total N	810
Test Statistic	365.929
Degrees of Freedom	2
Asymptotic Sig. (2-sided test)	.000

1. The test statistic is adjusted for ties.

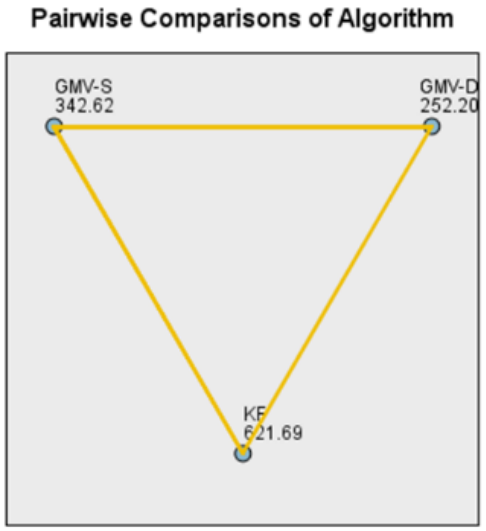

Each node shows the sample average rank of Algorithm.

Sample1-Sample2	Test Statistic	Std. Error	Std. Test Statistic	Sig.	Adj.Sig.
GMV-D-GMV-S	-90.422	20.137	-4.490	.000	.000
GMV-D-KF	-369.489	20.137	-18.349	.000	.000
GMV-S-KF	-279.067	20.137	-13.858	.000	.000

Each row tests the null hypothesis that the Sample 1 and Sample 2 distributions are the same.
Asymptotic significances (2-sided tests) are displayed. The significance level is .05.
Significance values have been adjusted by the Bonferroni correction for multiple tests.

Figure 6.13Kruskal-Wallis test statistics results for the orientation errors in the Euler angle Phi, across three different methods in the magnetically distorted area.

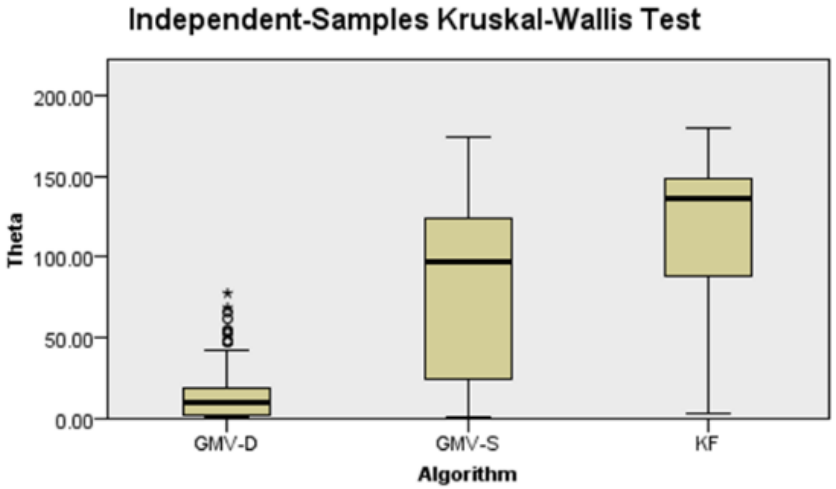

Total N	810
Test Statistic	377.616
Degrees of Freedom	2
Asymptotic Sig. (2-sided test)	.000

1. The test statistic is adjusted for ties.

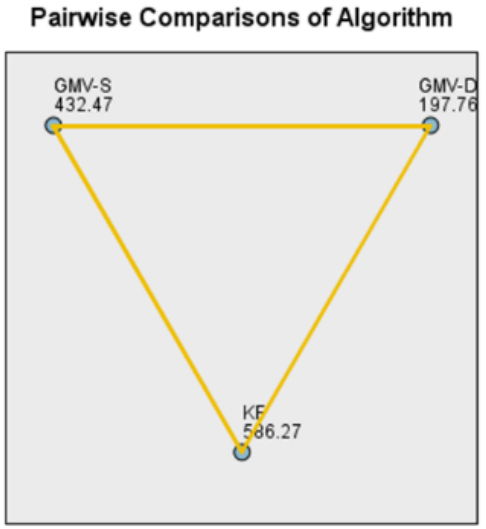

Each node shows the sample average rank of Algorithm.

Sample1-Sample2	Test Statistic	Std. Error	Std. Test Statistic	Sig.	Adj.Sig.
GMV-D-GMV-S	-234.711	20.137	-11.656	.000	.000
GMV-D-KF	-388.511	20.137	-19.293	.000	.000
GMV-S-KF	-153.800	20.137	-7.638	.000	.000

Each row tests the null hypothesis that the Sample 1 and Sample 2 distributions are the same.
Asymptotic significances (2-sided tests) are displayed. The significance level is .05.
Significance values have been adjusted by the Bonferroni correction for multiple tests.

Figure 6.14Kruskal-Wallis test statistics results for the orientation errors in the Euler angle Theta, across three different methods in the magnetically distorted area.

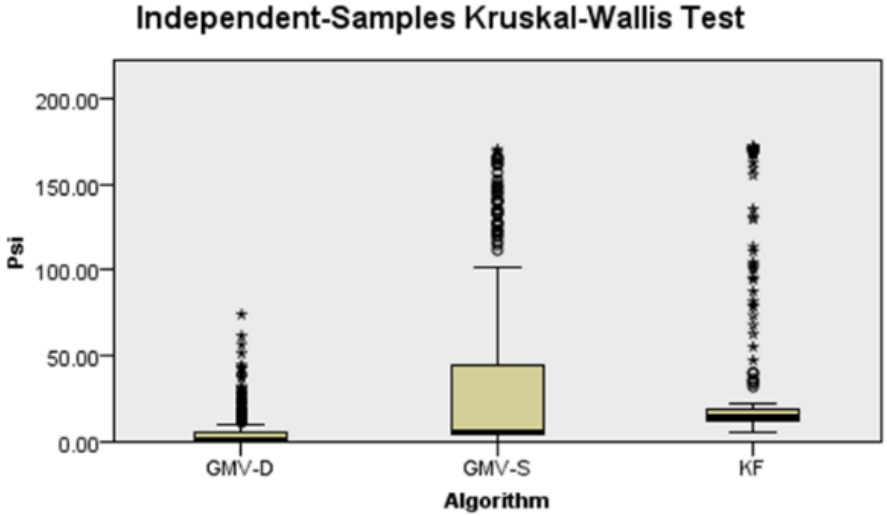

Total N	810
Test Statistic	278.583
Degrees of Freedom	2
Asymptotic Sig. (2-sided test)	.000

1. The test statistic is adjusted for ties.

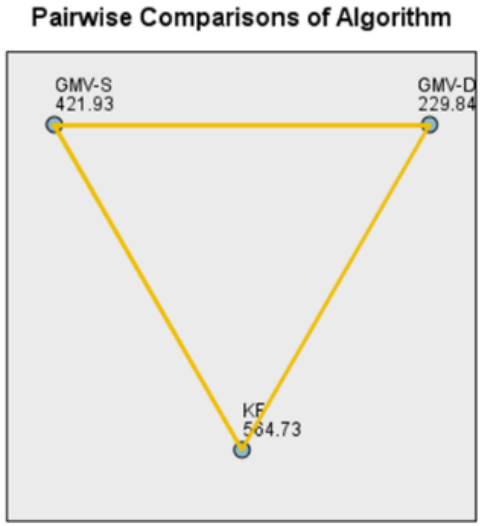

Sample1-Sample2	Test Statistic	Std. Error	Std. Test Statistic	Sig.	Adj.Sig.
GMV-D-GMV-S	-192.093	20.137	-9.539	.000	.000
GMV-D-KF	-334.896	20.137	-16.631	.000	.000
GMV-S-KF	-142.804	20.137	-7.092	.000	.000

Each row tests the null hypothesis that the Sample 1 and Sample 2 distributions are the same.
Asymptotic significances (2-sided tests) are displayed. The significance level is .05.
Significance values have been adjusted by the Bonferroni correction for multiple tests.

Figure 6.15Kruskal-Wallis test statistics results for the orientation errors in the Euler angle Psi, across three different methods in the magnetically distorted area.

CHAPTER 7 - DISCUSSION

The preceding sections, overall, have shown results that match the key intent of the development of the newly proposed algorithm, GMV-D, which was to make the orientation estimation derived from signals of the MARG module more robust in circumstances where distortion of the geomagnetic field exist.

The evaluation procedure was defined in such a way that its first half would take place within a region of space where the geomagnetic field was not distorted non-magnetically distorted area), whereas the second half took place in the immediate neighborhood of the iron bar, which was known to introduce significant distortion of the magnetic field (magnetically distorted area).

The initial assessment, comprising the plotting of the 4 components of the orientation quaternions output by the 4 methods compared (Fixed Bias, Kalman Filter, GMV-S and the newly proposed GMV-D), was performed for the complete duration of the experimental task, as a whole. Its results are shown in Figure 6.1. However, with the exception of the Fixed Bias approach, which shows progressive degradation in performance that starts immediately after the beginning of the experiment and is found in both the areas (with and without magnetic distortion), the remaining 3 algorithms display very different behaviors for the first and second halves of the experiment. Before the green vertical dividing line Figure 6.1, KF, GMV-S and GMV-D perform in almost identical fashion, which seems to reflect correct orientation estimates for the multiple poses instructed to the subjects in this first half. In contrast, while the poses held after the subject translated the MARG module to the magnetically distorted zone (i.e., after the green dividing line in Figure 6.1) were exactly the same poses as previously executed in the non-magnetically distorted area, the quaternion outputs of

KF and GMV-S do not appear similar to their outputs for the first half. This indicates that significant orientation estimation errors were introduced in the results from KF and GMV-S while at the magnetically distorted area. Only the bottom traces in Figure 6.1, corresponding to the approach proposed in this dissertation (GMV-D) displays traces that are essentially the same in the first and the second half of the experiment, as they were expected to be. It is, however, not easy to perceive the importance of the orientation errors suspected in the outputs from KF and GMV-S through the second half of the experiment, from the plots in Figure 6.1.

The effective importance of the orientation errors is better appreciated when the output quaternions from the 4 methods are used to determine the attitude of a 3D virtual hand in the Unity software package and renderings of that 3D hand are obtained at the times when the subjects were instructed to hold specific poses (Poses 1- 5 in the non-magnetically distorted area and Poses 6-10 in the magnetically distorted area).

Figure 6.2 compares the renderings of the 3D hand with its orientation driven by the quaternion results from Fixed Bias, KF, GMV-S and GMV-D, in columns 2, 3, 4, and 5, respectively, at the poses identified with numbers 1-5, in the non-magnetically distorted area. For reference, the first column shows renderings of the 3D hand taking on the reference orientation that the subjects were instructed to execute. It can be seen that, in the non-magnetically distorted area, other than the Fixed Bias method, all remaining orientation estimators did not introduce visually significant errors.

In contrast, Figure 6.3, which displays the 3D hand for Poses 6 to 10, executed in the magnetically distorted area, shows that only the proposed GMV-D method (rightmost column) resulted in 3D hand orientations that are visually perceived as similar to the reference orientations (leftmost column). This confirms the suspected additional robustness to magnetic distortion that was achieved by the GMV-D method.

Figure 6.1, Figure 6.2, and Figure 6.3 were created from orientation results from the completion of one representative experiment, performed by one of the volunteer subjects. However, it was also necessary to evaluate the results accounting for the diversity of trajectories, movement speed, etc. that various human subjects would use in completing the experimental task, as the subject is meant to be part of a human-computer interaction system. To that end, 30 volunteer subjects were asked to perform the experimental protocols and the orientation results generated for all the poses by them were recorded. To investigate the deviations of those recorded orientations from the "instructed orientations" ("ground truth") and in order to report the results in a more intuitive way, the orientation errors were expressed as Euler Angles, which are the errors around the 3 orthogonal axes of the "body frame" of the MARG module. These angles (Phi, Theta and Psi) are the angles rotated about the x, y and z axes, and can, therefore, be more readily interpreted than the 4 numerical components of a quaternion. Since the analysis was performed on angular errors, a lower mean value found for a given method than for another implies that the former performed better that the latter.

Proceeding on these bases, the statistical analysis of error for the 3 Euler Angles was performed separately for the poses in the first half of the experimental procedure (in the non-magnetically distorted area) and for the poses in the second half of the experimental procedure (in the magnetically distorted area. Additionally, only the 3 orientation estimation methods that were seen to perform reasonably well (KF, GMV-S and GMV-D) were included in this second level of analysis.

For the non-magnetically distorted area Table 6.4, shows that, as expected the performance of KF, GMV-S and GMV-D without magnetic distortions was very similar. Only the distribution of errors in Psi was found to be significantly different across the 3 methods. A more detailed analysis, summarized in Figure indicated that

GMV-S and GMV-D still yielded similar values of their mean ranks (381.70 and 384.93, respectively), while KF had a more different mean rank at 449.86. This is reinforced by the results of pairwise comparisons, which only found significant differences between KF and GMV-S and between KF and GMV-D, but not between GMV-S and GMV-D.

The results from the poses held in the magnetically distorted area, summarized in Table 6.5, are very different. The Kruskal-Wallis test indicated that the null hypothesis of similar level of errors across orientation estimation errors must be rejected, for all the Euler Angles. That means, in brief, that the levels of orientation error, as represented by the errors in the Phi, Theta and Psi Euler Angles was definitely not the same across orientation estimation methods when they were employed in the magnetically distorted area.

Looking into the performance for each specific angle a consistent pattern was found, in which the newly proposed GMV-D algorithm reported the lowest mean rank from the three algorithms, followed by GMV-S and KF recorded the highest mean ranks, with respect to all 3 of the Euler Angles. For all 3 of the Euler Angles, pairwise comparisons confirmed that there were significant differences in error between every possible pair of these 3 methods (KF vs. GMV-S, KF vs. GMV-D and GMV-S vs. GMV-D).

Overall, the statistical results for the errors that were recorded confirm the intuitive perception that is derived from observation of the plots representing the marginal means of orientation errors for Phi, Theta and Psi, in Figure 6.4, Figure 6.5, and Figure 6.6, respectively. Focusing on the second (right) half of these plots, which corresponds to poses held while in the magnetically distorted area, the errors for GMV-

D are typically lowest, with errors from GMV-S at an intermediate level and errors from KF typically being the highest.

Then, it can be summarized that the provisions included in the proposed GMV-D orientation estimation algorithm, for progressive assessment of the level of distortion of the geomagnetic filed in specific regions of the operating space of the MARG module has made it possible to avoid the introduction of strong orientation errors in its final estimate that judiciously fuses the original orientation assessment based on integration of gyroscope signals with weighted corrections from the accelerometer and magnetometer signals. The addition of magnetic distortion capability, the new formulation of a magnetic correction trustworthiness parameter (μ) and the use of two tiers of SLERP correction of the initial dead reckoning orientation estimate appear to have, indeed, enhanced the performance in magnetically disturbed areas beyond that of the previous GMV-S algorithm.

It can be speculated that, while all 3 of the methods compared in detail: KF, GMV-S and GMV-D derived their orientation estimates from all 3 of the sensor modalities (gyroscope, accelerometer and magnetometer), it is the higher level of adaptability in GMV-D that has yielded the best performance. The Kalman Filter internally implemented by the 3-Space Embedded MARG used for the experiments does not have any specific provisions to modify the items in the Kalman Filtering algorithm that weigh the value of the accelerometer or magnetometer corrections (the covariance matrices corresponding to these measurements). Therefore, these covariance matrices were kept constant throughout the experimental process. The GMV-S algorithm includes the assessment of the acceleration correction trustworthiness parameter, α, on a sample-by sample basis, but it did not include a similar parameter to represent the magnetic correction trustworthiness, and, therefore,

adapts the weighted mixture of accelerometer and magnetometer corrections on the exclusive knowledge of the accelerometer correction trustworthiness. This may allow inappropriately large influence of the magnetometer correction when the accelerometer correction is not highly reliable, even if the MARG module is located in a magnetically disturbed area where that strong involvement of the magnetic correction could lead to orientation errors. Only the GMV-D approached, proposed in this dissertation performs a concurrent and independent assessment of the trustworthiness of both the accelerometer and the magnetometer corrections and defines its final orientation estimate by fusion of both corrections using trustworthiness measures that are updated on a sample-by-sample basis.

Lastly, it should also be noted that the performance of parallel and separate processing of correction quaternions ($\Delta q_{A \text{ and }} \Delta q_{M}$), which are kept independent and individually accessible until the last steps of each iteration of the GMV-D algorithm, opens up possibilities for manipulations that may extract valuable information from these items towards future enhancements of the algorithm. This is in marked contrast with the ways in which corrective measurement information is blended into the global results in early stages of other information fusion approaches for orientation estimation, such as the Kalman Filter.

CHAPTER 8 – ADAPTING GMV-D FOR NEW MARG MODULES

Today, microelectromechanical system (MEMS) sensors are used in many electronic devices such as medical instruments, smartphones, smartwatches, IoT module, autonomous vehicles, etc. Allied Market Research reported that in 2018 the global MEMS sensor market was valued at $25.7 million and expected to grow and reach $60.6 million by 2026 [74]. This highly competitive market causes the decline of selling price for these devices, while the manufacturer has to enhance their performance, for instance, by offering improvements in key characteristics, such as: accuracy, power consumption, sizes, functions, etc.

Yost Labs is one of the commercial MEMS sensor providers. They name their product in this category as “3-Space Sensors”, offering different members of this line with prices that range from as low as $12.50 (the IC alone) to $205.00 and continue to develop and introduce more product to serve the sensor market. The section below will describe a few 3-Space sensors that may be of interest to continue developing the research presented in this dissertation.

8.1 Specification

In this research, the specific MARG model used for implementation was the 3-Space™ Micro USB. Table 8.1 shows a comparison between the 3-Space™ Micro USB and other models recently introduced by the Yost Labs company, which may be used for future development of this research.

Table 8.1Three model of 3-Space sensors provided by Yost Labs

Model	Micro USB	LX Embedded	Nano IC
Photo			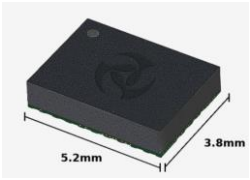
Dimension	23x23x2.2 mm	16x15x1.7 mm	3.8x5.3x1.1 mm
Weight	1.3 g	0.9 g	0.01 g
Power Consumption	45mA @ 5v	22mA @ 3.3V	20mA @3.3V
Orientation Accuracy	+/- 1 Deg	+/- 1.5 Deg	+/- 1.5 Deg
Gyro Bias Stability	2.5 Deg/hr	11 Deg/hr	11 Deg/hr
Filter	Kalman, QCOMP	QGRAD2	QGRAD2
Confidence value (Stillness): 0x2D	YES	NO	NO
Price	$65	$37.50-$75	$12.50-$25

8.2 Motionlessness Algorithm

From Table 8.1, it is clear that the new generations of MARG modules, such as Yost Labs' LX Embedded and Nano IC, provide advantages in terms of smaller sizes, lower weight and lower power consumption, which will make them even more appropriate for their use in an instrumented glove. However, Table 8.1 also indicates that an explicit, user-readable parameter of "Confidence" (which indicates, in a range from 0 to 1, how much the MARG module is currently moving) may not be available in the newer modules from Yost Labs. Similarly, this type of parameter may not be available from MARG modules from other manufacturers.

As the orientation estimation algorithm proposed in this dissertation currently uses the "Confidence" parameter provided by the 3-Space Micro USB module, this section proposes a mechanism to define an equivalent floating-point variable, which

will be called “Motionlessness (MTNLNS)”, directly from the 3 types of measurements carried out by all MARG modules

The confidence factor provided by the Micro USB module has a range of values from 0 to 1, where 1 indicates that the sensor is static [41]. In the proposed orientation estimation algorithm, that confidence factor is used to calculate the value of “alpha”, which defines the weight given to the accelerometer correction (q_{GA}).

The “Motionlessness” variable was created to substitute the Confidence Factor as defined below. The new MTNLNS parameter was defined by processing the signals from both the gyroscope axes and the accelerometer axes. Two separate versions, $Gyro_{MTNLNS}(i)$ and $Accel_{MTNLNS}(i)$, were calculated, and each of them was filtered to yield a contribution towards a new formulation of the alpha parameter used in our GMV-D algorithm.

The version of MTNLNS derived from accelerometer measurements is calculated according to Equations 7.1 and 7.2, where Th_{MTNLNS} is the sensitivity control of MTNLNS (default Th_{MTNLNS} = 0.5).

$$\Delta Gyro(x,y,z) = |Gyro_x(i) - Gyro_x(i-1)|, |Gyro_y(i) - Gyro_y(i-1)|, |Gyro_z(i) - Gyro_z(i-1)| \quad (7.1)$$

If max $(\Delta Gyro(i)) \leq Th_{MTNLNS}$;

$$\|Gyro_{MTNLNS}(i)\| = 1 - \frac{\max(\Delta Gyro(i))}{Th_{MTNLNS}} \quad (7.2)$$

Otherwise; $\|Gyro_{MTNLNS}(i)\| = 0$

Once the gyroscope version of motionlessness has been calculated, then the Gamma filter is applied to smoothen the signal and obtained the alpha value from Gyroscope (α_{Gyro}).

Similarly, to retrieve the alpha value from accelerometer (α_{Acc}), the same process is applied to the data from accelerometer (x, y, z). That is $Accel_{MTNLNS}(i)$ is calculated

by equations like 7.1 and 7.2, but using accelerometer readings, instead. $Accel_{MTNLNS}(i)$ is also processed through the Gamma filter to yield α_{Acc}.

After the Alpha value from both accelerometer and gyroscope were obtained, as shown in Figure 8.1, we studied the possibilities of fusing them as an average or by multiplying their values, i.e.., finding the product of their two values at every sampling instant. For the product method, it was found that the resulting overall alpha value would more closely the alpha derived from the "confidence" (stillness) internally calculated by the Micro USB module if an offset of 0.1 is applied to the product of the individual alphas. Figure 8.2 shows that the alpha obtained by the product method with 0.1 offset displays very similar trends as the alpha calculated from the "stillness" ("confidence") parameter offered by the Micro USB module. In fact, the alpha from the product method tends to be more "conservative" in indicating a static condition for the MARG module, which will probably result in increased reliability of the accelerometer corrections, when they are fully enabled by large values of alpha.

Figure 8.1Alpha value obtained from Gyroscope data (top), and Accelerometer data (bottom).

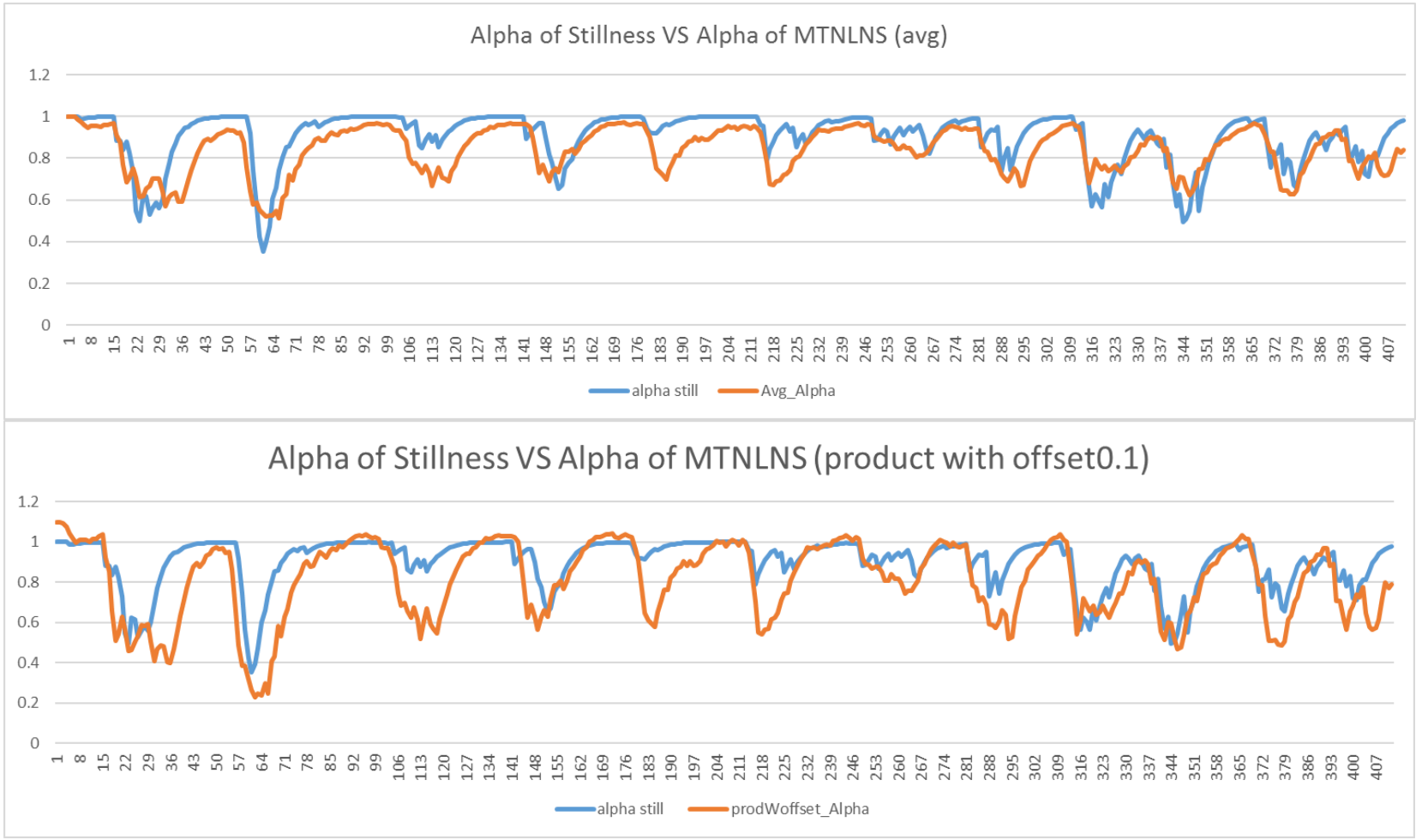

Figure 8.2Comparison between Stillness vs Motionlessness with Average method (top) and after applied offset product (bottom)

As a further means to compare the alpha values calculated from the "confidence" or "stillness" parameter provided by the MICRO USB MARG module and the alpha that can be calculated as average or product of alphas derived from the $Gyro_{MTNLNS}$ and the $_{Accel}MTNLNS$, Figure 8.3 shows the intervals at which the 3 versions of alpha surpass 0.9, in reaction to the gyroscope and accelerometer signals displayed in Figure 8.1. For the alpha derived from the "stillness" parameter the intervals where its value surpassed 0.9 are drown at a height of 1 according to the scale in the right margin of the figure. For the alpha variables defined as average and product of α_{Gyro} and α_{Acc}, the intervals above the 0.9 threshold have been drawn at a heigh of 1 but following the (larger) scale that appears on the left margin of the figure (This was intended to make the traces more easily discernable). This figure confirms that the average combination of alphas and (particularly) the product combination of alphas is actually slightly more conservative than the alpha from the "stillness: parameter.

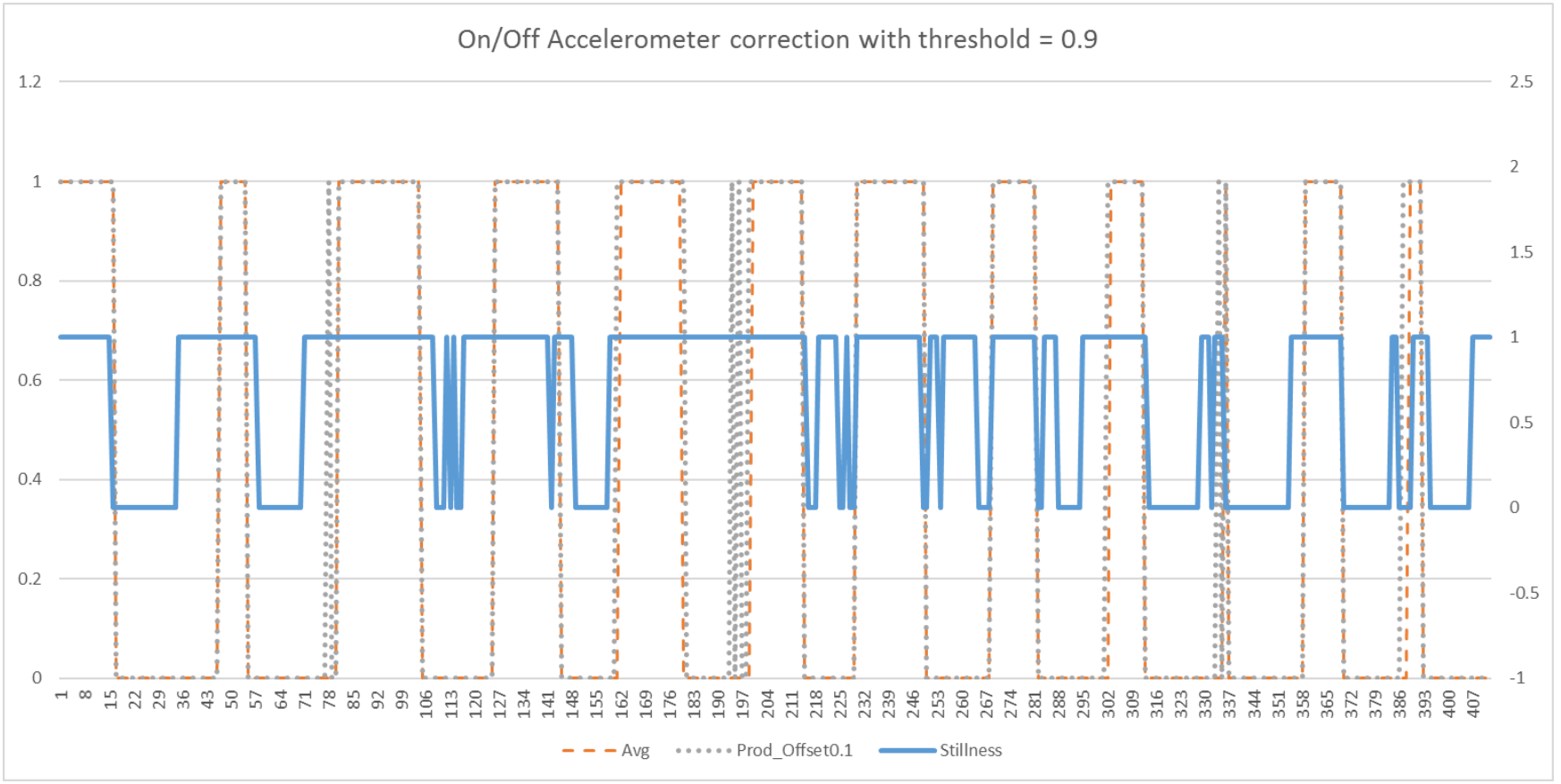

Figure 8.3Square wave pulse showing on/off Accelerometer Correction periods

CHAPTER 9 - CONCLUSION AND FUTURE WORK

9.1 Conclusion

This research aimed to create a robust system that can determine, in real-time, the correct orientation of a MEMS MARG module so that multiple MARG modules can be embedded in an instrumented glove that will report the real-time position, orientation, and configuration of the hand of a computer user, enabling new avenues for hand-gesture-based human-computer interaction.

When miniature MEMS accelerometers and gyroscopes were first introduced in the late 1990s and early 2000s, there were hopes that these devices could be used for determining orientation and position in ways similar to the use of their large-scale counterparts for aircraft navigation. However, it was soon found that the much poorer performance characteristics of the MEMS sensors prevented the direct use of the same processing approaches as used for larger devices. In particular, MEMS gyroscopes have been found to have significant and varying levels of "offset," i.e., non-zero output that is generated when the sensor is actually not turning. As the output of the gyroscopes must be integrated to calculate orientation, even small levels of gyroscope offset will cause high levels of "drift" error in the orientation estimation. Further, this error will tend to rapidly and linearly grow with respect to time. Designers have sought to apply frequent corrections to the orientation calculated from the signals of the gyroscope using information from the accelerometer that usually accompanied the MEMS gyroscopes and even from MEMS magnetometers which began to be included in the sensor packages that were then called Magnetic, Angular-Rate, Gravity (MARG) Sensors. However, accelerometer corrections should only be applied when the module is static so that the accelerometer reports only the acceleration of gravity, and

magnetometer corrections should only be applied if the local geomagnetic field measured by the device is not distorted due to the presence of a nearby medium or large ferromagnetic objects.

This dissertation pursued the definition and evaluation of a novel processing approach that could achieve real-time robust orientation estimation for a typical MARG module in the context of human-computer interaction. This context implies that a 3-camera IR-video system can be used to determine the approximate position of the MARG module, which allowed the novel idea of mapping the level of magnetic trustworthiness (encoded in a parameter $0 < \mu < 1$) of small regions of the working space of the device. This is used to reduce the weight given to the magnetic correction component where the magnetic field is distorted, enhancing the robustness of the system.

At the beginning of the work reported in this dissertation, the first research question asked if the gyroscope drift artifact could be controlled by performing appropriate corrections using information from the accelerometer and magnetometer. The results in Chapter 6 indicate that the proposed algorithm, GMV-D, was successful in avoiding orientation errors to a large degree (more than two alternative methods).

The second research question for this dissertation asked whether it would be possible to spatially detect ("map") the spatial regions where the geomagnetic field might be distorted to properly decrease the level of involvement of the magnetic correction in the definition of the final orientation estimate. Chapter 4 in this dissertation details the process that has been proposed to map the magnetic trustworthiness parameter, μ, in the regions of space visited by the MARG module. It also explains how the knowledge of that mapping is used to adjust the two-tier SLERP interpolation that defines the final orientation estimate of the GMV-D algorithm.

The last research question proposed dissertation asked if a system could be developed that would bring together information from all the sensor modalities in the MARG module to result in a robust estimate of its orientation, even in areas where the geomagnetic field might be distorted. This dissertation has proposed the GMV-D algorithm, explained in Chapter 4, and it has benchmarked its performance against its precursor approach, GMV-S, and a commonly used solution, the Kalman Filter. The results shown in Chapter 6 indicate that, indeed, the GMV-D method was more successful than the other two methods in providing robust orientation estimates, even in the region of space in which a significant magnetic field distortion was present.

The improved real-time orientation estimation achieved by GMV-D may facilitate the development of alternative input methods for computer-human interaction, towards the development of more flexible input devices, and also for the tracking of hand movements in 3D virtual environments, which are becoming more and more popular. The development of hand motion tracking benefits the users as it provides a more natural way to interact with a computer.

Two distinct advantages of the GMV-D approach are, first that it does not require the user to set any initialization parameters (as other approaches, such as the Kalman Filter require), and second, that it implements the processing pipelines where the information derived from the three sensing modalities available in the MARG module (gyroscope, accelerometer, and magnetometer) are kept independent and separately accessible throughout must of each algorithm iteration. This is in contrast to other approaches which might "fuse" or "mix" the several sources of information early on in the algorithm. This parallel management of the information from the sensors allows a more explicit comparison between them or even a retrospective analysis for

each of them, such that additional mechanisms for suppressing the influence of a sensing modality that is displaying incongruent behavior.

In summary, it is likely that the contributions of the GMV-D method may help in making the MARG orientation estimation process more robust by fully taking advantage of the MARG operating conditions for a typical human-computer interaction application and comprehensively utilizing all the sensing modalities available in the MARG module.

9.2 Future Work

The parallel processing pipelines that keep the information from the accelerometer and magnetometer independent throughout each iteration of the GMV-D algorithm may provide an alternative mechanism to detect when the local magnetic field is likely distorted, based exclusively on the internal signals from the MARG module. In the current version of GMV-D, the local magnetic trustworthiness parameter, μ, is defined by "mapping" the regions of space that have been previously visited by the MARG module. The "mapping" process makes use of the position estimates provided by the IR-camera system. This is completely acceptable for the intended use of the MARG module considered in this dissertation (human-computer interaction). However, finding an alternative mechanism for the detection of magnetic field alterations, utilizing only the signals generated by the MARG module, would extend the scope of use of the algorithm. This would be very significant, for example, if the GMV-D orientation estimation method could also be used in ambulatory applications (such as gait analysis) where position estimates may not be readily available.

Similarly, the accuracy level reached by the GMV-D method may be increased if a higher-level- management of the trustworthiness parameters, α and μ, is implemented dynamically. For example, the current system updates the μ value for any visited voxel by merely replacing the value with the newest calculation of μ. This was implemented so that, even if the ferromagnetic objects in the working space of the system were to move slowly, the system would keep an updated μ map that can reflect those slow variations. To enhance the accuracy of the system, however, it may be beneficial to keep track of the last few (e.g., 3 or 5) values of μ calculated for a given voxel, assigning the mean of those few values in the update of the voxel.

The overall accuracy level of the GMV-D method might be increased if a progressive, nonlinear "alpha" degradation process is in place to restrict the accelerometer corrections to only those cases with a high level of acceleration trustworthiness, α, in the later intervals of operation of the system. Initially, all the voxels are initialized with $\mu = 0$, and, therefore, no significant corrections are made on the basis of the magnetometer measurements. This means that, in the initial intervals of operation of the system, the only significant corrections will be made on the basis of the accelerometer measurements, in proportion to α. Therefore, it is important that the "gaps" between those meaningful corrections be small (to prevent the uncontrolled growth of the gyroscopic drift error. In contrast, during the later phases of operation of the system, the commonly visited voxels around the user will be mapped, and for many of them, the μ value assigned will be high. Therefore, significant corrections will be performed more frequently based on both accelerometer and magnetometer readings. In this later stages of operation, a mechanism could be put in place to "degrade" to vary low levels (close to 0) any values of a that are not above a dynamically changing

threshold ($\alpha_{DEGRADE}$), so that, for these late iterations in the operation of the system significant accelerometer corrections will only be applied for cases where it is highly likely that the module is really very close to static, enhancing the accuracy of those corrections. Initially ($\alpha_{DEGRADE}$) can be set at a low value so that, essentially, α is never "degraded," and GMV-D will perform as described in this dissertation. When the system has been operating for a while, and more frequent correct magnetic corrections are taking place, a larger value of $\alpha_{DEGRADE}$ will make it possible only to apply significant accelerometer corrections when the system is highly confident that the assumption of a static module is closely fulfilled. This is a luxury that may not be afforded at the beginning of the operation of the system since significant magnetic corrections will likely be infrequent right after the initialization of the system.

BIBLIOGRAPHY

[1] Prabhakar, O. P., & Sahu, N. K. (2013). A survey on: Voice command recognition technique. *International Journal of Advanced Research in Computer Science and Software Engineering, 3*(5), 576-585.

[2] Evans, A., Romeo, M., Bahrehmand, A., Agenjo, J., & Blat, J. (2014). 3D graphics on the web: A survey. *Computers & Graphics, 41*, 43-61.

[3] Simsek, I., & Tuncer, C. (2016). (2016). The design and use of educational games in 3D virtual worlds. Paper presented at the *Society for Information Technology & Teacher Education International Conference,* 611-617.

[4] Shiratuddin, M. F., & Thabet, W. (2011). Utilizing a 3D game engine to develop a virtual design review system.

[5] Kim, S. J. J. (2012). (2012). A user study trends in augmented reality and virtual reality research: A qualitative study with the past three years of the ISMAR and IEEE VR conference papers. Paper presented at the *2012 International Symposium on Ubiquitous Virtual Reality,* 1-5.

[6] Nonnarit, O., Barreto, A., Ratchatanantakit, N., Tangnimitchok, S., & Ortega, F. R. (2018). (2018). Real-time implementation of orientation correction algorithm for 3D hand motion tracking interface. Paper presented at the *International Conference on Universal Access in Human-Computer Interaction,* 228-242.

[7] Suarez, J., & Murphy, R. R. (2012). (2012). Hand gesture recognition with depth images: A review. Paper presented at the *2012 IEEE RO-MAN: The 21st IEEE International Symposium on Robot and Human Interactive Communication,* 411-417.

[8] Murthy, G., & Jadon, R. S. (2009). A review of vision based hand gestures recognition. *International Journal of Information Technology and Knowledge Management, 2*(2), 405-410.

[9] Roy, K., Idiwal, D. P., Agrawal, A., & Hazra, B. (2015). (2015). Flex sensor based wearable gloves for robotic gripper control. Paper presented at the *Proceedings of the 2015 Conference on Advances in Robotics,* 1-5.

[10] Maurya, S. K., & Prasad, R. K. (2015). Gesture controlled robotic hand using flex sensor. *International Journal for Scientific Research & Development, 3*(07), 646-648.

[11] Weber, P., Rueckert, E., Calandra, R., Peters, J., & Beckerle, P. (2016). (2016). A low-cost sensor glove with vibrotactile feedback and multiple finger joint and hand motion sensing for human-robot interaction. Paper presented at the *2016 25th IEEE International Symposium on Robot and Human Interactive Communication (RO-MAN),* 99-104.

[12] 12. Johnson, R. C.3-axis MEMs gyro chip debuts. Retrieved from http://www.eetimes.com/document.asp?doc_id=1313118

[13] Foxlin, E. (2002). Motion tracking requirements and technologies. *Handbook of Virtual Environment Technology, 8*, 163-210.

[14] Zhang, P., Hancock, C. M., Lau, L., Roberts, G. W., & de Ligt, H. (2019). Low-cost IMU and odometer tightly coupled integration with robust kalman filter for underground 3-D pipeline mapping. *Measurement, 137*, 454-463.

[15] Qiu, D., Li, S., Wang, T., Ye, Q., Li, R., Ding, K., & Xu, H. (2020). A high-precision calibration approach for camera-IMU pose parameters with adaptive constraints of multiple error equations. *Measurement, 153*, 107402.

[16] Yang, Y. (2020). An improved nonlinear FastEuler AHRS estimation based on the SVDCKF algorithm. *arXiv Preprint arXiv:2002.08317,*

[17] Khankalantary, S., Rafatnia, S., & Mohammadkhani, H. (2020). An adaptive constrained type-2 fuzzy hammerstein neural network data fusion scheme for low-cost SINS/GNSS navigation system. *Applied Soft Computing, 86*, 105917.

[18] Brossard, M., Bonnabel, S., & Barrau, A. (2020). Denoising imu gyroscopes with deep learning for open-loop attitude estimation. *IEEE Robotics and Automation Letters, 5*(3), 4796-4803.

[19] Yuan, Q., Asadi, E., Lu, Q., Yang, G., & Chen, I. (2019). Uncertainty-based IMU orientation tracking algorithm for dynamic motions. *IEEE/ASME Transactions on Mechatronics, 24*(2), 872-882.

[20] Hao, M., Chen, K., & Fu, C. (2019). Smoother-based 3-D foot trajectory estimation using inertial sensors. *IEEE Transactions on Biomedical Engineering, 66*(12), 3534-3542.

[21] Tjhai, C., & O'Keefe, K. (2019). Using step size and lower limb segment orientation from multiple low-cost wearable inertial/magnetic sensors for pedestrian navigation. *Sensors, 19*(14), 3140.

[22] Irie, K. (2020). (2020). A loop-closure-based inertial motion capture, with application to sports swing measurements. Paper presented at the *2020 IEEE/SICE International Symposium on System Integration (SII)*, 693-699.

[23] Shaikh, S., & Malhotra, A. (2020). Real-time feedback control for knee prosthesis using motion fusion algorithm in 6-DOF IMU.

[24] Duraffourg, C., Bonnet, X., Dauriac, B., & Pillet, H. (2019). Real time estimation of the pose of a lower limb prosthesis from a single shank mounted IMU. *Sensors, 19*(13), 2865.

[25] Duan, H., Huang, M., Yang, Y., Hao, J., & Chen, L. (2020). Ambient light based hand gesture recognition enabled by recurrent neural network. *IEEE Access, 8*, 7303-7312.

[26] Tran, D., Ho, N., Yang, H., Baek, E., Kim, S., & Lee, G. (2020). Real-time hand gesture spotting and recognition using RGB-D camera and 3D convolutional neural network. *Applied Sciences, 10*(2), 722.

[27] Park, G., Argyros, A., Lee, J., & Woo, W. (2020). 3d hand tracking in the presence of excessive motion blur. *IEEE Transactions on Visualization and Computer Graphics, 26*(5), 1891-1901.

[28] Jiang, S., Li, L., Xu, H., Xu, J., Gu, G., & Shull, P. B. (2019). Stretchable e-skin patch for gesture recognition on the back of the hand. *IEEE Transactions on Industrial Electronics, 67*(1), 647-657.

[29] Nazarahari, M., & Rouhani, H. (2021). 40 years of sensor fusion for orientation tracking via magnetic and inertial measurement units: Methods, lessons learned, and future challenges. *Information Fusion, 68*, 67-84. doi:10.1016/j.inffus.2020.10.018

[30] Nazarahari, M., & Rouhani, H. (2021). Sensor fusion algorithms for orientation tracking via magnetic and inertial measurement units: An experimental comparison survey. *Information Fusion, 76*, 8-23. doi:10.1016/j.inffus.2021.04.009

[31] Sabatini, A. M. (2006). Quaternion-based extended kalman filter for determining orientation by inertial and magnetic sensing. *IEEE Transactions on Biomedical Engineering, 53*(7), 1346-1356. doi:10.1109/TBME.2006.875664

[32] Minh-Duc Hua, Ducard, G., Hamel, T., Mahony, R., & Rudin, K. (2014). Implementation of a nonlinear attitude estimator for aerial robotic vehicles. *IEEE Transactions on Control Systems Technology, 22*(1), 201-213. doi:10.1109/TCST.2013.2251635

[33] Justa, J., Šmídl, V., & Hamáček, A. (2020). Fast AHRS filter for accelerometer, magnetometer, and gyroscope combination with separated sensor corrections. *Sensors (Basel, Switzerland), 20*(14), 3824. doi:10.3390/s20143824

[34] Harindranath, A., & Arora, M. (Dec 2018). (Dec 2018). MEMS IMU sensor orientation algorithms-comparison in a simulation environment. Paper presented at the 1-6. doi:10.1109/ICNEWS.2018.8904029 Retrieved from https://ieeexplore.ieee.org/document/8904029

[35] Madgwick, S. O. H. (2010). *An efficient orientation filter for inertial and inertial/magnetic sensor arrays*

[36] Mahony, R., Hamel, T., & Pflimlin, J. -. (2005). (2005). Complementary filter design on the special orthogonal group SO(3). Paper presented at the 1477-1484.

doi:10.1109/CDC.2005.1582367 Retrieved from https://ieeexplore.ieee.org/document/1582367

[37] Kalman, R. E. (1960). A new approach to linear filtering and prediction problems.

[38] Barreto, A., Adjouadi, M., Ortega, F. R., & Nonnarit, O. (2020). *Intuitive understanding of kalman filtering with MATLAB®* CRC Press.

[39] Marins, J. L., Xiaoping Yun, Bachmann, E. R., McGhee, R. B., & Zyda, M. J.An extended kalman filter for quaternion-based orientation estimation using MARG sensors. Paper presented at the *Proceedings 2001 IEEE/RSJ International Conference on Intelligent Robots and Systems. Expanding the Societal Role of Robotics in the the Next Millennium (Cat. no. 01CH37180), , 4* 2003-2011 vol.4. doi:10.1109/IROS.2001.976367 Retrieved from https://ieeexplore.ieee.org/document/976367

[40] Peppoloni, L., Filippeschi, A., Ruffaldi, E., & Avizzano, C. A. (Sep 2013). (Sep 2013). A novel 7 degrees of freedom model for upper limb kinematic reconstruction based on wearable sensors. Paper presented at the 105-110. doi:10.1109/SISY.2013.6662551 Retrieved from https://ieeexplore.ieee.org/document/6662551

[41] Yost Labs, I. (2017). *3-space sensor miniature attitude & heading reference system with pedestrian tracking user's manual*. Portsmouth, Ohio:

[42] Paul Yost, & Yost Labs.QGRAD vs. kalman filter. Retrieved from https://yostlabs.com/about/feature-advantages/qgrad-vs-kalman-filter/

[43] Roetenberg, D., Luinge, H. J., Baten, C. T. M., & Veltink, P. H. (2005). Compensation of magnetic disturbances improves inertial and magnetic sensing of human body segment orientation. *IEEE Transactions on Neural Systems and Rehabilitation Engineering*, *13*(3), 395-405. doi:10.1109/TNSRE.2005.847353

[44] Daponte, P., De Vito, L., Rapuano, S., Riccio, M., & Picariello, F. (May 2015). (May 2015). Compensating magnetic disturbances on MARG units by means of a low complexity data fusion algorithm. Paper presented at the 157-162. doi:10.1109/MeMeA.2015.7145191 Retrieved from https://ieeexplore.ieee.org/document/7145191

[45] Daponte, P., De Vito, L., Mazzilli, G., Picariello, F., & Rapuano, S. (May 2017). (May 2017). Method for compensating the effect of disturbances on magnetometer measurements: Experimental results. Paper presented at the 1-6. doi:10.1109/I2MTC.2017.7969980 Retrieved from https://ieeexplore.ieee.org/document/7969980

[46] Wu, J. (2019). Real-time magnetometer disturbance estimation via online nonlinear programming. *IEEE Sensors Journal*, *19*(12), 4405-4411. doi:10.1109/JSEN.2019.2901925

[47] Valenti, R. G., Dryanovski, I., & Xiao, J. (2015). Keeping a good attitude: A quaternion-based orientation filter for imus and margs. *Sensors (Basel, Switzerland)*, *15*(8), 19302-19330. doi:10.3390/s150819302

[48] Shoemake, K. (1985). (1985). Animating rotation with quaternion curves. Paper presented at the *Proceedings of the 12th Annual Conference on Computer Graphics and Interactive Techniques*, 245-254.

[49] Dam, E. B., Koch, M., & Lillholm, M. (1998). *Quaternions, interpolation and animation* Citeseer.

[50] Nonnarit, O., Barreto, A., Tangnimitchok, S., & Ratchatanantakit, N. (2018). (2018). Orientation correction for a 3d hand motion tracking interface using inertial measurement units. Paper presented at the 321-333.

[51] de Franceschi, M., & Zardi, D. (2003). Evaluation of cut-off frequency and correction of filter-induced phase lag and attenuation in eddy covariance analysis of turbulence data. *Boundary-Layer Meteorology*, *108*(2), 289-303. doi:10.1023/A:1024157310388

[52] Meyer, J., Padayachee, K., & Broughton, B. A. (2019). *A robust complementary filter approach for attitude estimation of unmanned aerial vehicles using AHRS*

[53] Helmert, F. R. (1884). *Die mathematischen und physikalischen theorieen der höheren geodäsie* BG Teubner.

[54] Jekeli, C. (2012). *Inertial navigation systems with geodetic applications* de Gruyter.

[55] Mathworks.Earth-centered-earth-fixed frame, from mathworks.com. Retrieved from https://www.mathworks.com/help/map/choose-a-3-d-coordinate-system.html

[56] Jazar, R. N.*Theory of applied robotics [electronic resource]: Kinematics, dynamics, and control* Springer.

[57] Hamilton, W. R. (1848). Xi. on quaternions; or on a new system of imaginaries in algebra. *The London, Edinburgh, and Dublin Philosophical Magazine and Journal of Science*, *33*(219), 58-60.

[58] O-larnnithipong, N.*Hand motion tracking system using inertial measurement units and infrared cameras* Retrieved from https://digitalcommons.fiu.edu/etd/3905

[59] Allen, J. J. (2007). *Introduction to MEMS (MicroElectroMechanical systems).* ().Sandia National Lab.(SNL-NM), Albuquerque, NM (United States).

[60] Barlian, A. A., Park, W., Mallon, J. R., Rastegar, A. J., & Pruitt, B. L. (2009). Semiconductor piezoresistance for microsystems. *Proceedings of the IEEE, 97*(3), 513-552.

[61] *IEEE standard specification format guide and test procedure for coriolis vibratory gyros* (2004). doi:10.1109/IEEESTD.2004.95744

[62] Gyroscope-microstructure. Retrieved from https://howtomechatronics.com/wp-content/uploads/2015/11/Gyroscope-Microstructure.jpg

[63] Murphy, C. (2017). Choosing the most suitable MEMs accelerometer for your Application—Part 1. *Analog Dialogue, 51*(4), 1-10.

[64] Gauss, K. F. (1837). (1837). Intensitas vis magneticae terrestris ad mensuram absolutam revocata. Paper presented at the (3) 166-174.

[65] Passaro, V., Cuccovillo, A., Vaiani, L., De Carlo, M., & Campanella, C. E. (2017). Gyroscope technology and applications: A review in the industrial perspective. *Sensors, 17*(10), 2284.

[66] Yost Labs. (2014). Gyroscope drift rating. Retrieved from https://yeitechnology.freshdesk.com/support/solutions/articles/1000131493-gyroscope-drift-rating

[67] Ratchatanantakit, N., Nonnarit, O., Barreto, A., & Tangnimitchok, S. (2019). (2019). Consistency study of 3D magnetic vectors in an office environment for IMU-based hand tracking input development. Paper presented at the 377-387.

[68] Montgomery, D. C., Peck, E. A., & Vining, G. G. (2021). *Introduction to linear regression analysis* John Wiley & Sons.

[69] Tech specs. Retrieved from https://optitrack.com/cameras/v120-trio/specs.html

[70] Volume size diagrams. Retrieved from https://d111srqycjesc9.cloudfront.net/V120-Trio%20Volume%20Size%20Diagrams.pdf

[71] 3-space sensor micro USB specification. (2007). Retrieved from https://yostlabs.com/product/3-space-micro-usb/

[72] Montgomery, D. C. (2017). *Design and analysis of experiments* John wiley & sons.

[73] Field, A. (2009). *Discovering statistics using SPSS* Sage publications.

[74] Tewari, D., Chhabra, M., & Baul, S. (2019). Microelectromechanical system (MEMS) sensor market by type (inertial sensor, pressure sensor, optical sensor, environment sensor, and ultrasonic sensor) and application (consumer electronics, automotive, industrial, aerospace & defense, healthcare, telecommunication, and others). *Global Opportunity Analysis and Industry Forecast,* (Allied Mark Res), Pg.335.

APPENDICES

Appendix A

Source Codes of The Implementation of Orientation Correction Algorithm using Gravity Vector and Magnetic North Vector with Double SLERP

```
using UnityEngine;
using System;
using System.Collections;
using System.IO.Ports;
using UnityEditor;
using System.Text;
using System.Collections.Generic;
public class StreamRaw1MovementGuide : MonoBehaviour
{
    private IEnumerator coroutine;
    // Connect to the serial port the 3-Space Sensor is connected to
    public static SerialPort sp0 = new SerialPort("\\\\.\\COM3", 115200,
Parity.None, 8, StopBits.One);

    // Print-to-file variables
    public string filenameNo = "";
    private static string FileStr0;
    private static string FileStr1;
    private static string FileStrMark;
    private int rotCount = 0;
    private int markCount = 0;
    private bool handRotated = true;
    private float k = 0.0f;
    private GUIStyle guiStyle = new GUIStyle();
    List<Quaternion> Qref = new List<Quaternion>();
    List<Vector3> uPref = new List<Vector3>();
    List<Vector3> Pref = new List<Vector3>();

    // Command packet for getting the filtered tared orientation as a
quaternion
    // {header byte, command byte, [data bytes], checksum byte}
    // checksum = (command byte + data bytes) % 256

    public static byte TSS_START_BYTE = 0xF7;
    public static byte TSS_SET_STREAMING_SLOTS = 0x50;
    public static byte TSS_SET_STREAMING_TIMING = 0x52;
    public static byte TSS_START_STREAMING = 0x55;
    public static byte TSS_STOP_STREAMING = 0x56;
    public static byte TSS_GET_SENSOR_MOTION = 0x2D;
    public static byte TSS_GET_RAD_PER_SEC_GYROSCOPE = 0x26;
    public static byte TSS_GET_CORRETED_LINEAR_ACC_AND_GRAVITY = 0x27;
    public static byte TSS_GET_CORRETED_COMPASS = 0x28;
    public static byte TSS_GET_TARED_ORIENTAITON_AS_QUAT = 0x00;
    public static byte TSS_NULL = 0xFF;
    public static byte TSS_TARE_CURRENT_ORIENTATION = 0x60;
    public static byte CHECK_SUM = (byte)((TSS_SET_STREAMING_SLOTS +
TSS_GET_SENSOR_MOTION + TSS_GET_RAD_PER_SEC_GYROSCOPE +
TSS_GET_CORRETED_LINEAR_ACC_AND_GRAVITY +
        TSS_GET_CORRETED_COMPASS + TSS_GET_TARED_ORIENTAITON_AS_QUAT + TSS_NULL
+ TSS_NULL + TSS_NULL) % 256);

    public static byte[] stream_slots_bytes = {TSS_START_BYTE,
                                        TSS_SET_STREAMING_SLOTS,
                                        TSS_GET_SENSOR_MOTION, // Slot0 - 4
TSS_GET_RAD_PER_SEC_GYROSCOPE, // Slot1 - 12
TSS_GET_CORRETED_LINEAR_ACC_AND_GRAVITY, // Slot2 - 12
TSS_GET_CORRETED_COMPASS, // Slot3 - 12
TSS_GET_TARED_ORIENTAITON_AS_QUAT, // Slot4 - 16
TSS_NULL, // Slot5
```

```
TSS_NULL, // Slot6
TSS_NULL, // Slot7
CHECK_SUM};

    public static byte[] stream_timing_bytes = new byte[15];
    public static byte[] start_stream_bytes = new byte[3];
    public static byte[] tare_bytes = { TSS_START_BYTE,
TSS_TARE_CURRENT_ORIENTATION, TSS_TARE_CURRENT_ORIENTATION }; // <-- one
command, checksum = command itself
    public static byte[] interval = BitConverter.GetBytes(70000);
    public static byte[] delay = BitConverter.GetBytes(0);
    public static byte[] duration = BitConverter.GetBytes(0xFFFFFFFF);
    public static bool EndOfSimulation = false;
    public static Quaternion HandOrientation;
    public static Vector3 HandPosition;
    // ---------- Algorithm Variables ---------- //
    private double CurrentTime = 0.00;
    private double PreviousTime = 0.00;
    private float SamplingTime;
    private int N = 0;
    private static int BuffSize = 3;
    private float B_SCALING = 1.0f;
    private float alpWeight = 0.25f;
    private float muWeight = 0.25f;

    private float Stillness0;
    private Vector3 Gyro0, Accelero0, Magneto0;
    private Quaternion IMUQuat0;
    private Vector3[] GyroBuff0 = new Vector3[BuffSize];
    private Vector3[] AcceleroBuff0 = new Vector3[BuffSize];
    private Vector3[] MagnetoBuff0 = new Vector3[BuffSize];
    private float[] StillnessBuff0 = new float[BuffSize];
    private Vector3 GyroAvg0 = new Vector3();
    private Vector3 AcceleroAvg0 = new Vector3();
    private Vector3 MagnetoAvg0 = new Vector3();
    private float StillnessAvg0 = new float();
    private float alpha0 = new float();
    private float prevAlphaX0 = 1.0f;
    private float prevAlphaY0 = 1.0f;
    private float thisAlphaX0 = new float();
    private float thisAlphaY0 = new float();
    private Vector3 Bias0 = new Vector3(0, 0, 0);
    private Vector3 fixedBias0 = new Vector3(-0.008081f, -0.002751f, -
0.008184f); // <------------------------- Fixed single bias values ------------
-------------------
    private Vector3 BiasBuff0 = new Vector3(0, 0, 0);
    private int trigcount0 = 0;
    private Vector3 UnbiasedGyro0 = new Vector3(0, 0, 0);
    private Vector3 UnbiasedGyroWithfixedBias0 = new Vector3(0, 0, 0);
    private Quaternion w0; // Pure Quaternion
    private Quaternion wfixed0; // Pure Quaternion
    private Quaternion dqG0;
    private Quaternion dqGfixed0;
    private Quaternion qG0 = new Quaternion(0, 0, 0, 1);
    private Quaternion qGfixed0 = new Quaternion(0, 0, 0, 1);
    private Quaternion dqGA0;
    private Quaternion qGA0 = new Quaternion(0, 0, 0, 1);
    private Quaternion dqGM0;
    private Quaternion qGM0 = new Quaternion(0, 0, 0, 1);
    private Quaternion A_int0 = new Quaternion();
    private Quaternion M_int0 = new Quaternion();
```

```
    private Quaternion a40 = new Quaternion(0, 0, 0, 1);
    private Vector3 a30 = new Vector3();
    private Quaternion m40 = new Quaternion(0, 0, 0, 1);
    private Vector3 m30 = new Vector3();
    public static Quaternion qOUT0 = new Quaternion(0, 0, 0, 1);
    public static Quaternion qOUT1 = new Quaternion(0, 0, 0, 1);

    private Vector3 EulerFixed0;
    private Vector3 EulerKalman0;
    private Vector3 EulerGMV1;
    private Vector3 EulerGMV0;

    private Quaternion qGfixed0e;
    private Quaternion IMUQuat0e;
    public static Quaternion qOUT0e;
    public static Quaternion qOUT1e;

    private Vector3 EulerFixed0e;
    private Vector3 EulerKalman0e;
    private Vector3 EulerGMV0e;
    private Vector3 EulerGMV1e;

    private Vector3 PosE;

    private static int VoxNO = 200;
    private static float[,,] MU = new float[VoxNO, VoxNO, VoxNO];

    float TA = 0.80f; //Alpha Threshold
    float TM = 0.80f; //MU Threshold

    Quaternion qGpost, mGA4;
    Vector3 mGA3;
    float cosGamma, norm_MagAvg, norm_mGA3, temp_mu, gg, gl;
    static float thisMu = 0.0f, prevMu = 0.0f, thisTempMu = 0.0f, prevTempMu =
0.0f, mu0 = 0.0f;
    int Stage;
    int ma = 1;
    int mt = 2;

    static int LocateVoxX = 0;
    static int LocateVoxY = 0;
    static int LocateVoxZ = 0;

    float prevMuX = 0.0f;
    float prevMuY = 0.0f;

    string[] step = { "Start at initial position", "Move to position 1", "Move
to position 2", "Move to initial position" };
void Start()
    {
        /*
            private static string FileParameter;
            private static string FielEUL;
         */
        FileStr0 = "Assets/Raw1Recordings/rec" + filenameNo + "GMV0.txt";
        FileStr1 = "Assets/Raw1Recordings/rec" + filenameNo + "GMV1.txt";
        FileStrMark = "Assets/Raw1Marks/mark" + filenameNo + ".txt";

        // Start box at dock.
        Qref.Add(Quaternion.Euler(0, 0, 0));
        // Move hand to Pos1
```

```
        // Non mag distortion
        Qref.Add(Quaternion.Euler(0, 0, 0));
        Qref.Add(Quaternion.Euler(0, 0, 90));
        Qref.Add(Quaternion.Euler(0, 0, 0));
        Qref.Add(Quaternion.Euler(90, 0, 0));
        Qref.Add(Quaternion.Euler(0, 0, 0));
        Qref.Add(Quaternion.Euler(0, 90, 0)); // Check y
        Qref.Add(Quaternion.Euler(0, 0, 0));
        Qref.Add(Quaternion.Euler(90, 0, 45)); //
        Qref.Add(Quaternion.Euler(0, 0, 0));
        // Move hand to Pos2
        // mag distortion
        Qref.Add(Quaternion.Euler(0, 0, 0));
        Qref.Add(Quaternion.Euler(0, 0, 90));
        Qref.Add(Quaternion.Euler(0, 0, 0));
        Qref.Add(Quaternion.Euler(90, 0, 0));
        Qref.Add(Quaternion.Euler(0, 0, 0));
        Qref.Add(Quaternion.Euler(0, 90, 0)); // Check y
        Qref.Add(Quaternion.Euler(0, 0, 0));
        Qref.Add(Quaternion.Euler(90, 0, 45)); //
        Qref.Add(Quaternion.Euler(0, 0, 0));
        // Move hand to Dock
        Qref.Add(Quaternion.Euler(0, 0, 0));

        // Set the read/write timeoutsS
        sp0.WriteTimeout = 500;
        sp0.ReadTimeout = 500;

        if (!sp0.IsOpen)
        {
            try
            {
                sp0.Open();

                print("Serial Port 0 is open (COM4)");
            }
            catch (TimeoutException)
            {
            }

        }
        else
        {
            Debug.LogError("All Serial Ports are already open.");
        }

        sp0.Write(stream_slots_bytes, 0, stream_slots_bytes.Length);

        Array.Reverse(interval);
        Array.Reverse(delay);
        Array.Reverse(duration);

        stream_timing_bytes[0] = TSS_START_BYTE;
        stream_timing_bytes[1] = TSS_SET_STREAMING_TIMING;
        interval.CopyTo(stream_timing_bytes, 2);
        delay.CopyTo(stream_timing_bytes, 6);
        duration.CopyTo(stream_timing_bytes, 10);
        stream_timing_bytes[14] = (byte)((stream_timing_bytes[1] +
stream_timing_bytes[2] + stream_timing_bytes[3] + stream_timing_bytes[4] +
stream_timing_bytes[5] + stream_timing_bytes[6] +
```

```
        stream_timing_bytes[7] + stream_timing_bytes[8] +
stream_timing_bytes[9] + stream_timing_bytes[10] + stream_timing_bytes[11] +
stream_timing_bytes[12] + stream_timing_bytes[13]) % 256);

        sp0.Write(stream_timing_bytes, 0, stream_timing_bytes.Length);

        tareSensor();

        start_stream_bytes[0] = TSS_START_BYTE;
        start_stream_bytes[1] = TSS_START_STREAMING;
        start_stream_bytes[2] = TSS_START_STREAMING;

        sp0.Write(start_stream_bytes, 0, start_stream_bytes.Length);

        //coroutine = TestCoroutine ();
        //StartCoroutine (coroutine);

    }
void Update()
    {
        if (!EndOfSimulation)
        {
            // A quaternion consists of 4 floats which is 16 bytes
            byte[] read_bytes0 = new byte[56];   // <----------------- No. of
Bytes
// Mono, for some reason, seems to randomly fail on the first read after a
write so we must loop
// through to make sure the bytes are read and Mono also seems not to always
read the amount asked
// so we must also read one byte at a time
            int read_counter = 100;
            int byte_idx0 = 0;

            PreviousTime = CurrentTime;
            CurrentTime += 1 * Time.deltaTime;
            SamplingTime = (float)(CurrentTime - PreviousTime);

            while (read_counter > 0)
            {

                try
                {
                    byte_idx0 += sp0.Read(read_bytes0, byte_idx0, 1);
                }
                catch
                {
                    // Failed to read from serial port
                }
                if (byte_idx0 == 56)
                { // <----------------- No. of Bytes
                    break;
                }
                if (read_counter <= 0)
                {
                    throw new System.Exception("Failed to read quaternion from
port too many times." +
                        " This could mean the port is not open or the Mono
serial read is not responding.");
                }
                --read_counter;
            }
```

```
            // Convert bytes to floats
            Stillness0 = bytesToFloat(read_bytes0, 0);
            Gyro0.x = bytesToFloat(read_bytes0, 4);
            Gyro0.y = bytesToFloat(read_bytes0, 8);
            Gyro0.z = bytesToFloat(read_bytes0, 12);
            Accelero0.x = bytesToFloat(read_bytes0, 16);
            Accelero0.y = bytesToFloat(read_bytes0, 20);
            Accelero0.z = bytesToFloat(read_bytes0, 24);
            Magneto0.x = bytesToFloat(read_bytes0, 28);
            Magneto0.y = bytesToFloat(read_bytes0, 32);
            Magneto0.z = bytesToFloat(read_bytes0, 36);
            IMUQuat0.x = bytesToFloat(read_bytes0, 40);
            IMUQuat0.y = bytesToFloat(read_bytes0, 44);
            IMUQuat0.z = bytesToFloat(read_bytes0, 48);
            IMUQuat0.w = bytesToFloat(read_bytes0, 52);

            // Orientation Correction Algorithm using gravity vector and
magnetic North vector correction.
            // --- Code starts here ---!
            GMVD();

            if (Input.GetKey("escape"))
            {
                sp0.Close();
                print("All ports are closed!");
                EndOfSimulation = true;
            }
        }
if (rotCount != 0)
        {
            HandOrientation = Quaternion.Slerp(Qref[rotCount - 1],
Qref[rotCount], k);
            // HandPosition = Vector3.Lerp(uPref[rotCount - 1],
uPref[rotCount], k);
            if (k < 1)
            {
                k += 0.05f; // Set speed rotation animation
            }
        }
        else
        {
            HandOrientation = Qref[rotCount];
            // HandPosition = uPref[rotCount];
        }

        //print ("x=" + HandOrientation.x + " y=" + HandOrientation.y + " z=" +
HandOrientation.z + " w=" + HandOrientation.w);
        this.transform.rotation = HandOrientation;
        // this.transform.position = HandPosition;
    }

    // Helper function for taking the bytes read from the 3-Space Sensor and
converting them into a float
    float bytesToFloat(byte[] raw_bytes, int offset)
    {
        byte[] big_bytes = new byte[4];
        big_bytes[0] = raw_bytes[offset + 3];
        big_bytes[1] = raw_bytes[offset + 2];
        big_bytes[2] = raw_bytes[offset + 1];
        big_bytes[3] = raw_bytes[offset + 0];
        return BitConverter.ToSingle(big_bytes, 0);
```

```
    }

    void tareSensor()
    {
        sp0.Write(tare_bytes, 0, 3);
    }

    Quaternion myQuatConj(Quaternion q)
    {

        Quaternion q_result = new Quaternion(-1.0f * q.x, -1.0f * q.y, -1.0f *
q.z, q.w);
        return q_result;
    }

    Quaternion myQuatIntegrate(Quaternion dq, Quaternion q, float dt)
    {

        Quaternion omega = dq * myQuatConj(q);
        omega = new Quaternion(2.0f * omega.x, 2.0f * omega.y, 2.0f * omega.z,
2.0f * omega.w);
        omega = new Quaternion((omega.x * dt) / 2.0f, (omega.y * dt) / 2.0f,
(omega.z * dt) / 2.0f, (omega.w * dt) / 2.0f);
        float omega_norm2 = Mathf.Sqrt(Mathf.Pow(omega.x, 2) +
Mathf.Pow(omega.y, 2) + Mathf.Pow(omega.z, 2));
        Quaternion exp = new Quaternion();

        if (omega_norm2 != 0)
        {

            exp.x = Mathf.Exp(omega.w) * (Mathf.Sin(omega_norm2) / omega_norm2)
* omega.x;
            exp.y = Mathf.Exp(omega.w) * (Mathf.Sin(omega_norm2) / omega_norm2)
* omega.y;
            exp.z = Mathf.Exp(omega.w) * (Mathf.Sin(omega_norm2) / omega_norm2)
* omega.z;
            exp.w = Mathf.Exp(omega.w) * Mathf.Cos(omega_norm2);
        }
        else
        {

            exp.x = Mathf.Exp(omega.w) * omega.x;
            exp.y = Mathf.Exp(omega.w) * omega.y;
            exp.z = Mathf.Exp(omega.w) * omega.z;
            exp.w = Mathf.Exp(omega.w) * Mathf.Cos(omega_norm2);
        }

        Quaternion q_result = exp * q;

        return q_result;
    }

    Quaternion myQuatNormalize(Quaternion q)
    {

        float q_norm = Mathf.Sqrt((Mathf.Pow(q.x, 2) + Mathf.Pow(q.y, 2) +
Mathf.Pow(q.z, 2) + Mathf.Pow(q.w, 2)));
        Quaternion q_result = new Quaternion(q.x / q_norm, q.y / q_norm, q.z /
q_norm, q.w / q_norm);

        return q_result;
```

```
    }

void OnGUI()
    {

        GUIStyle buttonGUIStyle = new GUIStyle("button");
        buttonGUIStyle.normal.textColor = Color.green;
        buttonGUIStyle.hover.textColor = Color.green;
        buttonGUIStyle.fontStyle = FontStyle.Bold;

        GUILayout.BeginArea(new Rect(10, Screen.height - 40, 200, 200));
        GUILayout.BeginVertical("box");
        if (GUILayout.Button("Close ALL Ports"))
        {
            sp0.Close();
            print("COM4 is closed!");
            EndOfSimulation = true;
            UnityEditor.EditorApplication.isPlaying = false;
        }
        GUILayout.EndVertical();
        GUILayout.EndArea();

        GUILayout.BeginArea(new Rect(Screen.width / 2 - 100, 40, 300, 200));
        if (!EndOfSimulation)
        {
            // GUILayout.Label("Now Recording... Subject" + filenameNo + "\n" +
markCount.ToString() + "/" + Qref.Count.ToString() + " orientation(s) marked");
        }
        else
        {
            // GUILayout.Label("Recording Completed for Subject" + filenameNo);
        }
        GUILayout.EndArea();
        if (markCount < Qref.Count)
        {
            if (handRotated)
            {
                GUILayout.BeginArea(new Rect(Screen.width - 210, Screen.height
- 40, 200, 200));
                GUILayout.BeginVertical("box");
                if (GUILayout.Button("Mark this position & orientation"))
                {
                    PosE.x = OptitrackStreamingClient.markerX;
                    PosE.y = OptitrackStreamingClient.markerY;
                    PosE.z = OptitrackStreamingClient.markerZ;

                    qGfixed0e = myQuatNormalize(myQuatConj(Qref[rotCount]) *
qGfixed0);
                    IMUQuat0e = myQuatNormalize(myQuatConj(Qref[rotCount]) *
IMUQuat0);
                    qOUT0e = myQuatNormalize(myQuatConj(Qref[rotCount]) *
qOUT0);
                    qOUT1e = myQuatNormalize(myQuatConj(Qref[rotCount]) *
qOUT1);

                    EulerFixed0e = qGfixed0e.eulerAngles;
                    EulerKalman0e = IMUQuat0e.eulerAngles;
                    EulerGMV0e = qOUT0e.eulerAngles;
                    EulerGMV1e = qOUT1e.eulerAngles;
```

```
                    if (EulerFixed0e.x > 180.0)
                        EulerFixed0e.x = -(360.0f - EulerFixed0e.x);
                    if (EulerFixed0e.y > 180.0)
                        EulerFixed0e.y = -(360.0f - EulerFixed0e.y);
                    if (EulerFixed0e.z > 180.0)
                        EulerFixed0e.z = -(360.0f - EulerFixed0e.z);

                    if (EulerKalman0e.x > 180.0)
                        EulerKalman0e.x = -(360.0f - EulerKalman0e.x);
                    if (EulerKalman0e.y > 180.0)
                        EulerKalman0e.y = -(360.0f - EulerKalman0e.y);
                    if (EulerKalman0e.z > 180.0)
                        EulerKalman0e.z = -(360.0f - EulerKalman0e.z);

                    if (EulerGMV0e.x > 180.0)
                        EulerGMV0e.x = -(360.0f - EulerGMV0e.x);
                    if (EulerGMV0e.y > 180.0)
                        EulerGMV0e.y = -(360.0f - EulerGMV0e.y);
                    if (EulerGMV0e.z > 180.0)
                        EulerGMV0e.z = -(360.0f - EulerGMV0e.z);

                    if (EulerGMV1e.x > 180.0)
                        EulerGMV1e.x = -(360.0f - EulerGMV1e.x);
                    if (EulerGMV1e.y > 180.0)
                        EulerGMV1e.y = -(360.0f - EulerGMV1e.y);
                    if (EulerGMV1e.z > 180.0)
                        EulerGMV1e.z = -(360.0f - EulerGMV1e.z);

                    System.IO.File.AppendAllText(FileStrMark,
System.String.Format("T{0},", CurrentTime)); //write data to file

                    markCount++;
                    print("Orientation marked (" + markCount.ToString() + "/" +
Qref.Count.ToString() + ")");
                    handRotated = false;
                }
                GUILayout.EndVertical();
                GUILayout.EndArea();
            }
            else
            {

                GUILayout.BeginArea(new Rect(Screen.width - 210, Screen.height
- 40, 200, 200));
                GUILayout.BeginVertical("box");
                if (GUILayout.Button("Show Hand Sequence", buttonGUIStyle))
                {

                    print("Hand Model is rotating");
                    rotCount++;
                    k = 0.0f;
                    handRotated = true;
                }
                GUILayout.EndVertical();
                GUILayout.EndArea();
            }
            guiStyle = GUI.skin.GetStyle("Label");
            guiStyle.fontSize = 30; //change the font size
            guiStyle.alignment = TextAnchor.UpperCenter;

            float movePosSp = 0.05f; // Positon moving speed.
```

```
            if (rotCount == 0)
            {
                GUI.Label(new Rect(Screen.width / 2 - 200, 40, 400, 100),
step[0], guiStyle);
            }
            else if (rotCount == 1)
            {
                Vector3 newPosition = transform.position; // We store the
current position

                if((int)transform.position.z != -3){
                    newPosition.z = newPosition.z - movePosSp;
                    transform.position = newPosition; // We pass it back
                }

                GUI.Label(new Rect(Screen.width / 2 - 200, 40, 400, 100),
step[1], guiStyle);
            }
            else if (rotCount == 10)
            {
                Vector3 newPosition = transform.position; // We store the
current position
                if((int)transform.position.x != -3){
                    newPosition.x = newPosition.x - movePosSp;
                    transform.position = newPosition; // We pass it back
                }
                GUI.Label(new Rect(Screen.width / 2 - 200, 40, 400, 100),
step[2], guiStyle);
            }
            else if (rotCount == 19)
            {
                Vector3 newPosition = transform.position; // We store the
current position
                if((int)transform.position.x != 3 &&
(int)transform.position.z != 2){
                    newPosition.x = newPosition.x + movePosSp;
                    newPosition.z = newPosition.z + movePosSp;
                    transform.position = newPosition; // We pass it back
                }
                GUI.Label(new Rect(Screen.width / 2 - 200, 40, 400, 100),
step[3], guiStyle);
            }
            else
            {
                GUI.Label(new Rect(Screen.width / 2 - 200, 40, 400, 100),
"Performing", guiStyle);
            }

            if (rotCount == 2 || rotCount == 11)
            {
                GetComponent<Renderer>().material.color = Color.green;
            }
            else if (rotCount == 4 || rotCount == 13)
            {
                GetComponent<Renderer>().material.color = Color.blue;
            }
            else if (rotCount == 6 || rotCount == 15)
            {
                GetComponent<Renderer>().material.color = Color.yellow;
            }
            else if (rotCount == 8 || rotCount == 17)
```

```
            {
                GetComponent<Renderer>().material.color = Color.red;
            }
            else
            {
                GetComponent<Renderer>().material.color = Color.grey;
            }
        }
    }
    void GMVD()
    {
        for (int i = BuffSize - 1; i >= 1; i--)
        {
            GyroBuff0[i] = GyroBuff0[i - 1];
            AcceleroBuff0[i] = AcceleroBuff0[i - 1];
            MagnetoBuff0[i] = MagnetoBuff0[i - 1];
            StillnessBuff0[i] = StillnessBuff0[i - 1];
        }

        GyroBuff0[0] = Gyro0;
        AcceleroBuff0[0] = Accelero0;
        MagnetoBuff0[0] = Magneto0;
        StillnessBuff0[0] = Stillness0;

        N += 1;

        int ClampBuffSize = Mathf.Clamp(N, 0, BuffSize);

        GyroAvg0 = new Vector3(0, 0, 0);
        AcceleroAvg0 = new Vector3(0, 0, 0);
        MagnetoAvg0 = new Vector3(0, 0, 0);
        StillnessAvg0 = new float();

        for (int i = 0; i < ClampBuffSize; i++)
        {

            GyroAvg0 += GyroBuff0[i];
            AcceleroAvg0 += AcceleroBuff0[i];
            MagnetoAvg0 += MagnetoBuff0[i];
            StillnessAvg0 += StillnessBuff0[i];
        }

        GyroAvg0 /= ClampBuffSize;
        AcceleroAvg0 /= ClampBuffSize;
        MagnetoAvg0 /= ClampBuffSize;
        thisAlphaX0 = Mathf.Pow((StillnessAvg0 / ClampBuffSize), 2.0f);
        thisAlphaY0 = alpWeight * (prevAlphaX0) + (1.0f - alpWeight) *
(prevAlphaY0);
        prevAlphaX0 = thisAlphaX0;
        prevAlphaY0 = thisAlphaY0;

        // Calculate new Bias offset Errors when the sensor is NOT rotating

        if (Mathf.Abs(Gyro0.x) < 0.03 && Mathf.Abs(Gyro0.y) < 0.03 &&
Mathf.Abs(Gyro0.z) < 0.03)
        {
            BiasBuff0.x += Gyro0.x;
            BiasBuff0.y += Gyro0.y;
            BiasBuff0.z += Gyro0.z;
            trigcount0 += 1;
```

```
        }
        else
        {
            trigcount0 = 0;
            BiasBuff0.x = 0;
            BiasBuff0.y = 0;
            BiasBuff0.z = 0;
        }

        if (trigcount0 == 5)
        {

            Bias0 = new Vector3(BiasBuff0.x / 5.0f, BiasBuff0.y / 5.0f,
BiasBuff0.z / 5.0f);
            trigcount0 = 0;
            BiasBuff0.x = 0;
            BiasBuff0.y = 0;
            BiasBuff0.z = 0;
        }
        // Remove Gyroscope Bias
        UnbiasedGyro0 = Gyro0 - (B_SCALING * Bias0);
        // Compute Quaternions

        if (N == 1)
        {
            A_int0 = new Quaternion(Accelero0.x, Accelero0.y, Accelero0.z,
0.0f);
            M_int0 = new Quaternion(Magneto0.x, Magneto0.y, Magneto0.z, 0.0f);
        }

        w0 = new Quaternion(UnbiasedGyro0.x, UnbiasedGyro0.y, UnbiasedGyro0.z,
0.0f);
        qG0 = qOUT1;
        qGA0 = qOUT1;
        qGM0 = qOUT1;

        dqG0 = (qG0 * w0);
        dqG0 = new Quaternion(0.5f * dqG0.x, 0.5f * dqG0.y, 0.5f * dqG0.z, 0.5f
* dqG0.w);
        qG0 = myQuatIntegrate(dqG0, qG0, SamplingTime);
        qG0 = myQuatNormalize(qG0);

        dqGA0 = (qGA0 * w0);
        dqGA0 = new Quaternion(0.5f * dqGA0.x, 0.5f * dqGA0.y, 0.5f * dqGA0.z,
0.5f * dqGA0.w);
        qGA0 = myQuatIntegrate(dqGA0, qGA0, SamplingTime);
        qGA0 = myQuatNormalize(qGA0);

        dqGM0 = (qGM0 * w0);
        dqGM0 = new Quaternion(0.5f * dqGM0.x, 0.5f * dqGM0.y, 0.5f * dqGM0.z,
0.5f * dqGM0.w);
        qGM0 = myQuatIntegrate(dqGM0, qGM0, SamplingTime);
        qGM0 = myQuatNormalize(qGM0);

        // Compute Gravity and Magnetic North Vectors

        a40 = myQuatConj(qGA0) * (A_int0 * qGA0);
        a30 = new Vector3(a40.x, a40.y, a40.z);
        m40 = myQuatConj(qGM0) * (M_int0 * qGM0);
        m30 = new Vector3(m40.x, m40.y, m40.z);
```

```
        // Compute Differences between measured and calculated Gravity Vector
described in Quaternion domain

        Vector3 qAv0 = Vector3.Cross(AcceleroAvg0, a30);
        float qAw0 = Vector3.Magnitude(AcceleroAvg0) * Vector3.Magnitude(a30) +
Vector3.Dot(AcceleroAvg0, a30);
        Quaternion deltaQa0 = myQuatNormalize(new Quaternion(qAv0.x, qAv0.y,
qAv0.z, qAw0));
        qGA0 = myQuatNormalize(qGA0 * deltaQa0);


        // Compute Differences between measured and calculated Magnetic North
Vector described in Quaternion domain

        Vector3 qMv0 = Vector3.Cross(Magneto0, m30);
        float qMw0 = Vector3.Magnitude(Magneto0) * Vector3.Magnitude(m30) +
Vector3.Dot(Magneto0, m30);
        Quaternion deltaQm0 = myQuatNormalize(new Quaternion(qMv0.x, qMv0.y,
qMv0.z, qMw0));
        qGM0 = myQuatNormalize(qGM0 * deltaQm0);

        // Quaternion Interpolation

        alpha0 = thisAlphaY0;

        ////////////////////////////////////////////
        ///GENERATE (alpha)
        ////////////////////////////////////////////

        alpha0 = (ma * alpha0) + (1 - ma); //Linear Equation
        alpha0 = (alpha0 + (Math.Abs(alpha0))) / 2;
        if (alpha0 < 0.01f)
        {
            alpha0 = 0.5f;
        }
        else
        {
            alpha0 = alpha0;
        }
        ////////////////////////////////////////////
        ///GENERATE (MU)
        ////////////////////////////////////////////

        qGpost = qGA0;
        mGA4 = myQuatConj(qGpost) * (M_int0 * qGpost);
        mGA3 = new Vector3(mGA4.x, mGA4.y, mGA4.z);
        norm_MagAvg = (float)Math.Sqrt((Magneto0.x * Magneto0.x) + (Magneto0.y
* Magneto0.y) + (Magneto0.z * Magneto0.z));
        norm_mGA3 = (float)Math.Sqrt((mGA3.x * mGA3.x) + (mGA3.y * mGA3.y) +
(mGA3.z * mGA3.z));
        cosGamma = Vector3.Dot(MagnetoAvg0, mGA3);
        cosGamma = cosGamma / (norm_MagAvg * norm_mGA3);
        if (cosGamma > 1.0f)
            cosGamma = 1.0f;
        if (cosGamma < -1.0f)
            cosGamma = -1.0f;
        ////cosGamma = MagnetoAvg0.dot(mGA3);
        gg = (float)Math.Acos((double)cosGamma);

        //gg = Gamma;
        gl = -mt * gg + 1.0f; //Linear Equation
```

```
        temp_mu = (1.0f + gl) / 2.0f;
        //temp_mu = gg;
        if (temp_mu < 0)
        {
            thisMu = 0;
        }
        else
        {
            thisMu = temp_mu;
        }

        float thisMuY = 0.0f;
        float thisMuX = thisMu * thisMu;

        thisMuY = (muWeight* prevMuX) + (1.0f-muWeight) * prevMuY;
        prevMuX = thisMuX;
        prevMuY = thisMuY;
        LocateVOX(OptitrackStreamingClient.markerX,
OptitrackStreamingClient.markerY, OptitrackStreamingClient.markerZ);

        if (MU[LocateVoxX, LocateVoxY, LocateVoxZ] < TM && alpha0 > TA)
        {
            MU[LocateVoxX, LocateVoxY, LocateVoxZ] = thisMuY;
        }
        qOUT1 = Quaternion.Slerp((Quaternion.Slerp(qG0, qGM0, MU[LocateVoxX,
LocateVoxY, LocateVoxZ])), (Quaternion.Slerp(qG0, qGA0, alpha0)), alpha0);

        // Print the data to a file
        System.IO.File.AppendAllText(FileStr1,
System.String.Format("T{0},{1},{2},{3},{4},{5},{6},{7},{8},{9},{10},{11},{12},{
13},{14},{15},{16},{17},{18},{19} \n"
            , CurrentTime, StillnessAvg0, Gyro0.x, Gyro0.y, Gyro0.z,
Accelero0.x, Accelero0.y, Accelero0.z, Magneto0.x, Magneto0.y, Magneto0.z,
alpha0, qOUT1.x, qOUT1.y, qOUT1.z, qOUT1.w, LocateVoxX, LocateVoxY, LocateVoxZ,
MU[LocateVoxX, LocateVoxY, LocateVoxZ]));
        long milliseconds = DateTimeOffset.Now.ToUnixTimeMilliseconds();
    }

//Voxel Calculation
    private static void LocateVOX(float x, float y, float z)
    {
        float OffsetNewOriginX = (float)-50.0; //Set New origin at x: -200
        float OffsetNewOriginY = (float)-50.0; //Set New origin at y: -200

        float MPx = (x);
        float MPy = (y);
        float MPz = (z);

        float nMPx = MPx - OffsetNewOriginX;
        float nMPy = MPy - OffsetNewOriginY;
        float nMPz = MPz;

        int VoxelSize = 1;

        LocateVoxX = (int)(nMPx / VoxelSize) + 1;
        LocateVoxY = (int)(nMPy / VoxelSize) + 1;
        LocateVoxZ = (int)(nMPz / VoxelSize) + 1;
    }
}
```

Appendix B

The Health Sciences Institutional Review Board (IRB) of Florida International University Protocol Approval

FLORIDA INTERNATIONAL UNIVERSITY

Office of Research Integrity
Research Compliance, MARC 414

Dr. Armando Barreto

Neeranut Ratchatanantakit

April 3, 2019

"Digital Signal Processing for Human-Computer Interactions from Inertial Measurement Units"

The Institutional Review Board of Florida International University has your study for the use of human subjects via the process. Your study was found to be in compliance with this institution's Federal Wide Assurance (00000060).

IRB-19-0110		03/29/19
107758	**IRB Expiration Date:**	03/29/22

As a requirement of IRB Approval you are required to:

Submit an IRB Amendment Form for all proposed

Receive annual review and re-approval of your study prior to your IRB expiration date. Submit the IRB Renewal Form at least 30 days in advance of the study's expiration date.
or discontinued.

HIPAA Privacy Rule:

Special Conditions: **N/A**

For further information, you may visit the IRB website at http://research.fiu.edu/irb

Appendix C

Adult Consent to Participate in a Research Study

FIU IRB Approval:	03/29/2019
FIU IRB Expiration:	03/29/2022
FIU IRB Number:	IRB-19-0110

FIU | FLORIDA INTERNATIONAL UNIVERSITY

- _____
- _____
- _____
- ____
- _____
- _____
- _____

FIU IRB Approval:	03/29/2019
FIU IRB Expiration:	03/29/2022
FIU IRB Number:	IRB-19-0110

3. You will be asked to repeat performing a sequence of simple hand movement tasks again for different signal processing algorithm.
4. You will take off the glove after finishing the experiment.
5. You will be asked to fill out the questionnaire regarding the experience of using hand motion tracking system.

RISKS AND/OR DISCOMFORTS
The minimal-risk is no different than working with a computer at work or home and the data and the experiment uses non-invasive sensors for data collecting process.

BENEFITS
There is no direct benefit to the subject, other than contributing the knowledge of human-computer interaction to the development of more natural user interface.

ALTERNATIVES
There are no known alternatives available to you other than not taking part in this study. However, any significant new findings developed during the course of the research which may relate to your willingness to continue participation will be provided to you.

CONFIDENTIALITY
The records of this study will be kept private and will be protected to the fullest extent provided by law. In any sort of report, we might publish, we will not include any information that will make it possible to identify you. Research records will be stored securely, and only the researcher team will have access to the records. However, your records may be inspected by authorized University or other agents who will also keep the information confidential.

COMPENSATION & COSTS
You will not be provided any compensation for your participation.
There are no costs to you for participating in this study.

RIGHT TO DECLINE OR WITHDRAW
Your participation in this study is voluntary. You are free to participate in the study or withdraw your consent at any time during the study. You will not lose any benefits if you decide not to participate or if you quit the study early. The investigator reserves the right to remove you without your consent at such time that he/she feels it is in the best interest.

RESEARCHER CONTACT INFORMATION
If you have any questions about the purpose, procedures, or any other issues relating to this research study you may contact Neeranut Ratchatanantakit at EC 3970, Tel. (305) 348-6072, Email Address: nratc001@fiu.edu

IRB CONTACT INFORMATION

FIU IRB Approval:	03/29/2019
FIU IRB Expiration:	03/29/2022
FIU IRB Number:	IRB-19-0110

If you would like to talk with someone about your rights of being a subject in this research study or about ethical issues with this research study, you may contact the FIU Office of Research Integrity by phone at 305-348-2494 or by email at ori@fiu.edu.

PARTICIPANT AGREEMENT

I have read the information in this consent form and agree to participate in this study. I have had a chance to ask any questions I have about this study, and they have been answered for me. I understand that I will be given a copy of this form for my records.

_____ _ _____

Signature of Participant Date

_____

Printed Name of Participant

_____ _ _____

Signature of Person Obtaining Consent Date

VITA

NEERANUT RATCHATANANTAKIT

1989	Born, Bangkok, Thailand
2009-2013	B.Eng., Mechatronics Engineering Assumption University Samut Prakan, Thailand
2013	Automation & Robotics Lab Assistance HEIG-VD (HES-SO) Yverdon-les-Bains, Switzerland
2013 - 2015	Mechanical Design & Project Engineer Seagate Technology (Thailand) Co.Ltd. Samut Prakan, Thailand
2015 - 2016	PLC Trainer Bosch Rexroth Bangkok, Thailand
2016 - 2021	Ph.D., Electrical and Computer Engineering Florida International University Miami, Florida
	Graduate Teaching Assistant Florida International University Miami, Florida

PUBLICATIONS AND PRESENTATIONS

Ratchatanantakit, N., Nonnarit, O., Barreto, A., & Tangnimitchok, S. (2019, July). Consistency Study of 3D Magnetic Vectors in an Office Environment for IMU-based Hand Tracking Input Development. In International Conference on Human-Computer Interaction (pp. 377-387). Springer, Cham.

Nonnarit, O., *Ratchatanantakit, N.*, Tangnimitchok, S., Ortega, F., & Barreto, A. (2019, March). Hand tracking interface for virtual reality interaction based on MARG sensors. In 2019 IEEE Conference on Virtual Reality and 3D User Interfaces (VR) (pp. 1717-1722). IEEE.

Nonnarit, O., *Ratchatanantakit, N.*, Barreto, A., & Tangnimitchok, S. (2019, July). Evaluation of Orientation Correction Algorithms in Real-Time Hand Motion Tracking for Computer Interaction. In International Conference on Human-Computer Interaction (pp. 348-365). Springer, Cham.

Nonnarit, O., *Ratchatanantakit, N.*, Tangnimitchok, S., Ortega, F. R., Barreto, A., & Adjouadi, M. (2019, July). Statistical Analysis of Novel and Traditional Orientation Estimates from an IMU-Instrumented Glove. In International Conference on Human-Computer Interaction (pp. 282-299). Springer, Cham.

Tangnimitchok, S., Nonnarit, O., *Ratchatanantakit, N.*, & Barreto, A. (2019, July). Eliminating the Pupillary Light Response from Pupil Diameter Measurements Using an RGB Camera. In International Conference on Human-Computer Interaction (pp. 397-406). Springer, Cham.

Tangnimitchok, S., Nonnarit, O., *Ratchatanantakit, N.*, & Barreto, A. (2019, July). Affective Monitor: A Process of Data Collection and Data Preprocessing for Building a Model to Classify the Affective State of a Computer User. In International Conference on Human-Computer Interaction (pp. 179-190). Springer, Cham.

Nonnarit, O., Barreto, A., Tangnimitchok, S., & *Ratchatanantakit, N.* (2018, July). Orientation Correction for a 3D Hand Motion Tracking Interface Using Inertial Measurement Units. In International Conference on Human-Computer Interaction (pp. 321-333). Springer, Cham.

Nonnarit, O., Barreto, A., *Ratchatanantakit, N.*, Tangnimitchok, S., & Ortega, F. R. (2018, July). Real-time implementation of orientation correction algorithm for 3D hand motion tracking interface. In International Conference on Universal Access in Human-Computer Interaction (pp. 228-242). Springer, Cham.

Tangnimitchok, S., Nonnarit, O., *Ratchatanantakit, N.*, Barreto, A., Ortega, F. R., & Rishe, N. D. (2018, July). A System for Non-intrusive Affective Assessment in the Circumplex Model from Pupil Diameter and Facial Expression Monitoring. In International Conference on Human-Computer Interaction (pp. 465-477). Springer, Cham.